

AD-E 201 181

(2)

PL-TR-92-2172

AD-A256 686



**SPECTRAL ANALYSIS OF THE SHUTTLE GLOW:
AIS EXPERIMENT SCIENCE SUPPORT**

A. L. Broadfoot

University of Arizona
Lunar and Planetary Laboratory
Tucson, Arizona 85721

23 June 1992

**DTIC
ELECTE
AUG 20 1992
S A D**

Final Report
August 1988-November 1991

APPROVED FOR PUBLIC RELEASE; DISTRIBUTION UNLIMITED



**PHILLIPS LABORATORY
AIR FORCE SYSTEMS COMMAND
HANSCOM AIR FORCE BASE, MASSACHUSETTS 01731-5000**

92-23091



92 8 19 018

This technical report has been reviewed and is approved for publication.



DAVID J. KNECHT
Contract Manager



CHARLES P. PIKE, Chief
Spacecraft Interactions Branch

This document has been reviewed by the ESD Public Affairs Office (PA) and is releasable to the National Technical Information Service.

Qualified requesters may obtain additional copies from the Defense Technical Information Center. All others should apply to the National Technical Information Service.

If your address has changed, or if you wish to be removed from the mailing list, or if the addressee is no longer employed by your organization, please notify PL/TSI, Hanscom AFB, MA 01731-5000. This will assist us in maintaining a current mailing list.

Do not return copies of this report unless contractual obligations or notices on a specific document require that it be returned.

REPORT DOCUMENTATION PAGE			Form Approved OMB No. 0704-0188	
Public reporting burden for this collection of information is estimated to average 1 hour per response, including the time for reviewing instructions, searching existing data sources, gathering and maintaining the data needed, and completing and reviewing the collection of information. Send comments regarding this burden estimate or any other aspect of this collection of information, including suggestions for reducing this burden, to Washington Headquarters Services, Directorate for Information Operations and Reports, 1215 Jefferson Davis Highway, Suite 1204, Arlington, VA 22202-4302, and to the Office of Management and Budget, Paperwork Reduction Project (0704-0188), Washington, DC 20503.				
1. AGENCY USE ONLY (Leave blank)	2. REPORT DATE 23 June 92	3. REPORT TYPE AND DATES COVERED Final Report (Aug 1988 - Nov 1991)		
4. TITLE AND SUBTITLE Spectral Analysis of the Shuttle Glow. A.S Science Support		5. FUNDING NUMBERS PE 63220C PR S321 TA 47 WU AA Contract F19628-88-K-0028		
6. AUTHOR(S) A. L. Broadfoot				
7. PERFORMING ORGANIZATION NAME(S) AND ADDRESS(ES) University of Arizona Lunar and Planetary Laboratory Tucson, Arizona 85721		8. PERFORMING ORGANIZATION REPORT NUMBER		
9. SPONSORING/MONITORING AGENCY NAME(S) AND ADDRESS(ES) Phillips Laboratory Hanscom AFB, MA 01731-5000 Contract Manager: David Knecht/WSSI		10. SPONSORING/MONITORING AGENCY REPORT NUMBER PL-TR-92-2172		
11. SUPPLEMENTARY NOTES				
12a. DISTRIBUTION/AVAILABILITY STATEMENT Approved for public release; Distribution unlimited		12b. DISTRIBUTION CODE		
13. ABSTRACT (Maximum 200 words) The science support effort for the Arizona Imager/Spectrograph (AIS) included several aspects of shuttle and spacecraft interactions research. Software development, flight planning and analysis of related ground-based observations of the shuttle interaction were included. The AIS flight planning task continued from delivery of the experiment to the SPAS II at Messerschmitt-Bolkow-Blohm in Germany in May 1989 until flight of the experiment on STS-39 in April/May of 1991. Since the AIS was to provide supporting data for all of the experiments on the IBSS/SPAS II mission, special experiment sequences were developed for each of the six experiments. With various options, this amounted to about thirty templates or individual experiments. The AIS data were reviewed carefully to identify periods in which good data were received on the identified experiments. About 45 data sets were identified and work was begun on preparing them for analysis. A second scientific data set, which was a companion to the AIS, came from the AMOS observational program. The commonality between the data from the observations of thruster firings by the shuttle over AMOS and the AIS flight experiments joined these two scientific analysis programs.				
14. SUBJECT TERMS SPECTROMETER, ULTRAVIOLET, VISIBLE, INFRARED, SPACE FLIGHT, DATA ANALYSIS			15. NUMBER OF PAGES 76	
			16. PRICE CODE	
17. SECURITY CLASSIFICATION OF REPORT Unclassified	18. SECURITY CLASSIFICATION OF THIS PAGE Unclassified	19. SECURITY CLASSIFICATION OF ABSTRACT Unclassified	20. LIMITATION OF ABSTRACT SAR	

CONTENTS

Introduction	1
Appendix A: Spectrographic Observations at Wavelengths Near 630 nm of the Interaction Between the Atmosphere and the Space Shuttle Exhaust	3
Appendix B: A Study of the NH Interaction	33
Appendix C: Application of the Intensified CCD to Airglow and Auroral Measurements	45

DTIC QUALITY INSPECTED 8

Accession For	
NTIS CRA&I	<input checked="" type="checkbox"/>
DTIC TAB	<input type="checkbox"/>
Unannounced	<input type="checkbox"/>
Justification	
By	
Distribution/	
Availability Codes	
Dist	Avail And/or Special
A-1	

The Arizona Imager/Spectrograph (AIS) science support effort included several aspects of shuttle and spacecraft interactions research. Software development, flight planning and analysis of related ground-based observations of the shuttle interaction were included.

The first objective of the program was to establish a data handling and analysis system which would be ready to receive the AIS data, evaluate the data and provide imaging and spectrographic tools for analysis. Two *Sun Microsystems* computers were procured for this task. The "Image Reduction and Analysis Facility" (IRAF) software system, developed by the Kitt Peak National Observatory, was adopted and installed on the Sun computers by our data center personnel.

Several students and some of the scientific staff became involved in the experiment planning, data handling and analysis for both the AIS flight program and the ground-based shuttle observational program at the Air Force Maui Optical Station (AMOS).

The AIS flight planning task continued from delivery of the experiment to the payload integrator in Germany in May 1989 until flight of the experiment on the Space Shuttle in April/May of 1991. Since the AIS was also to provide supporting data for all other experiments on the mission, special experiment sequences were developed for each of the six experiments. With various options, this amounted to about thirty templates or individual experiments.

As the program proceeded and our shuttle operational procedure was defined, a problem in communications was identified. A committee solution to this problem was to reduce the necessity to edit templates by putting more options in the instrument to select from. A further one hundred templates were designed. These templates had to be run individually through the payload system in Germany. Flight scheduling and planning became an associated problem in supporting the AIS in flight. The planning team then became the flight team for the AIS. In the fall of 1990 and spring of 1991, the team was in training through various Joint Integrated Simulation meetings for Shuttle/payload flight activity at Johnson Space Center. Finally these personnel supported the AIS experiment on the Shuttle at JSC during the flight.

Preliminary data were available immediately after flight from the real-time downlink. These data provided "quick look" material for our sponsors. The flight data which had been recorded on board the satellite became available in late May 1991. Unfortunately the shuttle supplementary data was not forthcoming. At the end of this contract in September, 1991, we had not received sufficient shuttle altitude and pointing information from the Data Management Center to proceed with definitive analysis.

The AIS data were reviewed carefully to identify periods in which good data were received on the identified experiments. About 45 data sets were identified and work was begun on preparing them for analysis.

A second scientific data set, which was a companion to the AIS, came from the AMOS observational program. The commonality between the data from the observations of thruster firings by the shuttle over AMOS and the AIS flight experiments joined these two scientific analysis programs. The results of the AMOS observations were directly applicable to the AIS experiment planning activity. The AMOS experiments produced data in the same format as the AIS. This activity improved our software preparation activity for the AIS and was a good training opportunity. The analysis team received data from six AMOS overflights.

On the first opportunity, the spectrum of the shuttle PRCS (Primary Reaction Control System) was acquired. Although the resolution was low, several important spectral features were identified: a very strong emission of NH was discovered near 3400 Å, and a longer wavelength emission which was subsequently identified as the OI (6300, 6364 Å) lines. The work on the OI line has been submitted for publication (Appendix A). A study of the NH interaction was initiated. Dr. Joseph W. Chamberlain provided the attached report (Appendix B) with respect to the hydrogen interaction with the atmosphere. Some of the work and analysis in the preparation of two technical papers (Appendices C and D) was provided by this contract.

APPENDIX A

Final Report, SFRC F19628-88-K-0028

Paper prepared for publication:

**"Spectrographic Observation at Wavelengths near 630 nm of the
Interaction between the Atmosphere and the Space Shuttle Exhaust"**

SPECTROGRAPHIC OBSERVATION AT WAVELENGTHS NEAR 630 NM OF THE INTERACTION BETWEEN THE ATMOSPHERE AND THE SPACE SHUTTLE EXHAUST

A. L. Broadfoot,¹ E. Anderson,¹ P. Sherard,¹ D. J. Knecht,²

R. A. Viereck,² C. P. Pike,² Edmond Murad,² J. E. Elgin,³ L. S. Bernstein,³

I. L. Kofsky,⁴ D. L. A. Rall,⁴ J. Blaha,⁵ and F. L. Culbertson⁵

ABSTRACT

The collision between the exhaust from the Primary Reaction Control System (PRCS) engines (870 lbs thrust) of the space shuttle and the ambient atmosphere has been observed from the Air Force Maui Optical Station (AMOS). Spectra have been obtained in the wavelength region near 630 nm. The temporal, spatial, and spectral distribution of the emission in this region has been recorded. The results reported here indicate that when the exhaust of the space shuttle interacts with the atmosphere in the ram direction, an intense, long-lasting emission at 630 nm due to $O(^1D \rightarrow ^3P)$ is generated. A substantial amount of $O(^1D)$ is swept back onto the orbiter. Two processes are proposed for the formation of $O(^1D)$: (1) excitation of atmospheric $O(^3P)$ by collisions with the exhaust of the space shuttle engines; and (2) charge exchange between ambient O^+ and exhaust H_2O . Calculations using the SOCRATES Code show excellent agreement with the data.

1. Lunar and Planetary Laboratory, University of Arizona, Tucson, AZ
2. Phillips Laboratory, OLAA-WSSI, Hanscom AFB, MA
3. Spectral Sciences, Inc., Burlington, MA
4. PhotoMetrics, Inc., Woburn, MA
5. NASA, Johnson Space Center, Houston, TX

INTRODUCTION

In a previous report (Murad et al., 1990), we presented telescope images of the interaction of space shuttle exhaust gases with the atmosphere as a function of angle of attack. Those measurements were made in the visible region of the spectrum using an ISIT camera with an uncharacterized generic S-20 response. Such observations are relevant to the use of space-borne platforms for astronomical measurements (see, for example, Koch et al., 1988), routine operations (see, for example, Scialdone, 1984), and plume research. Onboard mass spectrometry has shown complex mass spectra that are strongly influenced by the firings of attitude-control jets on the Space Shuttle (Ehlers, 1986; Wulf and von Zahn, 1986). These onboard measurements, of course, detect only those molecules that have been scattered back into the shuttle bay; the reaction of the exhaust with the atmosphere and the products of this interaction are not directly observed. Because the nature of the optical environment of the space shuttle has important implications for use of space-borne platforms for research, we have extended the data by obtaining spectral, spatial, and temporal information about the interaction region. In this paper we present and interpret spectral data for an emission feature near 630 nm, a region that is amenable to interpretation. As we will show, the emission is due to a metastable species, $O(^1D)$.

EXPERIMENT

Primary Reaction Control System (PRCS) engines of the Space Shuttle, STS-41, were fired on October 7, 1990 at 1326 UT during a period when the Shuttle could be observed from the Air Force Maui Optical Station (AMOS). The altitude of the shuttle was 290 km. The firings were observed with an ICCD spectrograph at the focus of a 200-mm aperture, f/5

telescope mounted on and coaligned with a 1.6-meter telescope. ICCD-spectrograph design criteria have been discussed in general by Broadfoot et al. (1992). The instrument used here had a high throughput ($f/1.2$), broad spectral coverage (310-710 nm), and time resolution consistent with the time scale of the interaction phenomena (0.84 sec per exposure). The slit image at the detector was 192 pixels in length and was subdivided electronically into twelve segments of 16 pixels each. In the direction of slit width the image was dispersed over 384 pixels, coadded to provide a spectral resolution of about 10 nm. The instrument was calibrated before and after the experiment.

In order to observe the morphological development of the interaction between the shuttle exhaust gases and the atmosphere, the spectrograph slit length was aligned with the shuttle velocity vector, as shown in Figure 1. Engines were fired successively in four directions (ram, wake, down, and up), each burn lasting three seconds followed by a quiescent period of five seconds. The thrust directions were forward (ram, hereafter referred to as Burn 1), aft (wake, hereafter referred to as Burn 2), down (nadir, hereafter referred to as Burn 3), and up (zenith, hereafter referred to as Burn 4). The geometry of the experiment and the burn times as viewed from AMOS are illustrated in Figure 2. The trajectory passed near the zenith at AMOS (nearly overhead), but the burns were conducted after reaching that point to avoid looking into the near-zenith moon. Because the instrument line of sight lay in the plane containing all four exhaust directions, the slit sampled all four burns.

RESULTS

The spectrograph data contain spectral information (location of pixel in the dispersion

direction), spatial information (location of pixel in the direction of slit length), and temporal information (sampling by successive exposures), provided the emissions are sufficiently bright to yield adequate counting statistics. If not, the data can be processed by summing pixel values in several different ways that yield the highest spectral, spatial, or temporal resolution of the emission region. For highest spectral resolution, counting statistics can be improved by summing over time (more than one exposure) and/or spatial extent (adding one or more slit segments). Similarly, for best temporal information, data can be summed over a selected spectral range as well as over slit length, and best spatial information is obtained by summing over time and spectral dispersion.

Figure 3 presents the data for burn No. 1 (ram) in the 500-710 nm region of the spectrum, comparing the exhaust interaction spectrum with the airglow spectrum measured with the same instrument. The burn spectrum was acquired in three seconds, while the airglow spectrum required an exposure of 180 s. These observations were made on October 7, 1990, three days after full moon (91% full). The strong feature between 615 and 645 nm is identified as the $O(^1D \rightarrow ^3P)$ transition (630.0, 636.4 nm). This identification was subsequently confirmed by the spectrum labeled STS-43 in Figure 3, from a similar experiment on 7 August 1991, in which a higher-resolution spectrograph was used. The second feature in the 665-695 nm region is due mostly to second-order diffraction of the NH ($A \rightarrow X$) fundamental at 336 nm. Some small part of the feature at 665-695 nm may be due to the OH ($X^2\Pi_r$) Meinel system, as proposed in an earlier study (Murad *et al.*, 1990). However, that contribution appears to be quite small. Therefore, in the following discussion, we will refer to the wavelength of this feature as 336 nm. We plan to discuss in this report the nature and origin of the emissions in the spectral region near

630 nm; to a much lesser extent we will also discuss the difference between the two features of the interaction spectrum around 630 and 336 nm.

Figure 4 shows the intensity of these two emissions as a function of time. These curves were obtained by summing over all slit segments and over the wavelength range 615-645 or 665-695-nm (see Figures 3 and 5). The start and stop times of the burn were taken from the shuttle time log. The time scale has been referenced to zero at the start of the first burn, and the time at which each data point is plotted refers to the beginning of the spectrograph exposure. A notable feature of Figure 4 is the delay in rise and fall of the 630-nm emission with respect to the 336-nm emission. The 336-nm emission turns on and off with the thruster. The delay of the 630-nm emission is between two and three seconds. This suggests a forbidden emission but ascribing it to the $O(^1D \rightarrow ^3P)$ transition which has a radiative lifetime of about 150 seconds (Radzig and Smirnov, 1985), seemed unlikely until the dynamics of the experiment was modeled as discussed below. The marked difference in intensity between the ram and wake firings is expected from the energetics of the gas-gas reaction. The nadir and zenith intensities, shown in Figure 4 are relatively strong; the difference between them may be due to unequal sampling of the plumes by the spectrograph because of telescope aiming. The remainder of this report will deal mainly with the data from the first (ram) burn.

A stacked time-series of spectra (eleven consecutive 0.84-s exposures with all the slit segments added) for burn No. 1 is shown in Figure 5. The spectra have been smoothed with a low pass mathematical filter to show the temporal signature more clearly. Time labels at the right side of the plot refer to the start of each exposure and correspond to the times of the data points in Figure 4. The third, fourth, and fifth spectra from the bottom (1.04, 1.88, and 2.72

seconds) were obtained during the burn and show the strong and prompt emission at 336 nm. The delay in growth of the 630-nm emission is apparent as is its persistence after the 336-nm emission has ceased.

The spatial-temporal characteristics of the 336- and 630-nm emissions are shown in Figures 6 and 7, respectively. For these figures spatial resolution in the direction of slit length has been retained by not summing over the twelve slit segments. At the shuttle range of 314 km from AMOS, each slit segment was illuminated by a region 0.45 km long. Supplemental telescope pointing data placed the shuttle at the zero of the distance scale in Figures 6 and 7 with a probable error ± 0.2 km. Positive distance is in the ram direction.

We note that the shuttle is moving in the ram direction at about 7.8 km/s and the initial velocity of the plume gases relative to the shuttle is near 3.5 km/s (Pickett et al., 1985; 1986). The 336-nm emission (Figure 6) appears to extend at least 2 km in front of the shuttle with very little emission in the wake. The 630-nm emission (Figure 7) rises slowly in the forward direction, spreads into the wake and persists for several seconds after the burn has ended. Both emissions indicate that the exhaust-gas is being carried along with the shuttle. The shuttle moves forward several plume lengths per second; nevertheless the emission comes from the region ahead of the shuttle even after the firing ceases. The extension of the 630-nm emission into the wake is a measure of the "drag" which finally separates the thruster gases from the orbiter.

The spectra of Figures 3 through 7 are plotted in relative units because of the various ways the data have been summed to extract spectral, temporal and spatial information. From the spectrum at 2.72 sec, we have estimated the peak brightness at the center of the interaction cloud (about 1 km ahead of the shuttle) to be about 10 kR in the 630-nm feature (or 2.5×10^{-10}

watts/cm²/sr).

The 630-nm region emission is not necessarily confined to the O (¹D→³P) transition. We estimate that as much as 20% of the emission within the 30-nm band could be from other plume emission sources. Intensity estimates through the three phases of the experiment are given in Table 1. There is some uncertainty about the intensity of the perpendicular burns. We have adopted the intensity from the nadir burn since it registered the highest intensity or a lower limit for the perpendicular direction. In earlier, visible-wavelength (S-20 photocathode) images the nadir and zenith burns have appeared to be approximately equal in brightness; in this experiment we suspect that the lower intensity seen by the spectrograph during the zenith burn is the result of observing a dimmer part of the plume because of a difference in pointing.

DISCUSSION

A. 615-645 nm Feature: We ascribe this feature to the O(¹D → ³P) transition for the following reasons:

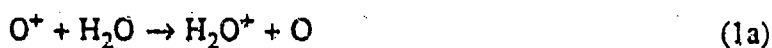
- a. Its shape agrees closely with that predicted by convolving the spectral-response function of the instrument with doublet lines at 630 and 636.4-nm;
- b. Its shape fits the night-sky airglow spectrum shown in Figure 3;
- c. The assignment was subsequently confirmed by a higher-resolution measurement from the STS-43 experiment on August 7, 1991, as shown in the inset in Figure 3; and
- d. A forbidden transition explains the emission delay

B. Origin of O(¹D): Two mechanisms for generating the O(¹D) are proposed:





where X is any exhaust species with sufficient kinetic energy to excite the O(¹D). Reactions (1) and (2) are endoergic at room temperature by ~ 1 and ~ 2 eV, respectively. When the orbital velocity (i.e. the relative velocity of the initial O or O⁺) and the velocity of the exhaust are summed vectorially the center-of-mass collision energy is sufficient to overcome the energy barriers in the ram and perpendicular burns, as long as X is a species of a molecular mass comparable to that of O. The cross sections for these reactions have not been measured because of the long radiative lifetime of O(¹D). However, the cross section for the reaction:



where the state of O is not determined, has been measured (Heninger et al., 1989; Dressler et al., 1990). More recently the kinetic energies of the charged products of reaction (1a) have been measured (Dressler et al., 1991), and from these measurements one can obtain an indication that at least some of reaction (1a) may proceed via (1). In the analysis of the 630-nm feature we have used the *total* measured rate coefficient, knowing that this is a maximum. Since even with this rate coefficient, the charge-exchange channel contributes only 10% to the O(¹D), the error introduced is not very large.

For the cross section for reaction (2) we have used the recently calculated data by Sun and Dalgarno (1992). Sun and Dalgarno (1992) fitted the quenching rate coefficient to an expression of the type $k_q = (A + B\sqrt{T} + CT) \times 10^{-12} \text{ cm}^3 \text{ molecule}^{-1} \text{ s}^{-1}$. We fitted their data to an excitation rate coefficient of the form $k_e = 4.9 \times 10^{-12} e^{(-22800/T)} \text{ cm}^3 \text{ molecule}^{-1} \text{ s}^{-1}$. For the deactivation of O(¹D):





we have used the data reported by Abreu et al. (1986) for reaction (3), where M is N₂ or O. Published data indicate that $k_3(\text{N}_2)$, i.e. the deactivation rate constant when M is N₂ (Link et al., 1981; Link and Cogger, 1988) is 2.3×10^{-11} , while $k_3(\text{O}) = 8.0 \times 10^{-12}$ molecules cm³ s⁻¹. Assuming microscopic reversibility, we then estimate the rates of the reverse, endothermic reactions to be $k_3'(\text{N}_2) = 2.3 \times 10^{-11} \exp(-22800/T)$, and $k_3'(\text{O}) = 8.0 \times 10^{-12} \exp(-22800/T)$ molec cm³ s⁻¹. In the calculations discussed below we use $k_2(\text{H}_2\text{O}) = k_2(\text{N}_2)$ for reaction (2). Table 2 presents a summary of the rate constants used in the analysis of the 630 nm feature.

C. Temporal and Spatial Characteristics: Figures 4 and 7 show the intensity of this emission as a function of time after initiation of burn and as a function of distance from the spacecraft. It is clear from Figure 4 that the O(¹D) intensity builds up slowly, requiring approximately 3 seconds to reach a maximum. After the burn, the emission continues for at least 5 seconds after engine shutoff. Figure 7 also shows the O(¹D) to extend as much as 2 km ahead of the orbiter and as much as 3 km behind.

D. Return Flux of Molecules to Spacecraft: Besides the temporal behavior of the 630-nm emission, the data of Figure 7 show that by 2.72 s, O(¹D) begins to be swept into the wake of the spacecraft, and this process continues after termination of the firing at 3 s. As late as 6.92s (3.92 s after burn termination) the spacecraft continues to overtake the O(¹D), which can be seen as far as 2 km behind the spacecraft. A consequence of this observation is that O(¹D), and by inference, perhaps other ram-directed exhaust species strike the surfaces of the spacecraft. This transport is a complex function of the radiative lifetime, elastic scattering, deactivation, and chemical reaction of O(¹D). The fact that we see O(¹D) behind the spacecraft and the fact that

its concentration decreases almost exclusively by collisional deactivation or reaction rather than radiation suggest that the products of its reaction will be present both ahead and behind the spacecraft. This observation can be generalized to other reactive species, where the concentration of the products is determined by the competition between radiative relaxation and collisional (both reactive and nonreactive) scattering.

For example, the fast reaction with H_2O , reaction (4) above, has a rate coefficient of $2.2 \times 10^{-10} \text{ cm}^3 \text{ s}^{-1}$ (Gericke and Comes, 1981; Demore et al., 1990). Assuming that H_2O represents 33% of the exhaust, and assuming that its density is $\sim 10^9 \text{ cm}^{-3}$, the time constant for this reaction turns out to be $\sim 5 \text{ s}$. An exhaust product with a slower rate coefficient would have a correspondingly longer time constant. For example, a potential product of hydrazine fuels is NH_2 ; its primary reaction will be with atmospheric O:



whose rate coefficient is $\sim 1 \times 10^{-11} \text{ cm}^3 \text{ s}^{-1}$ (Westley et al., 1990); the time constant against reaction with ambient O atoms, assuming again the local density of NH_2 to be $\sim 10^9 \text{ cm}^{-3}$, is $\sim 100 \text{ s}$, i.e. 20 times that of reaction (4).

E. Code calculations and comparison with data: The *SOCRATES* Code (Elgin et al., 1990) was used to calculate a number of the parameters discussed above, namely, the relative contribution of reactions (1) and (2), the effect of angle of attack on the spatial distribution of the relative distribution of emission rates of the 630-nm doublet, and the radiance in this line as a function of time. We used the appropriate atmospheric densities for altitude (290 km) and time (1326 UT), namely $[\text{O}^+] = 3.7 \times 10^5 \text{ cm}^{-3}$ and $[\text{O}] = 1 \times 10^9 \text{ cm}^{-3}$. Briefly, *SOCRATES* is a *Monte Carlo* Code developed to calculate and predict the effect of interactions of spacecraft surfaces

and atmospheres with the natural environment in low earth orbit. The code includes scattering and chemical reactions. The rate coefficients used for the reactions forming and destroying $O(^1D)$ are given in Table 2. We briefly present below the results of the calculations from the more detailed description of this work available elsewhere (Elgin et al., 1990).

i. *Angle of Attack:* The calculated maximum relative column emission rates at 630-nm were 6.8, 4.3, and 1.0 kR for the ram, perpendicular, and wake burns, respectively. These values compare favorably with the observed relative signals given in Table 1 and so lend credence to the calculational procedure. Figure 8 shows plots of the radiant intensity of the $O(^1D) \rightarrow O(^3P)$ photons as a function of time at different angles of attack. The differences in emission intensities are a direct result of the variation in available collision energy for the three cases.

ii. *Time of Maximum Intensity:*

Figure 8 shows the calculated total emission rate history for the three burns. A plateau is predicted approximately 2.5 seconds into the burns, in substantial agreement with the data. The relatively slow decay after engine shutdown in the calculations is predominantly due to residual atmospheric collisions that continue to excite the $O(^1D)$ even after the plume has left the immediate vicinity of the vehicle, and the transport of $O(^1D)$, previously excited, into the field of view.

iii. *Relative Contributions of Reactions (1) and (2):*

The relative contributions of the collisional and charge-exchange mechanisms are shown for the ram burn in Figure 9. The collisional mechanism is dominant throughout the burn. The collisional mechanism remains the dominant one even for the wake burn, but the ratio goes down from approximately 27 to 8 as the mean flow energy is reduced. After the engine shutdown, the

charge-exchange mechanism decays at a faster rate as the H_2O molecules leave the vicinity of the vehicle, while the collisional mechanism is maintained for a while via purely atmospheric collisions.

iv. *Predictions of emissions from the $\text{O}(^1\text{S}) \rightarrow \text{O}(^1\text{D})$ Transition:* A reaction similar to reaction (2) can be used to excite the $\text{O}(^1\text{S})$ in the ram direction. In this event, emission from the $\text{O}(^1\text{S}) \rightarrow \text{O}(^1\text{D})$ at 557 nm would be expected. We calculated profiles for this emission using the rate coefficients given by Krauss and Neumann (1975) using the *SOCRATES* Code. These calculations lead to a total emission due to $\text{O}(^1\text{S}) \rightarrow \text{O}(^1\text{D})$ which was a factor of 10 larger than that due to $\text{O}(^1\text{D}) \rightarrow \text{O}(^3\text{P})$. The data indicate that, in fact, $\{\text{O}(^1\text{S}) \rightarrow \text{O}(^1\text{D})\} / \{\text{O}(^1\text{D}) \rightarrow \text{O}(^3\text{P})\} \sim 0.1$. We conclude from this that the rate coefficient given by Krauss and Neumann (1975) is not correct; an adjustment downwards by a factor of 100 is required to reconcile the observations.

ACKNOWLEDGEMENTS

We wish to thank Ms. Kalynda Behrens for developing the software which made these measurements possible. We thank the reviewers for pointing out an error in the calculation of the rate coefficients used in the model. We also thank Dr. W. G. D. Frederick of SDIO for supporting this work under PMA 110501 and USAF under PE 63410F.

Table 1

PEAK COLUMN EMISSION RATES

Band Region (nm)	Peak Intensity (kR)			Assignment
	Wake	Perp	Ram	
615-645	1	7	10	Blended OI + ?
630.0 + 636.4 lines	1	5	8	O($^3P \rightarrow ^1D$)
665-695	7	8	12	NH Second Order

TABLE 2

RATE COEFFICIENTS OF REACTIONS

$$k = AT^n e^{(-E_a/kT)}$$

Reaction	A	n	E ₂ kcal/mol	Reaction ΔH kcal/mol
O(³ P) + N ₂ → O(¹ D) + N ₂	1.28x10 ⁻¹¹	0.00	45.3	45.3
O(³ P) + O(³ P) → O(¹ D) + O(³ P)	4.9X10 ⁻¹²	0.00	45.3	45.3
O(³ P) + H ₂ O → O(¹ D) + H ₂ O	1.28x10 ⁻¹²	0.00	45.3	45.3
O(¹ D) + N ₂ → O(³ P) + N ₂	2.3x10 ⁻¹¹	0.00	0	-45.3
O(¹ D) + O(³ P) → O(³ P) + O(³ P)	8.0x10 ⁻¹²	0.00	0	-45.3
O(¹ D) + H ₂ O → O(³ P) + H ₂ O	2.3x10 ⁻¹¹	0.00	0	-45.3
O(¹ D) + H ₂ O → OH + OH	2.2x10 ⁻¹⁰	0.00	0	-28.3
O ⁺ + H ₂ O → O(¹ D) + H ₂ O ⁺	<2.3x10 ⁻⁹	-0.03	23.0	23.0

FIGURE CAPTIONS

Figure 1 - A graphic representation of the experiment as seen with the ISIT imager, with ram and wake interactions shown. The dimensions of the shuttle and slit are exaggerated. The Shuttle/plume and coordinate system move in the positive direction at 7.8 km/sec. The slit projection is shown for the 12 consecutive spatial-sample regions.

Figure 2 - Geometry of the engine firing measurements.

Figure 3 - A composite of three spectra. 1) The night airglow recorded in 180 seconds. 2) The plume spectrum from STS-41 summed over the 3-second burn. 3) The plume spectrum from the similar STS-43 experiment using a higher-resolution spectrograph to confirm the identification of the atomic line. Integration regions for Fig. 4 are indicated.

Figure 4 - Temporal variation of relative intensity in the full slit through the duration of the experiment. The spectrum was integrated over the two regions 615-645 nm and 665-695 nm noted in Figure 3. These were relative intensities since the slit is not filled by the emission sources. Thruster direction sequence is shown at top of the plot.

Figure 5 - The full-slit spectral samples from the beginning of the ram burn to the beginning of the wake burn. The data have been smoothed to emphasize the temporal changes in spectral content. The spectra are offset vertically and tagged with their start integration time relative to the beginning of the ram burn. Intensities are again relative since the slit filling factor varies with time.

Figure 6 - Spatial and temporal variation in the emission from the 665-695 nm spectral region. The peak intensity reported in Table 1 was derived from the spectrum starting at 2.72 s about 1 km forward of the shuttle position.

Figure 7 - Spatial and temporal variation in the emission from the 615-645 nm spectral region.

The ram-burn peak intensity reported in Table 1 was derived from the spectrum starting at 2.72 s about 1 km forward of the shuttle.

Figure 8 - The calculated temporal dependence of the $O(^1D)$ emission for the three burn orientations. This emission is integrated spatially over a region of about 6 x 6 km around the shuttle.

Figure 9 - The relative contributions calculated by SOCRATES of the collisional and charge-exchange mechanisms to $O(^1D)$ production rate as a function of time for the ram burn.

REFERENCES

- Abreu, V. J., J. H. Yee, S. C. Solomon, and A. Dalgarno, The Quenching Rate of $O(^1D)$ by $O(^3P)$, *Planet. Space Sci.*, **34**, 1143-1145, 1986.
- Broadfoot, A. L., B. R. Sandel, R. A. Viereck, D. J. Knecht, and E. Murad, An Instrument to Study Spacecraft Interactions, *Applied Optics*, *In Press*.
- DeMore, W. B., S. P. Sander, D. M. Golden, M. J. Molina, R. F. Hampson, M. J. Kurylo, C. J. Howard, A. R. Ravishankara, Chemical Kinetics and Photochemical Data for Use in Stratospheric Modeling. Evaluation number 9, *JPL Publication 90-1*, Pasadena, CA, 1990.
- Dressler, R. A., J. A. Gardner, R. H. Salter, F. J. Wodarczyk, and E. Murad, The Reaction of N_2^+ with H_2O and D_2O , *J. Chem. Phys.*, **92**, 1117-1125, 1990.
- Dressler, R. A., J. A. Gardner, D. C. Cooke, and E. Murad, Analysis of Ion Densities in the Vicinity of Space Vehicles, *J. Geophys. Res.*, **96**, 13795-13806, 1991.
- Ehlers, H. F. K., Space Shuttle Orbiter Molecular Environment Induced by the Supplemental Flash Evaporator System, *J. Spacecraft Rockets*, **23**, 379-385, 1986.
- Elgin, J. B., D.C. Cooke, M. Tautz, and E. Murad, Modeling of Atmospherically-Induced Optical Contamination from Space-Borne Measurements, *J. Geophys. Res.*, **95**, 12197-12208, 1990.
- Gericke, K.-H.; F. J. Comes, Energy Partitioning in the Reaction $O(^1D) + H_2O \rightarrow OH + OH$. The Influence of $O(^1D)$ Translational Energy on the Reaction Rate Constant, *Chem. Phys. Lett.*, **81**, 218 (1981).
- Heninger, M., S. Fenistein, G. Mauclaire, R. Marx, and E. Murad, Review of the Reaction of O^+

- with H₂O and Its Bearing on Composition Measurements from the Space Shuttle, *Geophys. Res. Lett.*, **16**, 139-141 (1989)
- Koch, D. G., G. J. Melnick, G. G. Fazio, G. H. Rieke, F. J. Low, W. Hoffman, E. T. Young, E. W. Urban, J. P. Simpson, F. C. Witteborn, T. N. Gautier, III, and W. Poteet, Overview of Measurements from the Infrared Telescope on Spacelab 2, *Astro. Lett. Commun.*, **27**, 211-222, 1988.
- Krauss, M., and D. Neumann, On the Interaction of O(¹S) with O(³P), *Chem. Phys. Lett.*, **36**, 372-375, 1975.
- Link, R. J., J. C. McConnell, and G. G. Shepard, A Self-consistent Evaluation of the Rate Constants for the Production of the O 6300 A Airglow, *Planet. Space Sci.*, **29**, 589-593, 1981.
- Link, R., and L. L. Cogger, A Reexamination of the O I 6300 A Nightglow, *J. Geophys. Res.*, **93**, 9883-9892, 1988.
- Murad, E., D. J. Knecht, R. A. Viereck, C. P. Pike, D. C. Cooke, I. L. Kofsky, C. A. Trowbridge, D. L. A. Rall, G. Ashley, L. Twist, J. B. Elgin, A. Setayesh, A. T. Stair, Jr., J. E. Blaha, Visible Light Emission Excited by Interaction of Space Shuttle Exhaust with the Atmosphere, *Geophys. Res. Lett.*, **17**, 2205, 1990.
- Pickett, J. S., G. R. Murphy, W. S. Kurth, C. K. Goertz, and S. D. Shawhan, Effects of Chemical Releases by the STS-3 Orbiter on the Ionosphere, *J. Geophys. Res.*, **A90**, 3487-3497, 1985.
- Pickett, J. S., G. B. Murphy, and William S. Kurth, Gaseous Environment of the Shuttle Early in the Spacelab 2 Mission, *J. Spacecraft & Rockets*, **25**, 169, 1988.

- Radzig, A. A., and B. M. Smirnov, *Reference Data on Atoms, Molecules and Ions*, Springer Verlag, Heidelberg, 1985.
- Scialdone, J. J., Abatement of Gaseous and Particulate Contamination in a Space Instrument, in *Spacecraft Contamination: Sources and Prevention*, Edited by J. A. Roux and T. D. McCay, Volume 91, Progress in Astronautics and Aeronautics, P. 108, AIAA, New York, 1984.
- Sun, Y., and A. Dalgarno, Collisional Excitation of Metastable $O(^1D)$ Atoms, *J. Chem. Phys.*, 96, 5017-5019, 1992.
- Trinks, H., and R. J. Hoffman, Experimental Investigation of Bipropellant Exhaust Plume Flowfield, Heating, and Contamination and Comparison with the CONTAM Computer Model Predictions, in *Spacecraft Contamination: Sources and Prevention*, Edited by J. A. Roux and T. D. McCay, Volume 91, Progress in Astronautics and Aeronautics, pp. 261-292, AIAA, New York, 1984.
- Westley, F., J. T. Herron, R. J. Cvetanovic, R. F. Hampson, W. G. Mallard, *NIST Chemical Kinetics Database, Version 2.0*, National Institute of Science and Technology, Washington, DC, 1990.
- Wulf, E., and U. von Zahn, The Shuttle Environment: Effects of Thruster Firings on Gas Density and Composition in the Payload Bay, *J. Geophys. Res.*, 91, 3270-3278, 1986.

Schematic representation - Cloud shape is approximate and is for a nominal altitude of ~ 300 km. Shuttle and slit are exaggerated in size.

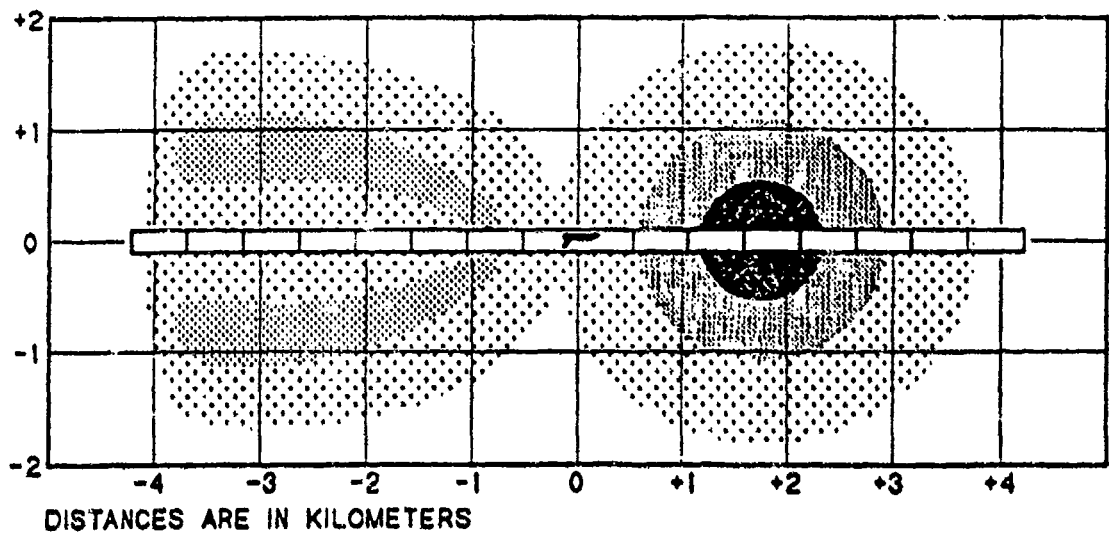


FIGURE 1

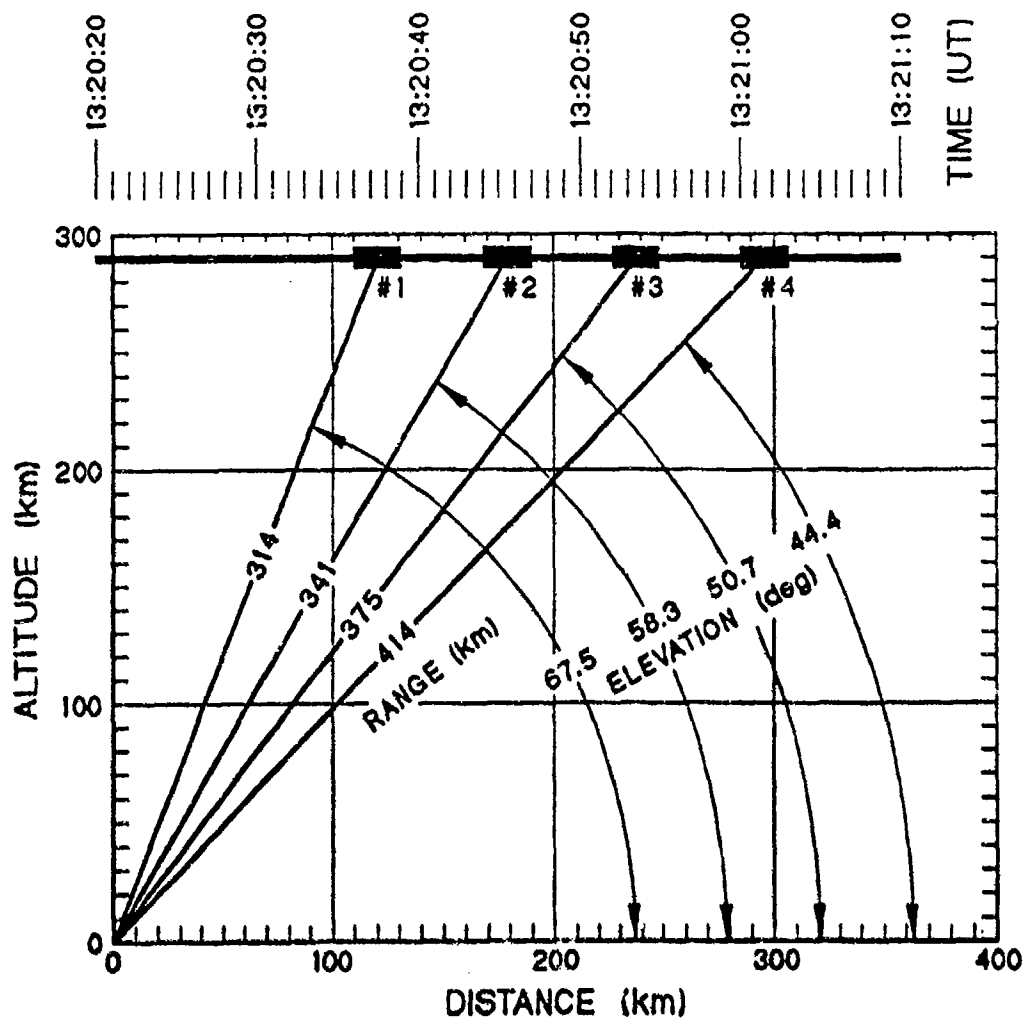


FIGURE 2

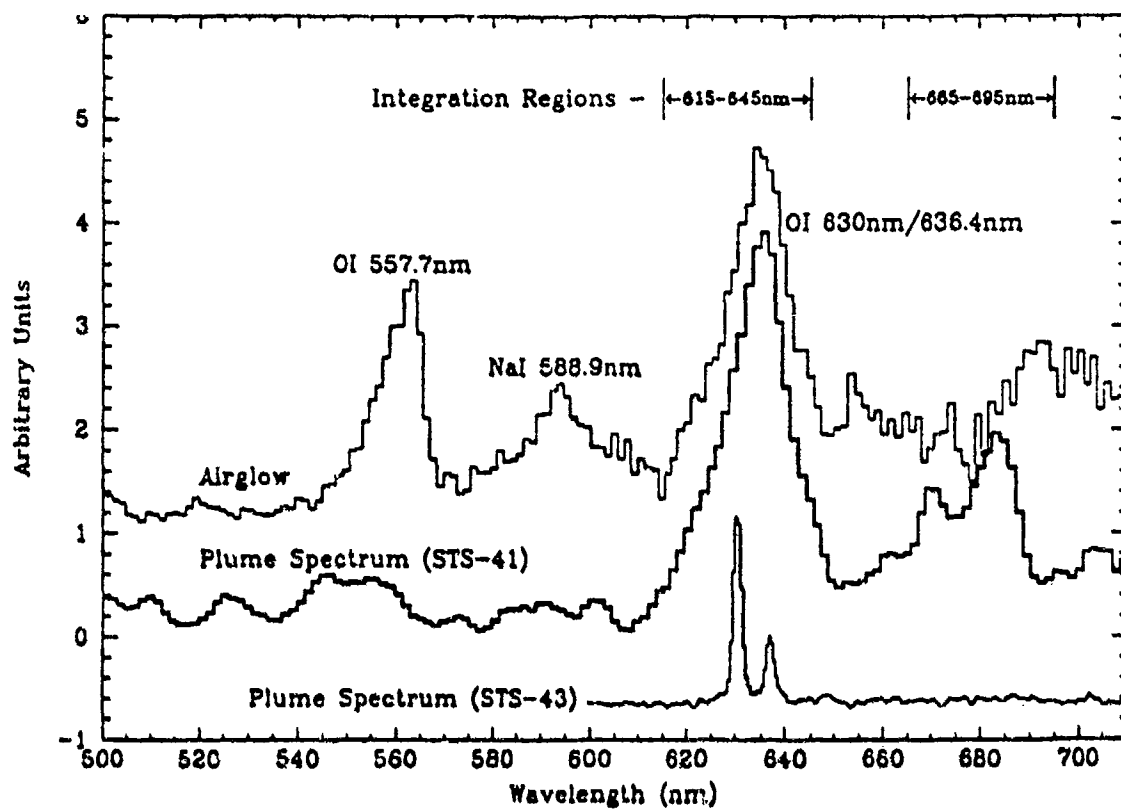


FIGURE 3

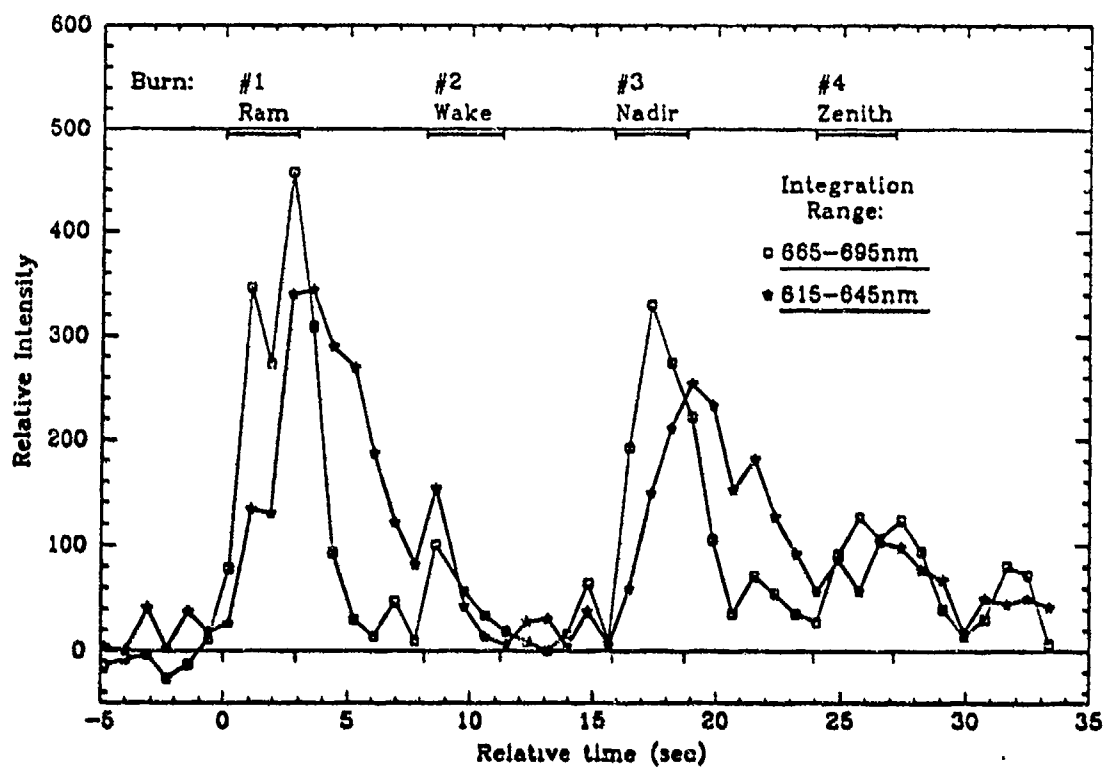


FIGURE 4

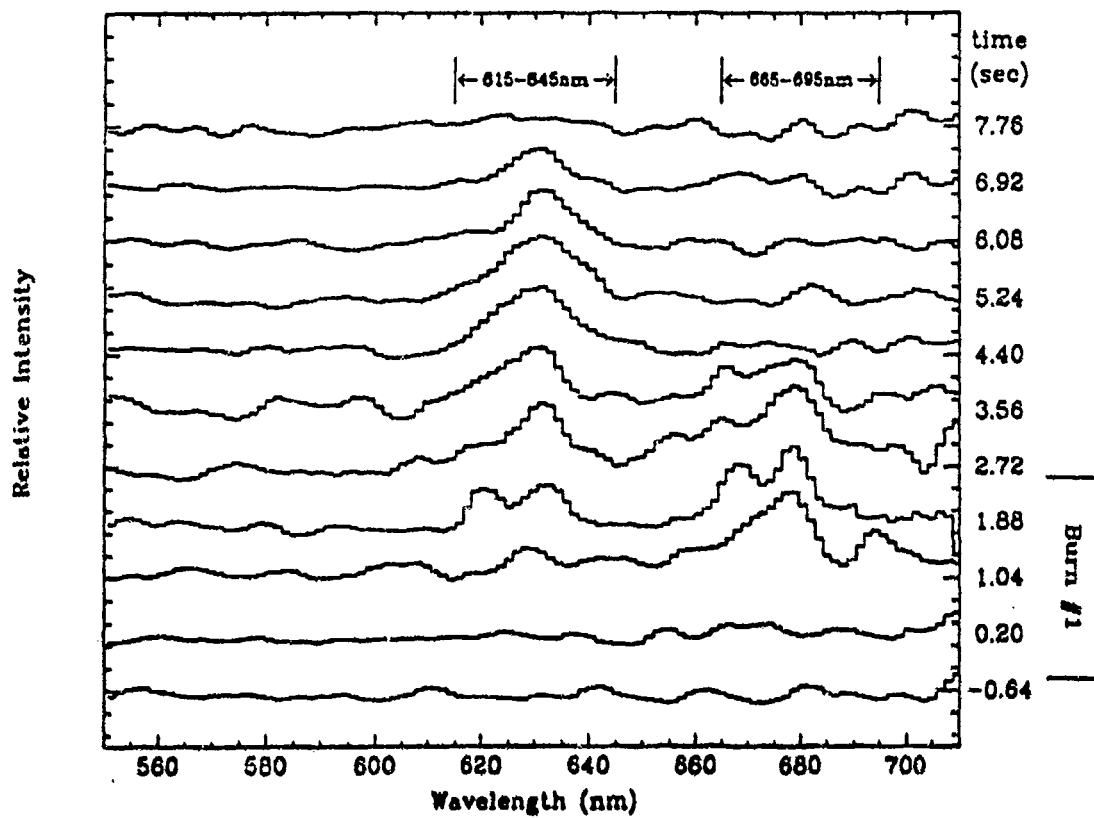


FIGURE 5

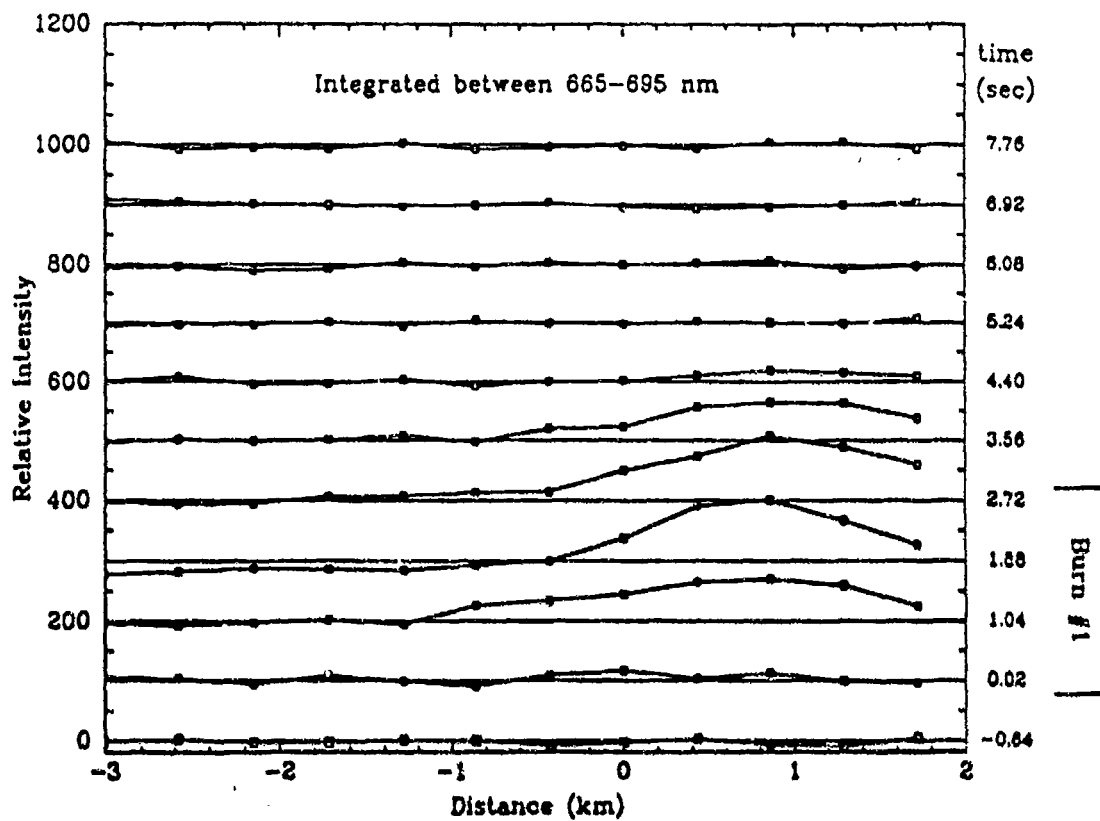


FIGURE 6

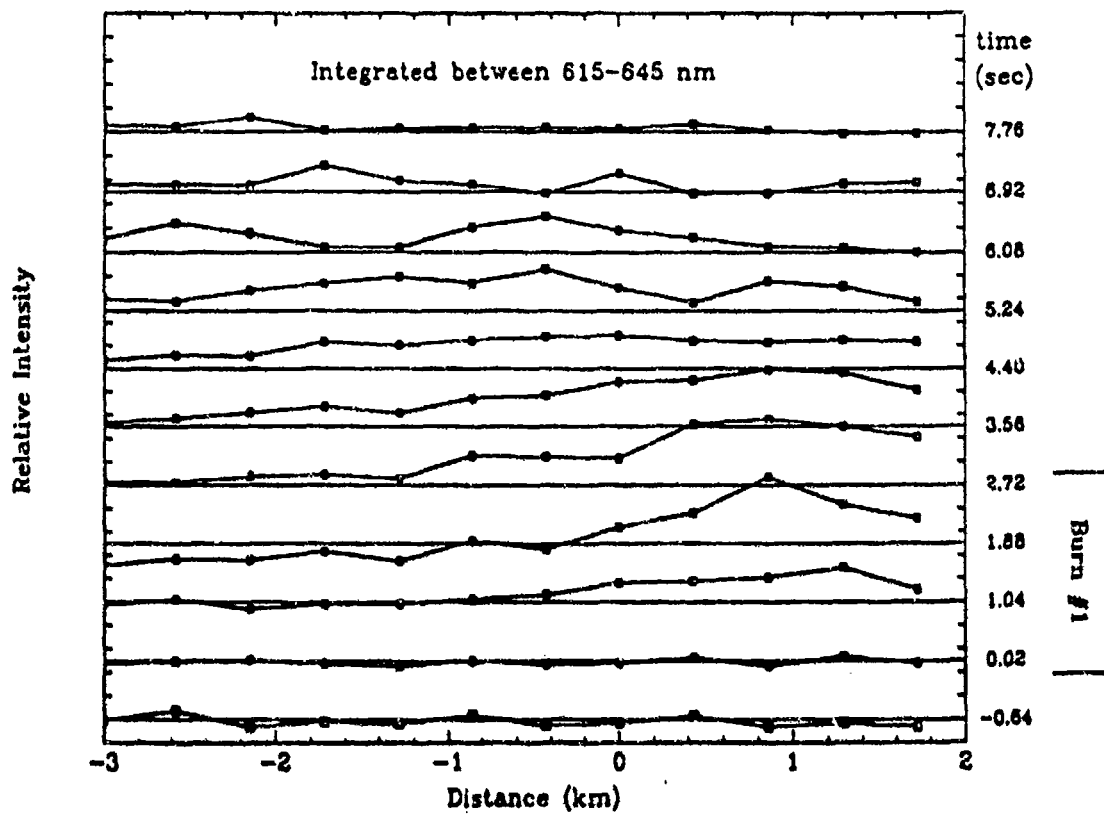


FIGURE 7

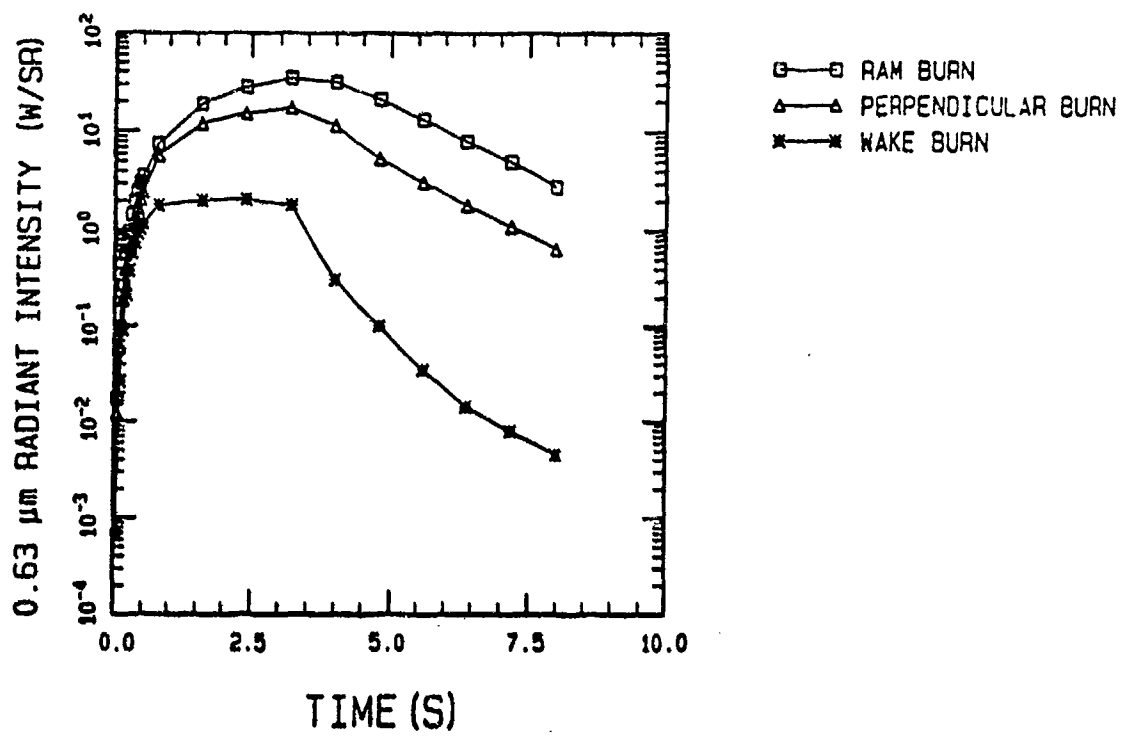


FIGURE 8

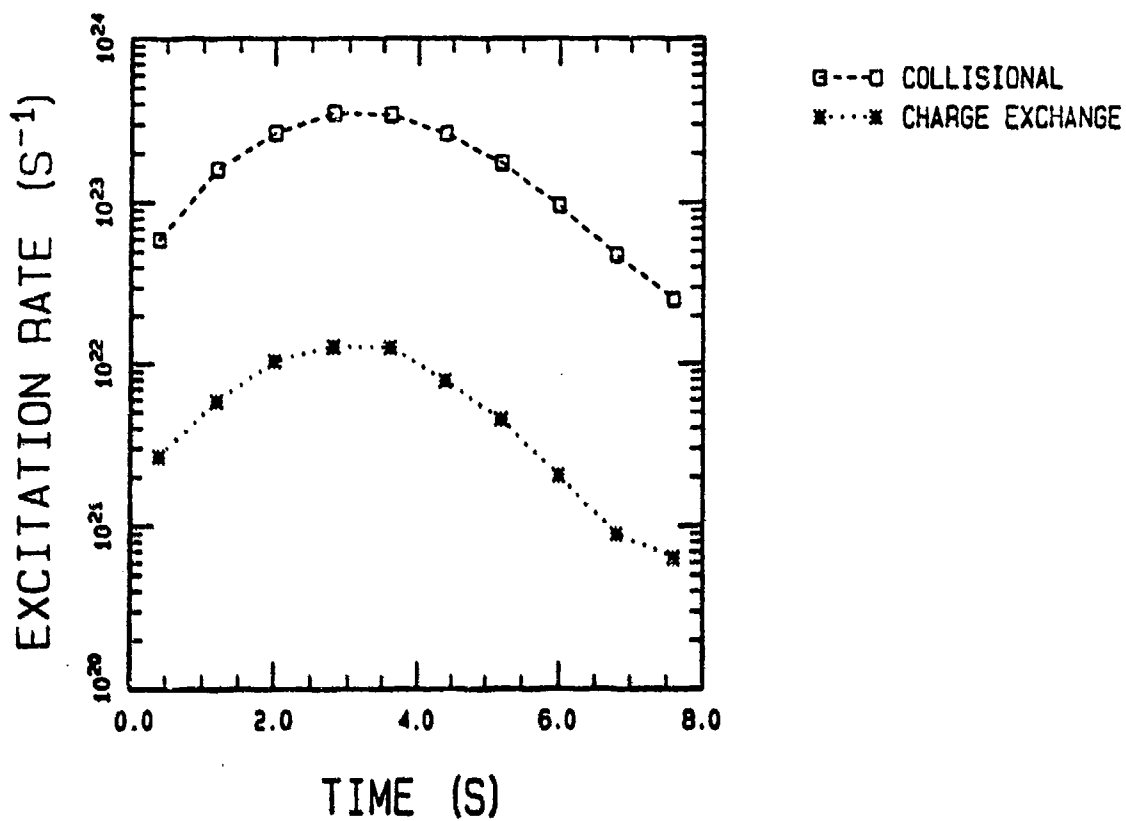


FIGURE 9

APPENDIX B
Final Report, SFRC F19628-88-K-0028

A Study of the NH Interaction

COMMENTS ON THE LIKELY MECHANISMS INVOLVED IN SHUTTLE-GLOW

JOSEPH W. CHAMBERLAIN

MAY 9, 1990

TYPES of GLOW. For any particular configuration of spacecraft and environment, there may well be more than one physical mechanism acting at one time. In addition, there are glows associated with space vehicles in distinctly different configurations. They include (1) ram surface glow; (2) thruster (gas-phase) glow, following thruster firings; and (3) "cloud (gas phase) glow", observed when looking away from the surface (without any thruster activity).

METHODS of OBSERVATION. Some early observations were made by ground-based telescopic equipment at Maui by Witteborn *et al* (1974), and they showed an infrared continuum glow that seemed to extend tens of meters from the Shuttle. The reported intensity seems much too bright in view of more recent Shuttle measurements. Shuttle observations, made with orbiter television cameras and still-camera pictures, have consistently shown a glow on the aft Shuttle surfaces facing into the velocity vector, as had previously been seen on AE satellites. Yee and Dalgarno (1986) derived intensities from STS-3 of about 30 kR, and the glow decreased away from the surface with a $1/e$ scale length of 20 cm; from this, they inferred a radiative lifetime for the emitting molecules of 0.67 msec.

SPECTRUM 1: RED CONTINUUM. Extensive observations of Shuttle-related glow have been made by Mende *et al* (1984, 1985, 1985, 1987, for example). Some spectra with low spectral resolution showed a red, structureless

glow extending away from the vertical stabilizer. There may have been problems here with scattered airglow emission lines. The optical detection equipment was significantly upgraded for observations on STS-41D. With spectral resolution of 34A, the continuous spectrum peaked at 6800A, and no spectral features were apparent.

The picture that emerges is one of NO₂ re-association spectrum in the red, produced when a mono-molecular layer of NO sticks to the surface and forms NO₂ with ramming atmospheric O. Presumably, the excess energy available breaks the bond of NO₂ with the surface, accounting for the stand-off glow above the Shuttle surface.

SPECTRUM 2: THE ISO/CLOUD GLOW. A confused array of spectra was obtained with an "Imaging Spectrometric Observatory" aboard STS-9/SPACELAB, and analyzed by Torr and Torr (1985). The spectral resolution was moderately high (3 - 6 A), with spectral ranges in the visual, near-UV, and far-UV. The importance of contamination is illustrated by the presence of various airglow and auroral emissions, but in addition the N₂ LBH band system (not a component of the natural atmospheric radiation) was found. The absence of any imaging data makes it impossible to ascertain the emission source: possibly it's the surface of the instrument baffles, but it is more likely the Shuttle-induced contaminant cloud, rather than a surface. The ISO also observed a glow in the wake of the Shuttle, again in contrast to a surface glow.

SPECTRUM 3: THRUSTER GLOW. When the thrusters are fired there appears an enhancement of the surface glow, followed by the creation of a glowing region apparently not associated with surface processes, which decays in tens of

seconds. Green *et al* (1985, 1986) suggest that the thrusters emit some 10^6 R from unburned fuel combining with ambient oxygen. Alternatively, oxygen may become adsorbed on the surface, creating a surface emission. Mende and Swenson (1985) found that Thruster glow decays 5 times more slowly on STS-8 at 220 km than did the glow studied by Green *et al* on STS-3 at 240 km. With 4 Å resolution, Kendall *et al* (1985, 1986) found the Thruster glow to be a continuum in the red, 6275 -- 6307 Å, and that the glow decayed slower on the surface than in the region over the surface. The latter effect suggests two distinct components.

MECHANISMS of EXCITATION. Green (1984) and Green and Murad (1986) have summarized the various sources that have been proposed for the vehicle glows, and Garrett *et al* (1988) have prepared a detailed review of the situation, which we will now both summarize and extend.

1. Simple Reactions That Produce Excited Neutrals [Slanger 1983, 1986]. Energetic neutral air molecules (N_2O) collide with the vehicle environment (consisting of local contaminants H_2O , H_2 , CO , CO_2 ; reflected ambient air; and thruster products, methylhydrazine $CH_3N_2H_3$ and N_2O_4 , and react at the vehicle surface. Possible reactants are vibrationally excited diatomic molecules such as NO , CO , and OH , which can radiate in the infrared, giving emission of the order of 10^5 R. The observed levels of contaminants may not be sufficient for the production of visual radiation by this mechanism. However, Green *et al* (1986) have examined the production of high vibrational overtones in NO (to $v' = 19$), which would produce radiation in the red and green.

2. Surface-Induced Decomposition of Molecules Followed by Association into Excited Electronic and Vibrational States [Green 1984, Green *et al* 1985]. This

mechanism is a variation on # 1:

N₂ dissociates on impact with the Shuttle surface; the N atoms then re-associate into high vibrational levels in the metastable A state (upper state of the Vegard-Kaplan, A --> X bands); then the electronic states cascade via A (high v') -> B (v") [a "reverse First Positive" transition] and then B --> A (ordinary First Positive) producing a variety of N₂ bands. Alas, there are some problems in matching the spectra from this mechanism with those observed as Shuttle-glow.

3. Plasma Excitation. Neutral atoms and molecules that impact a satellite surface have nearly the energy required to be collisionally ionized. In addition, with ions restrained by the Earth's magnetic field, the relative motions may reach the Alfvén critical ionization level and contribute to the ionization. Papadopoulos (1984) has advocated the beam plasma discharge for generating a glow; it involves two-stream instability between incoming ram and reflected ions. This instability generates electrostatic waves that heat the ambient electrons, producing a variety of N₂ and N₂⁺ band systems. The critical ionization velocity (CIV) or Alfvén mechanism has been advocated by Murad and associates. Kofsky (1984) has developed several phenomenological criticisms (especially dealing with the spectrum and geometrical distribution of the glow) against the discharge model. Although the association of enhanced ionization with visible glow suggested a causal link more recent work by Lai *et al* (1988) and Lai and Murad (1989) have indicated the relationship between the two phenomena is circumstantial, not causal, and that the CIV mechanism may arise from Shuttle exhaust.

4. Adsorption of O and O₂ on Surfaces. Prince (1985) has proposed a surface chemiluminescence model with an additional mechanism (transfer of an

electron from the Fermi level of the surface to the adsorbed, ambient species) contributing to the continuum emission. The mechanism is then a surface-aided chemiluminescence reaction with adsorbates, and it is probably sensitive to the surface material.

5. NO_2 Association Continuum. The association occurs between ambient O and NO, the latter occurring on the Shuttle surface from adsorption of ambient NO, by surface reactions of N and O, by O reaction with Shuttle surface materials, or from thruster exhausts containing $\text{CH}_3\text{N}_2\text{H}_3$ (mono-methylhydrazine), which is a hypergolic fuel when mixed with N_2O_4 .

6. Surface Bulk Reactions: Material Loss or Composition Change. Along with Shuttle glow, the early missions also revealed oxygen erosion of satellite surfaces. The topic is reviewed by Leger and Visentine (1986), who establish that oxygen can remove as much as 0.001 cm of material during a typical Shuttle mission. The process is very dependent on the specific materials. Green and Murad (1986) reported that NO, CO, SiO, and CN could be released with sufficient excitation to emit.

RECENT ADVANCES IN UNDERSTANDING SHUTTLE-GLOW. Conway *et al* (1987) have established that the LBH bands of N_2 , previously interpreted as airglow, is excited by the interaction of the vehicle with the ambient atmosphere. They found that the vibrational distribution is sharply peaked at $v' = 0$. The altitude variation of the emission suggested to these authors a three-stage process in which N_2 is first adsorbed, then collisionally excited, and finally desorbed by ambient N_2 collisions. However, reaction rates that seem physically reasonable failed to account quantitatively for the observed intensities.

This work has been followed by the proposal by Kofsky (1988) and by Swenson and Meyerott (1988) that the emission results from the surface association of $N + N$. Further analysis of this mechanism has been carried out by Meyerott and Swenson (1990), who note that N in the ground term (4S) can populate the upper state of the LBH bands either (a) directly or (b) by cascade from higher excited states of N_2 . Gas phase association would populate up to about $v' = 4 - 6$, although surface interactions with the spacecraft will lower the vibrational population. The Meyerott-Swenson paper explores the (b) mechanism (i.e., cascading), particularly from the c'_4 state, which could be populated with the translational energy of ramming N on surface bound N in association. The cascade mechanism would populate the a state, $v' = 0 - 1$, directly. Their cascade mechanism predicts additional emissions around 3000Å (Gaydon-Herman band system) and around 958Å from the surface association. The latter can resonantly scatter in the spacecraft cloud and in atmospheric N_2 , resulting in extended spacecraft glows in low Earth orbit. Thus, we have specific, detailed predictions to compare with observations as yet unmade.

SHUTTLE - GLOW BIBLIOGRAPHY

AUTHORS	YEAR + JOURNAL REF	SUBJECT
BANKS, P M; WILLIAMSON, P R; RAITT, WJ	83, GRL 10, 118	ENVIRONMENT, GLOW
BERNHARDT, PA; DUNCAN, LM; TEPLY, CA	88, SCIENCE 242, 1022	AIRGLOW, ARTIFICIAL
CLEMESHA, B R; TAKAHASHI, H; SAHAI, Y	87, PLANET SPACE SCI 35, 1367	ENVIRONMENT, GLOW - ROCKET
CONWAY, R R; MEIER; STROBEL; HUFFMAN	87, GRL 14, 628	EXCITATION, N2 LBH
CONWAY, R R; MEIER; STROBEL; HUFFMAN	87, GRL 14, 628	SPECTRUM, N2 LBH
DALGARNO, A	85, SUMMARY, NASA CP 2391,	EXCITATION, REVIEW
DALGARNO, A	85, SUMMARY, NASA CP 2391,	ENVIRONMENT, GLOW/GASEOUS
DRESSLER, R A et al (4)	90, J CHEM PHYS 92(2), 1117	CHARGE EXCHANGE, N2+ & WATER
GARRETT, H B; CHUTJIAN, A; GABRIEL, S	88, J. SPACECRAFT 25, 321	EXCITATION, REVIEW
GARRETT, H B; CHUTJIAN, A; GABRIEL, S	88, J. SPACECRAFT 25, 321	ENVIRONMENT, GLOW
GREEN, B D	84, GRL 11, 576	EXCITATION, CHEMICAL
GREEN, B D; MURAD, E	86, PLANET. SPACE SCI 34, 219	EXCITATION, REVIEW
GREEN, B D; CALEDONIA; WILKERSON	85, J SPACECRAFT 22, 500	ENVIRONMENT, GLOW
GREEN, B D; RAWLINS; MARINELLI	86, PLANET SPACE SCI 34, 879	EXCITATION, CHEMICAL
GREEN, B D	84, GRL 11, 576	RADIATIVE RECOMBIN. N2 CASCADING
GREEN, B D; CALEDONIA, G E; WILKERSON, T D	85, J SPACECRAFT 22, 500	ENVIRONMENT, GLOW/GASEOUS
KENDALL, D J W + 4 OTHERS	85, NASA CP-2391, 2d WORKSHOP, 63-74	SPECTRUM
KENDALL, D J W + 5 OTHERS	86, PLANET. SPACE SCI 34, 1159	ENVIRONMENT, GLOW
KOCK, D G; et al (7)	87, ADV SPACE RES 7, (5)211	ENVIRONMENT, GLOW/GASEOUS
KOFSKY, I L	88, GRL 15, 241	EXCITATION, N2 LBH
KOFSKY, I L	84, RADIO SCIENCE 19, 578	EXCITATION, IONIZATION
LAI, S T; DENIG, W F; MURAD, E; MCNEIL, W J	88, PLANET SPACE SCI 36, 841	ENVIRONMENT, GASEOUS; IONIZATION
LAI, S T; DENIG, W F; MURAD, E; MCNEIL, W J	88, PLANET SPACE SCI 36, 841	EXCITATION, CHEMICAL
LAI, S T; MCNEIL, W J; MURAD, E	88, J GEOPHYS RES A93, 5871	ENVIRONMENT, GASEOUS; IONIZATION
LAI, S T; MURAD, E	89, PLANET SPACE SCI 37, 865	ENVIRONMENT, IONIZATION
LAI, S T; MURAD, E	89, PLANET SPACE SCI 37, 865	CIV EXCITATION
LAI, S T; MURAD, E; MCNEIL, W J	89, IEEE TRANS PLASMA SCI 17, 124	ENVIRONMENT, GASEOUS, IONIC
LAI, S T; MURAD, E; MCNEIL, W J	89, IEEE TRANS PLASMA SCI 17, 124	CIV EXCITATION
LANGHOFF, S; JAFFE, R; YEE, J; DALGARNO, A	83, GRL 10, 896	SPECTRUM, ON SYNTHETIC
LEGER, L G; VISENTINE, J T	86, J SPACECRAFT 23, 505	EXCITATION, MATERIALS
MENDE, S B; BANKS, P M; KLINGELSMITH	84, GRL 11, 527	ENVIRONMENT, GLOW, SURF MATERIAL
MENDE, S B; GARRIOTT, O K; BANKS, P M	83, GRL 10, 122	ENVIRONMENT, GLOW, RAM & THRUSTER
MENDE, S B; SWENSON, G R	85, NASA CP-2391, 2d WORKSHOP, 1-34	ENVIRONMENT, GLOW
MENDE, S B; SWENSON, G R; + 4 OTHERS	86, J SPACECRAFT 23, 189	ENVIRONMENT, GLOW/GASEOUS
MENDE, S B; SWENSON, G R; LLEWELLYN, E J	87, ADV. SPACE RES 7, (5)189	ENVIRONMENT, GLOW
MEYEROTT, R E; SWENSON, G R	90, PLANET. SPACE SCI 38, 555	SURFACE REACTIONS, N + N
MEYEROTT, R E; SWENSON, G R	90, PLANET. SPACE SCI 38, 555	EXCITATION, N2 LBH
MURAD, E	85, PLANET. SPACE SCI 33, 421	ENVIRONMENT, ION/NEUTRAL
MURAD, E	85, SPI CONF PROC. 6, 147	EXCITATION, REVIEW
MURAD, E	87, IN KINGSTON "RECENT STUDIES..."	CIV EXCITATION
MURAD, E	89, J. SPACECRAFT 26, 145	THERMOCHEMICAL INTERACTIONS
MURAD, E; LAI, S	86, J GEOPHYS RES A91, 13745	DISSOCIATIVE RECOMBINATION
MURAD, E; LAI, S	86, J GEOPHYS RES A91, 13745	RADIATIVE RECOMBINATION
ORIENT, O J; CHUTJIAN, A; & MURAD, E	90, PHYS. REV. 1 APR	SURFACE REACTIONS: O + CO; O + NO
PAPADOPOULOS, K	84, RADIO SCIENCE 19, 571	EXCITATION, PLASMA
PATERSON, W R, FRANK, L A	89, J GEOPHYS RES A94, 3721	ENVIRONMENT, PLASMA
PATERSON, W R, FRANK, L A	89, J GEOPHYS RES A94, 3721	ENVIRONMENT, GASEOUS H2O
PIKE, C P et al (4)	90, GRL 17, 139	WATER RELEASE
PRINCE, R H	85, GRL 12, 453	EXCITATION, CHEMILUMINESCENCE
SISKIND, D E; RAITT; BANKS; WILLIAMSON	84, PLANET SPACE SCI 32, 881	ENVIRONMENT, IONIZATION
SLANGER, T G	88, AFOSR PROG REP	SURFACE REACTIONS, GENERAL
SLANGER, T G	88, AFOSR PROG REP	SPECTRUM, NO2
SLANGER, T G	83, GRL 10, 130	SURFACE REACTIONS, ON PRODUCTION
SWENSON, G R; MENDE, S B; CLIFTON, K S	85, GRL 12, 97	RADIATIVE ASSOCIATION, NO2
SWENSON, G R; MEYEROTT, R E	88, GRL 15, 245	EXCITATION, N2 LBH

TENNYSON, PD; FELDMAN, PD; HENRY, RC	87, ADV SPACE RES (PREPRINT)	ENVIRONMENT, GLOW UV
TORR, D G [EDITORIAL]	83, GRL 10, 113	ENVIRONMENT, GLOW
TORR, M R	83, GRL 10, 114	ENVIRONMENT, GLOW
TORR, M R; TORR, D G	85, J. GEOPHYS. RES. 90, 1683	ENVIRONMENT, GLOW, SHUTTLE/ISO
TORR, M R; TORR, D G	88, GRL 15, 95	EXCITATION, COLLISIONAL
TORR, M R; TORR, D G; EUN, J W	85, J. GEOPHYS. RES. 90, 4427	SPECTRUM, N2 LBH
von ZAHN, U; MURAD, E	86, NATURE 321, 147	EXCITATION, REVIEW
von ZAHN, U; MURAD, E	86, NATURE 321, 147	RADIATIVE ASSOCIATION, NO2
von ZAHN, U; MURAD, E	90, GRL 17, 147	SODIUM, SOURCE IN E REGION
WITTEBORN, F G; O'BRIENT, K; CAROFF, L	75, NASA TM-85972	ENVIRONMENT, GLOW
YEE, J H; ABREU, V J	83, GRL 10, 126	SPECTRUM, CONTINUOUS
YEE, J H; ABREU, V J; DALGARNO, A	84, GRL 11, 1192	ENVIRONMENT, GLOW
YEE, J H; ABREU, V J; DALGARNO, A	05, GRL 12, 651	SURFACE REACTIONS, O2
YEE, J H; ABREU, V J; DALGARNO, A	85, GRL 12, 651	RADIATIVE ASSOCIATION, OH; NO2
YEE, J H; DALGARNO, A	86, J. SPACECRAFT 23, 635	ENVIRONMENT, GLOW
YEE, J H; DALGARNO, A	86, J. SPACECRAFT 23, 635	RADIATIVE LIFETIME

INDEX of SHUTTLE - GLOW RESEARCH

SUBJECT	AUTHORS	YEAR + JOURNAL REF
AIRGLOW, ARTIFICIAL	BERNHARDT, PA; DUNCAN, LM; TEPLY, CA	88, SCIENCE 242, 1022
CHARGE EXCHANGE, N2+ & WATER	DRESSLER, R A et al (4)	90, J CHEM PHYS 92(2), 1117
CIV EXCITATION	MURAD, E	87, in KINGSTON "RECENT STUDIES..."
CIV EXCITATION	LAI, S T; MURAD, E; McNEIL, W J	89, IEEE TRANS PLASMA SCI 17, 124
CIV EXCITATION	LAI, S T; MURAD, E	89, PLANET SPACE SCI 37, 865
DISSOCIATIVE RECOMBINATION	MURAD, E; LAI, S	86, J GEOPHYS RES A91, 13745
ENVIRONMENT, GASEOUS H2O	PATERSON, W R; FRANK, L A	89, J GEOPHYS RES A94, 3721
ENVIRONMENT, GASEOUS, IONIC	LAI, S T; MURAD, E; McNEIL, W J	89, IEEE TRANS PLASMA SCI 17, 124
ENVIRONMENT, GASEOUS; IONIZATION	LAI, S T; McNEIL, W J; MURAD, E	88, J GEOPHYS RES A93, 5871
ENVIRONMENT, GASEOUS; IONIZATION	LAI, S T; DENIG, WF; MURAD, E; McNEIL, WJ	88, PLANET SPACE SCI 36, 841
ENVIRONMENT, GLOW	WITTEBORN, F C; O'BRIENT, K; CAROFF, L	75, NASA TM-85972
ENVIRONMENT, GLOW	TORR, D G [EDITORIAL]	83, GRL 10, 113
ENVIRONMENT, GLOW	TORR, M R	83, GRL 10, 114
ENVIRONMENT, GLOW	BANKS, P M; WILLIAMSON, P R; RAITT, WJ	83, GRL 10, 118
ENVIRONMENT, GLOW	YEE, J H; ABREU, VJ; DALGARNO, A	84, GRL 11, 1192
ENVIRONMENT, GLOW	GREEN, B D; CALEDONIA; WILKERSON	85, J SPACECRAFT 22, 500
ENVIRONMENT, GLOW	MEHDE, S B; SWENSON, G R	85, NASA CP-2391, 2d WORKSHOP, 1-34
ENVIRONMENT, GLOW	KENDALL, D J W + 5 OTHERS	86, PLANET. SPACE SCI 34, 1159
ENVIRONMENT, GLOW	MEHDE, S B; SWENSON, G R; LLEWELLYN, E J	87, ADV. SPACE RES 7, (5)169
ENVIRONMENT, GLOW	GARRETT, H B; CHUTJIAN, A; GABRIEL, S	88, J. SPACECRAFT 25, 321
ENVIRONMENT, GLOW - ROCKET	CLEMESHA, B R; TAKAHASHI, H; SAHAI, Y	87, PLANET SPACE SCI 35, 1367
ENVIRONMENT, GLOW UV	TENNYSON, PD; FELDMAN, PD; HENRY, RC	87, ADV SPACE RES (PREPRINT)
ENVIRONMENT, GLOW, RAM & THRUSTER	MEHDE, S B; GARRIOTT, O K; BANKS, P M	83, GRL 10, 122
ENVIRONMENT, GLOW, SHUTTLE/ISO	TORR, M R; TORR, D G	85, J. GEOPHYS. RES. 90, 1083
ENVIRONMENT, GLOW, SURF MATERIAL	MEHDE, S B; BANKS, P M; KLINGELSMITH	84, GRL 11, 527
ENVIRONMENT, GLOW/GASEOUS	GREEN, B D; CALEDONIA, GE; WILKERSON, TD	85, J SPACECRAFT 22, 500
ENVIRONMENT, GLOW/GASEOUS	DALGARNO, A	85, SUMMARY, NASA CP 2391,
ENVIRONMENT, GLOW/GASEOUS	MEHDE, S B; SWENSON, G R; + 4 OTHERS	86, J SPACECRAFT 23, 189
ENVIRONMENT, GLOW/GASEOUS	KOCK, D G; et al (7)	87, ADV SPACE RES 7, (5)211
ENVIRONMENT, ION/NEUTRAL	MURAD, E	85, PLANET. SPACE SCI 33, 421
ENVIRONMENT, IONIZATION	SISKIND, D E; RAITT; BANKS; WILLIAMSON	84, PLANET SPACE SCI 32, 881
ENVIRONMENT, IONIZATION	LAI, S T; MURAD, E	89, PLANET SPACE SCI 37, 865
ENVIRONMENT, PLASMA	PATERSON, W R; FRANK, L A	89, J GEOPHYS RES A94, 3721
EXCITATION, CHEMICAL	GREEN, B D	84, GRL 11, 578
EXCITATION, CHEMICAL	GREEN, B D; RAWLINS; MARINELLI	88, PLANET SPACE SCI 34, 879
EXCITATION, CHEMICAL	LAI, S T; DENIG, WF; MURAD, E; McNEIL, WJ	86, PLANET SPACE SCI 36, 841
EXCITATION, CHEMILUMINESCENCE	PRINCE, R H	85, GRL 12, 453
EXCITATION, COLLISIONAL	TORR, M R; TORR, D G	88, GRL 15, 95
EXCITATION, IONIZATION	KOFKY, I L	84, RADIO SCIENCE 19, 578
EXCITATION, MATERIALS	LEGER, L G; VISENTINE, J T	86, J SPACECRAFT 23, 505
EXCITATION, N2 LBN	CONWAY, R R; MEIER; STROBEL; HUFFMAN	87, GRL 14, 628
EXCITATION, N2 LBN	SWENSON, G R; MEYEROTT, R E	88, GRL 15, 245
EXCITATION, N2 LBN	KOFKY, I L	88, GRL 15, 241
EXCITATION, N2 LBN	MEYEROTT, R E; SWENSON, G R	90, PLANET. SPACE SCI 38, 555
EXCITATION, PLASMA	PAPADOPOULOS, K	84, RADIO SCIENCE 19, 571
EXCITATION, REVIEW	MURAD, E	85, SPI CONF PROC. 8, 147
EXCITATION, REVIEW	DALGARNO, A	85, SUMMARY, NASA CP 2391,
EXCITATION, REVIEW	VON ZAHN, U; MURAD, E	88, NATURE 321, 147
EXCITATION, REVIEW	GREEN, B D; MURAD, E	88, PLANET. SPACE SCI 34, 219
EXCITATION, REVIEW	GARRETT, H B; CHUTJIAN, A; GABRIEL, S	88, J. SPACECRAFT 25, 321
RADIATIVE ASSOCIATION, NO2	SWENSON, G R; MEHDE, SB; CLIFTON, KS	85, GRL 12, 97
RADIATIVE ASSOCIATION, NO2	VON ZAHN, U; MURAD, E	88, NATURE 321, 147
RADIATIVE ASSOCIATION, OH; NO2	YEE, J H; ABREU, VJ; DALGARNO, A	85, GRL 12, 651
RADIATIVE RECOMBIN, N2, CASCADING	GREEN, B D	84, GRL 11, 578
RADIATIVE RECOMBINATION	MURAD, E; LAI, S	86, J GEOPHYS RES A91, 13745

SODIUM, SOURCE IN E REGION
SPECTRUM
SPECTRUM, CONTINUOUS
SPECTRUM, N2 LSH
SPECTRUM, N2 LSH

VON ZAHN, U; MURAD, E
KENDALL, D J W + 4 OTHERS
YEE, J H; ABREU, V J
TORR, M R; TORR, D G; EUN, J W
CONWAY, R R; MEIER; STROBL; HUFFMAN

90, GRL 17, 147
85, NASA CP-2391, 2d WORKSHOP, 63-74
83, GRL 10, 126
85, J. GEOPHYS. RES. 90, 4427
87, GRL 14, 628

SPECTRUM, NO2
SPECTRUM, OH SYNTHETIC
SURFACE REACTIONS, GENERAL
SURFACE REACTIONS, N + N
SURFACE REACTIONS, O2

SLANGER, T G
LANGHOFF, S; JAFFE, R; YEE, J; DALGARNO, A
SLANGER, T G
MEYEROTT, R E; SWENSON, R R
YEE, J H; ABREU, V J; DALGARNO, A

88, AFOSR PROG REP
83, GRL 10, 896
88, AFOSR PROG REP
90, PLANET. SPACE SCI 38, 555
85, GRL 12, 651

SURFACE REACTIONS, OH PRODUCTION
SURFACE REACTIONS: O + CO; O + NO
THERMOCHEMICAL INTERACTIONS
WATER RELEASE
ENVIRONMENT, GLOW
RADIATIVE LIFETIME

SLANGER, T G
ORIENT, O J; CHUTJIAN, A; & MURAD, E
MURAD, E
PIKE, C P et al (4)
YEE, J H; DALGARNO, A
YEE, J H; DALGARNO, A

83, GRL 10, 130
90, PHYS. REV. 1 APR
89, J. SPACECRAFT 26, 145
90, GRL 17, 139
86, J. SPACECRAFT 23, 635
86, J. SPACECRAFT 23, 635

APPENDIX C
Final Report, SFRC F19628-88-K-0028

Reprint from *Applied Optics*:

Application of the Intensified CCD to Airglow and Auroral Measurements

Application of the intensified CCD to airglow and auroral measurements

A. L. Broadfoot and B. R. Sandel

New detector technology exemplified by advanced CCD and intensified CCD (ICCD) systems have important advantages for both spectrographic and imaging research. However, to realize the full potential of this new technology, we must consider the detector and the optical system as a whole. It is frequently not enough to simply substitute an ICCD for an earlier detector; rather, to achieve optimum results, the optics must be adapted to the specific detector. Properly designed airglow spectrographs based on the ICCD detector offer the advantages of high throughput over a broad spectral range, precise wavelength stability, low noise, and compactness. Imagers having the wide field and the high sensitivity needed for airglow research are practical as well.

1. Introduction

Quantitative auroral and airglow spectral measurements were first made by photographic emulsions in spectrographs and cameras. These emulsions recorded a great deal of information, both spectral and spatial, but had several important limitations. Photographic plates were slow, had a limited spectral range, and were difficult to interpret quantitatively. Early electronic detection systems, such as the vidicon and image orthicon developed for the television industry,¹ did not provide a quantitative alternative. The development of the photomultiplier² was an important milestone.

The photomultiplier had sensitivity to single photoevents and the capability for high time resolution. Although the photomultiplier was approximately 2 orders of magnitude more sensitive than the photographic emulsions, in a spectrograph it was limited to monochromatic samples. New optical designs were optimized for photomultipliers. By the early 1960's emphasis had shifted to monochromators (spectrometers), but the photographic spectrograph was still quite competitive when large spectral ranges and spatial resolution were required. Photometers with interference filters were useful as high-throughput monitors of a particular wavelength.

The most recent detector development has been in the family of solid-state arrays, including CCD's, charge-injection devices, Reticon photodiode arrays, and others.^{3,4} Although these devices have been available for approximately two decades, their application has been slow even though they have represented a major advancement in capability. We have been using the ICCD in our observational programs. ICCD's can be compared with the detectors mentioned above by noting that the ICCD's have the same sensitivity to photons as do photomultipliers as well as the advantage of spatial resolution. With the ICCD instead of the photographic plate in a spectrograph, the spectrograph has single photoelectron counting capability, an improvement of approximately 2 orders of magnitude in sensitivity over the photographic plate. However, the full potential of this improvement cannot be realized by simply substituting the ICCD for the photographic plate; rather, the optics must be redesigned and adapted to the requirements of the new detector.

In this sense, the development of detector systems and scientifically useful applications are two different concepts. Several good review papers expound the details of the detectors that are under development.^{3,5,6} These descriptions do not deal with many of the practical aspects of application except in a futuristic way. Application, as discussed in this paper, means the use of available technology to make scientifically useful measurements. The distinction between application and development is important in the following discussions because the promises of detector development in the past 10 years are familiar, whereas

The authors are with the Lunar and Planetary Laboratory, University of Arizona, Tucson, Arizona 85721.

Received 8 April 1991.

0003-6935/92/163097-12\$05.00/0.

© 1992 Optical Society of America.

The U.S. Government is authorized to reproduce and sell this report. Permission for further reproduction by others must be obtained from the copyright owner.

practical applications are specialized. Few detectors qualify as candidates for use in general-purpose instrumentation.

The astronomy community has taken a leading role in the application of CCD's to scientific measurement over the past 15 years. The capabilities and shortcomings of the CCD are well understood. In the use of intensified array detectors, astronomers again tried several techniques but improvements in the bare CCD progressed quickly enough to satisfy their requirements. The Voyager UV spectrograph launched in 1977 used an intensified linear array.⁷ It has undoubtedly the largest database from which to study the application of array detectors that can record single photoevents.

The development research and application of CCD's over the past decade have resulted in understanding and confidence in the device. This is a result of both industrial and scientific interest in the CCD. Another device, the proximity focused image intensifier, that uses microchannel plates and a phosphor screen on a fiber-optic output faceplate, has become readily available and can replace the photomultiplier in many cases. This is also a proven product resulting from military interest. Other detectors under development with various readout techniques do not fit into the category of proven and available. They fit into a class of special application and in our opinion cannot be viewed as competing devices for general use in airglow and auroral measurements.

The ICCD is formed by fiber optically coupling the output of the proximity focused image intensifier to the CCD to take advantage of the best attributes of both devices. The task is then a matter of engineering and verification rather than of detector development. Here we discuss the use of ICCD's in two types of instrument that are suited for measurements of extended sources, such as airglow and aurora, namely, spectrographs and imagers, with major emphasis on the former. We compare their performances with alternative detectors and discuss factors that must be considered in optimizing an observing program based on them. Among these are noise characteristics and suitable optical designs. In contrast to the development of specialized sensors needed for some particular applications, we emphasize the idea of using standard CCD's and image intensifiers available in standard product lines. We find that these are suitable for a large class of measurement that is of interest for studies of aurora and airglow.

II. General Considerations in the Application of CCD's and ICCD's

The bare (unintensified) CCD has been used extensively in astronomy. The attributes of the device that have been the most important are the linear response over several decades of dynamic range and the ability to integrate for long periods of time, hours at liquid nitrogen temperatures. The first is important because the data are in a digital format easily manipulated by computers. The second allowed the inte-

grated signal from weak sources to exceed the threshold of sensitivity. The threshold was fairly high in the early days. The Voyager UV spectrograph detector⁷ had a read noise of 10^4 electrons chosen as an easily attainable design criterion, although a level 10 times better could be reached with special effort. Modern CCD systems exhibit read noise in the several-electron range, approaching the ideal detector. However, they have other problems consistent with high-sensitivity systems.

The intensified CCD has all the attributes of photoelectron counting that are offered by the photomultiplier, including access to the whole photoelectric spectral range from 20 to 1200 nm but has been slow to be accepted as a viable detector system. We proposed the fiber-optic coupling of a proximity focused imaged intensifier to a Reticon photodiode array for the Voyager spectrograph in 1971 following the research of Riegler and More.⁸ The first ambitious application of the ICCD⁹ was initiated in 1976 by these authors in the Imaging Spectrometric Observatory (ISO) proposed for Spacelab I.¹⁰ Except for advancements in electronics, little has changed in our understanding of the ICCD as a detector system. It is not ideal, but it is readily available, has been used in several flight instruments, including the UV imagers aboard the Viking Earth Satellite,^{11,12} and is flexible in configuration.

The CCD and the ICCD differ considerably in use. A primary consideration in selecting between them is their thresholds of detection for a given integration time. For simplicity, we assume in the following discussion that the CCD and the ICCD have identical quantum efficiencies, thereby generating photoelectron events at equal rates. The CCD is basically an analog detector, but its sensitivity is high enough that it is evaluated by single-photon (electron) statistics. The read noise is typically 10–50 e⁻ (electron-hole pairs) rms, and, in special cases, it has been reported to be < 10 e⁻ rms. The signal-to-noise ratio (S/N) ρ for a read of a single pixel may be written as

$$\rho = \frac{S}{\sqrt{N + D + S}} \quad (1)$$

where S is the number of electron-hole pairs generated by the signal, D is the number resulting from thermal dark rate, and N represents the contribution from the read noise of the electronics. We take N to be the square of the rms read noise. Figure 1 shows the curves of ρ for a range of values of S .

The intrinsic dark count rate of the photon counting ICCD is very small on a per-pixel basis. For example, the dark count rate of a cooled S-20 photocathode of diameter 25 mm is typically 10 events/s. Scaled to the 5×10^{-4} mm² area of the pixel, this corresponds to $\sim 10^{-5}$ events pixel⁻¹ s⁻¹. Cathodes with reduced red response (higher work function) are less noisy. The ICCD curve, in the interesting range of the CCD curve, is a straight line. In Fig. 1, the ICCD curve was drawn through a S/N of 10 and

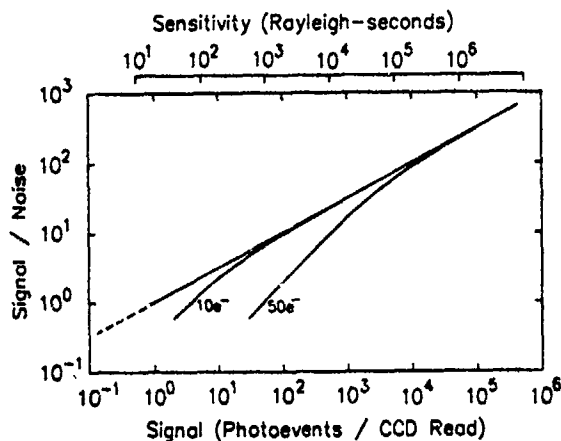


Fig 1. Signal-to-noise ratio ρ for CCD and ICCD detectors computed by using Eq. (1). The straight line represents the ICCD for which N is effectively zero because of the photoelectron counting capability of the ICCD. The curves represent CCD systems having readout noise of 10 and 50 electrons.

100 then extrapolated through 1 without regard for the statistical implications since individual photoevents can be detected by the ICCD.

It is interesting to consider the meaning of the threshold of detection for each detector system. The photoevent counting intensifiers are the most straightforward. The noise is dominated by the shot noise in the signal. Long integrations give the same results as the summation of multiple short samples representing the same total integration time. On the other hand, the read noise and the other effects in the operation of the CCD limit the threshold sensitivity. With the CCD, the most effective way to increase ρ is to increase the integration time—astronomers use hours. If adjustment of the integration time is not acceptable, two other approaches can improve the statistical performance modestly. They are referred to as on-chip summation and off-chip summation.

For photon counting detectors, both techniques (on-chip and off-chip summation) result in improved statistics. The photoevents appear as a burst of up to $10^3 e^-$ in the CCD. This charge overwhelms the lower level of noise associated with normal CCD readout. Event counting statistics will prevail (Fig. 1). This is not the case for the bare CCD.

On-chip summation sacrifices spatial resolution to minimize the number of read operations required to measure the charge on the chip. The technique is to move the charge in several adjacent pixels into the output junction, then sample and digitize the accumulated charge with a single read. Although this improves the signal-to-noise ratio over the sensitive area, the question of interest here is the effect on the threshold of detection. For example, if 10 pixels, each having a signal charge of $50 e^-$, are summed on chip, the resulting signal-to-noise ratio should be 10. If each pixel had an average of only $5 e^-$ and was shifted into the output junction, would the result be a signal-to-noise ratio of unity? There is the question of efficiency in handling a 5-electron charge. We do not

know of research that deals specifically with the effect of moving small numbers of charges. In any case, there are other noise contributions that become significant at this level of on-chip summation.¹³ Any leakage charge on the pixels would be summed into the output gate as well as the signal charge. It appears that there would be difficulties in pushing the threshold down far with the on-chip summation technique.

Off-chip summation also has limitations when the signal is close to threshold. First, the S/N improvement follows the square-root law in this case. Although areas that have identifiable intensity structure will improve in S/N, it is unlikely that the summation of samples with a S/N of unity or less will result in a recognizable improvement in the threshold of detection. The effect of reducing the read noise to $10 e^-$ is shown in Fig. 1, but the considerations above are still valid in evaluating the threshold of detection at the $10 e^-$ level.

We argue that the two devices, the CCD and the ICCD, can be separated in their application by their threshold of detection. For continued discussion we assume that the CCD has a threshold of detection of approximately 50 photoevents for comparative purposes. Also, we assume that each pixel of an ICCD can be considered as a photon counting device that preserves the Poisson statistics of the arriving photons.

The dynamic range of the detector is generally not a limitation for either CCD approach. The limitation in dynamic range in many cases is caused by internal scattering in the optical system and not the detector. The bare CCD has a linear response from its threshold to pixel saturation. Depending on the threshold and the full-well charge capacity of the pixel, the dynamic range can be greater than 10^4 . Saturation of some pixels does not affect the rest of the pixels significantly. This dynamic range is sufficient for most applications, and it can be extended by exposure control.

The ICCD dynamic range is not restricted by the detector either. It is defined by a companion digital memory and the dark count rate rather than by the full-well capacity. At maximum gain, the intensifier generates approximately $500 e^-$ /photoevent in a CCD pixel. This implies a dynamic range of 500 events for a full-well capacity of $2.5 \times 10^5 e^-$, but the CCD can be read out often and the events accumulated in a companion memory. High signal levels can also be handled by reducing the gain of the intensifier. The good statistical accuracy implied by the high photoevent rate is maintained by integrating the signal on the CCD; the only statistical penalty is a factor of $2^{1/2}$ introduced in the transition from pulse counting to pulse integration. The Voyager UV detector can integrate the signal on the anode array when the microchannel plate MCP is operated at low gain. The result is a markedly extended dynamic range. When the Voyager UV spectrograph observes the sun, it measures photoevent rates up to 3×10^5 photoevents/s/pixel. At full gain, photoevent rates of 5×10^3 s/pixel are routinely recorded at our thresh-

old of detection. The full dynamic range is therefore approximately 10^7 . The threshold of detection for the Voyager UV spectrograph detector is similar to that of the ICCD detector system, 10^{-3} events/s. This threshold is higher for the photocathodes that generate appreciable dark noise.

The ability to deal with high signal rates is not usually the concern in typical scientific applications. Rather, the limiting factor is usually the ability to deal with weak signals. Scientific observations are most often driven to the statistical limit to improve temporal, spatial, or spectral resolution.

For many investigations, the possibility of choosing the photocathode of the ICCD to reject unwanted long-wavelength emissions gives it an important advantage over the bare CCD. For example, many diagnostic emissions fall in the far UV. With a bare CCD, scattering from near UV and visible wavelengths, where the solar flux is orders of magnitude higher than in the far UV, can compromise measurements of the features of interest. A solar-blind photocathode in an ICCD is a convenient solution. We do not treat this advantage quantitatively because it depends on the specific application, but it is potentially a crucial point.

III. Application of Array Detectors to the Spectrograph

In the following discussions we concentrate on the use of the ICCD for aeronomical measurements, comparing it with other detectors that have been used for that purpose. We also consider the bare CCD, but the need for short integration times in most aeronomical observations leaves the bare CCD a poor contender.

There are five important differences between the ICCD spectrograph and the photomultiplier monochromator that we discuss in the following sections: (1) optical design criteria are different; (2) optical throughput or speed of the spectrograph for obtaining a complete spectrum is improved by approximately 2 orders of magnitude because of the multiplexing nature of the detector; (3) instrument size can be decreased by a factor of 10 in focal length or 10^3 in volume in many applications; (4) effective dark count rate per pixel is reduced by at least 2 orders of magnitude; and (5) quality of the data is improved remarkably because the spectrograph need have no moving parts. The specific application will determine the degree to which these improvements can be achieved, but, in general, the advantages are almost revolutionary.

A. Optical Designs and the ICCD Detector System

In Section I, we noted that the development of the photomultiplier resulted in a change in the optical design of spectrographic instruments to take advantage of the photomultiplier. The array detector also requires special optical designs. There will be a return to the spectrographic configuration but with some new constraints.

Spatial and spectral information can be obtained from the spectrograph, but this requires a good

quality image of the entrance slit in the image plane of the camera system. (Typically, there are three imaging optical elements defining a spectrograph: the collimator, the dispersing element, and the camera.) The optics for a monochromator need image only the width of the entrance slit on the exit slit for good performance; a one-dimensional or astigmatic image will suffice. Fastie¹⁴ was quick to rediscover the Ebert monochromator, which had not seen much use since its original description,¹⁵ presumably because the severe astigmatism in the system was unsatisfactory for a spectrograph. Fastie pointed out that a similar optical system could cancel spherical aberration and greatly reduce coma by the use of complementary spherical surfaces for the collimator and camera optics and of a special curved slit geometry. The reflecting optics have no chromatic aberration. The result was a high-throughput high-resolution monochromator, the Ebert-Fastie (E-F). However, the curved slit and astigmatic optics are inappropriate for the rectangular format of the CCD. Although the E-F optical system is fast, recording the full spectrum in a single exposure on the ICCD has an advantage of approximately 2 orders of magnitude over the E-F monochromator. This is best illustrated by a direct comparison of the E-F monochromator and a comparable ICCD spectrograph.

The performance of a monochromator or spectrograph viewing an extended source can be estimated by using the photometric equation

$$P = B A_d \frac{A_g \cos \phi}{F^2} \tau \eta \epsilon, \quad (2)$$

where P is the photoevent rate in events $s^{-1} \text{ pixel}^{-1}$, B_s is the brightness of the source in photons $s^{-1} \text{ cm}^{-2} \text{ s}^{-1}$, A_d is the area of the detector, $A_g \cos \phi$ is the effective area of the grating of area A_g operating at an angle ϕ , F is the focal length of the camera lens, τ is the optical transmission, η is the efficiency of the dispersing element, and ϵ is the quantum efficiency of the detector.

The following discussions can be simplified by some substitutions into Eq. (2). The area of the detector can be replaced by the effective dimension of the exit slit, L , the length of the slit, and, W , the width. The grating area divided by the focal length squared is a solid angle and can be replaced by the reciprocal f -ratio of the camera optics squared,

$$\frac{A_g \cos \phi}{F^2} = \frac{\pi}{4 f^2}$$

The modified photometric equation is

$$P = B_s \frac{\pi L W}{4 f^2} \tau \eta \epsilon. \quad (3)$$

For this comparative study, we assume that the transmission of the optical system τ , the grating or dispersive efficiency η , and the quantum efficiency ϵ are equal in the two systems. When the constant

terms are collected into the constant k , the expression becomes

$$P = k \frac{LW}{f^2} \quad (4)$$

and from system to system the throughput E has the proportionality

$$E \propto \frac{LW}{f^2} \quad (5)$$

This can be made more specific by comparing the performance of an E-F 0.125-m monochromator with that of a spectrograph having equivalent resolution, spectral range, and f -ratio but designed around the ICCD. The two optical systems are shown in Fig. 2. Table I lists the characteristics of the two designs.

The two sets of design parameters have been selected to produce identical spectra. The focal length and f -ratio were taken from the E-F design. A high-dispersion grating maximizes the throughput of the monochromator and three grating steps per slit width were used. To match this the ICCD system has 3 pixels per slit width and a grating ruling selected for a dispersion of 3.3 Å/pixel. The spectral range was determined by the number of rows in the ICCD array so that each spectrum would contain 576 samples.

Because the f -ratios are equal in the two instruments, their monochromatic throughput is simply

Table I. Monochromator-Spectrograph Comparison

Parameter	Ebert-Fastie Monochromator	Array Detector (ICCD) Spectrograph
Focal length (F)	125 mm	125 mm
f -ratio (f)	5	5
Resolution	10 Å	10 Å
Grating	3600 lines/mm	530 lines/mm
Slit width (W)	0.45 mm	0.066 mm
Slit length (L)	12 mm	8.5 mm
Spectral element Range	3.3 Å/step	3.3 Å/pixel
Elements per spectrum	576	576
Optical throughput (E) (monochromatic)	9.6	1
Optical throughput for full spectrum	1	60

The spectrograph has no physical exit slit, but the function of an exit slit is performed by the discrete pixels of the ICCD.

the ratio of the areas of their slits. The E-F slit is 9.6 times larger than the slit in the ICCD spectrograph. However, to cover a range of 1900 Å at the specified resolution, we must step the E-F grating and integrate 576 times. Hence we must consider the rate at which information is recorded, and we find that the spectrograph will produce 60 spectra, in the same time the E-F monochromator produces a single spectrum of comparable quality. Not only does the spectrograph gather photons 60 times faster than the monochromator, but the quality of the data is improved. Scattered light in the spectrograph is lower by the ratio of the areas of the slits, a factor of 9.6. The detector and the optical system of the spectrograph have no moving parts, so internal scattering depends only on the input illumination and can be measured for later removal. In the spectrograph, the wavelength scale is fixed by the unchanging relationship of the optics and the detector. In contrast, a reliable wavelength scale in a spectrometer with a rotating grating depends on the precision of the mechanism that positions the grating. Temporal variations in the source are recorded over the entire spectrum simultaneously by the spectrograph. The spectrograph images the entrance slit on the detector, so that the spatial variations in the source will be recorded. All the advantages of spectrographs with photographic plates can be realized in the ICCD spectrograph.

Flexibility and small size are additional advantages of the ICCD spectrograph. The optical design of the E-F system is fixed, and the experimenter can use only the fore optics to adapt the instrument to the observation. This is not the case with the ICCD spectrograph. The entire optical train is at the designer's disposal. It is most important to realize that the optical design of an ICCD system is constrained by the size of the detector, and, therefore, high speed does not necessarily imply a large instrument. The quantities L and W are the dimensions of the pixel array on which the entrance slit will be imaged and are therefore constrained by the detector size. The

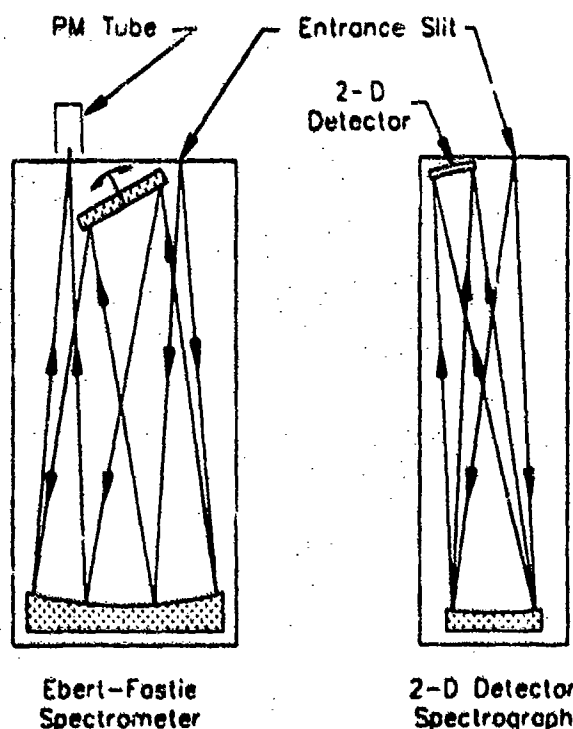


Fig. 2. Comparison of a conventional E-F spectrometer with a spectrograph designed to take advantage of modern two-dimensional detectors. In terms of the time required to cover the same range of wavelengths at equivalent resolution and statistical accuracy, the spectrograph has an advantage of a factor of 60.

f -ratio refers to the camera feeding the detector. The throughput will be constant as long as the f -ratio remains the same regardless of the size of the optics. In practice, the size of the optics can be reduced until the image quality over the area of the detector becomes unacceptable because of the optical aberrations in the system. It is also noteworthy that the throughput is not affected by the speed of the optical system in front of the grating provided it does not vignette the camera system. The f -ratio of the collimator can be large compared with that of the camera. A large f -ratio has the advantage of better scattered light control in the spectrograph. The f -ratio can be reduced until the image quality at the edge of the array becomes unacceptable.

The example above can be extended to instruments used in the past. A variety of instruments that have seen substantial use over the last two decades are cited to illustrate the use of array detectors. Beginning with the basic instrument design, we adjusted the parameters of each instrument to give the same spectral resolution in the 400-nm region of the spectrum. Then we evaluated the constant in Eq. (4) for each instrument to place the comparison on a common photometric scale. The characteristics of the instruments are gathered in Table II. The slit widths of the monochromators were chosen for 3-Å spectral resolution, assuming the use of a 1200-line/mm grating in the second or the third order as indicated. The spectrographs have their resolutions set by the pixel size and the slit width; the slit width in the

image plane was taken to be 3 pixels. In this case, the ruling of the grating would be adjusted to give the correct linear dispersion; note that only this apparent slit width enters the calculation of sensitivity. Spectrograph E (see Table II), an objective grating spectrograph similar to the Voyager UV instrument, can be included in the comparison because the calculation is independent of wavelength. At EUV wavelengths reflective efficiencies are poor, requiring a trade-off between resolution and throughput. Spectrograph F refers to an ICCD spectrograph that we recently put into service. Called the Arizona Imager/Spectrograph (AIS), it was built for the U.S. Air Force Geophysics Laboratory and will be flown on the space shuttle Discovery. Details of the instrument are given in a companion paper.¹⁶ A compromise in throughput by a factor of 4 was accepted to permit the spectral range 115–900 nm to be recorded simultaneously with 4600 spectral elements. The slit width is 2 pixels. Spectrograph G is the same as spectrograph F but designed to have full throughput with a slit width of 3 pixels as in the comparison with the E–F spectrometer above.

Spectrograph H is a special case. It is the same as spectrograph F except that it has a bare CCD rather than an ICCD in the image plane. The read noise of the CCD is a limiting factor as noted above. Even though there are nearly 1800 pixels within the effective slit, there is a read noise of $50 e^-$ associated with the reading of each pixel. The sum of all samples would give an effective read noise of $50 \times \sqrt{1800} =$

Table II. Spectral Instrument Comparison

Parameter	A E–F, 0.125-m Mono- chromator ^a	B Jarrel-Ash E–F, 1 m ^b	C Fast E–F, 1 m ^b	D ISO/ Spacelab 1	E Voyager UV Spectro- graph ^c	F AIS ICCD Spectro- graph ^d	G ICCD Spectro- graph ^e	H AIS CCD Spectro- graph ^f	I Photographic Spectrograph ^g
Focal length, F (cm)	12.5	100	100	50	20	27.5	27.5	27.5	—
f -ratio, f	5	8.8	8.2	3.6	3.6	4.1	2.9	2.9	0.8
Slit width (cm)	0.010	0.077	0.14	0.011	0.030	0.005	0.006	0.004	—
Slit length (cm)	1.2	5.1	15.2	0.57	0.30	0.45	0.40	0.80	—
Transmission, τ	0.78	0.78	0.56	0.82	0.60	0.90	0.90	0.90	—
Dispersion efficiency, η (order)	0.60 (2)	0.50 (2)	0.40 (3)	0.50	0.70	0.35	0.35	0.35	—
Quantum efficiency, ϵ	0.12	0.12	0.12	0.12	0.12	0.12	0.12	0.30	—
Spectral elements	1	1	1	190	128	4600	576	576	500
Photocount rate, $P/\Delta t$ (R ⁻¹)	1.68	14.8	93	1.50	2.19	0.22	1.3	2.25	—
Detector noise, s^-	10	10	10	3.1×10^3	4.5×10^3	2.8×10^3	2.8×10^3	0.05	—
Sensitivity, Rayleigh s^- (R ⁻¹)	2.2	0.25	0.040	0.67	0.46	4.55	0.76	222	10^4

^aResolution of 3 Å in the vicinity of 4000 Å.

^bCalculated in this paper.

^cRef. 18.

^d150-mm curved slits, designed by Fastie, Ref. 14.

^eRef. 10.

^fRef. 19.

^gRef. 16.

^hSame as spectrograph F but optimized for test specifications.

ⁱRef. 16.

^jRef. 17.

^kThe emission rate required to give a S/N of unity in 1 s.

2000 e^- , requiring a signal of 2000 e^- , to provide $S/N = 1$. On-chip summation of 18 pixels per read followed by off-chip summation would result in an effective noise threshold of 500 e^- , the number used in Table II.

The comparative study is completed by estimates for a photographic spectrograph, I. Vallance-Jones¹⁷ comments on high-speed photographic spectrographs. For an instrument developed by A. B. Meinel in the early 1950's and used with an $f/0.8$ Schmidt camera, he suggested a sensitivity in the 10^5 -R s range as a reasonable working value and estimated the threshold of sensitivity to be 10^4 R s.

The sensitivities in Rayleigh seconds from Table II are plotted in Fig. 3. The Rayleigh second¹⁷ is the emission rate required to produce a S/N of unity in 1 s. The calculations whose results are shown in Table II treat each instrument as a monochromator having one spectral element. As the spectral ranges for monochromators A, B, and C increase, the sensitivities decrease proportionally because time must be shared among the other elements of the spectrum. On the other hand, the spectrographic instruments have roughly the same sensitivity at each spectral resolution element.

There are many techniques for optimizing an instrument for a specific observation. Because the requirement in future programs is for broad spectral coverage, it seems that the ICCD system will be most useful. The airglow atlas of Broadfoot and Kendall¹⁸ was accumulated in segments of 500 spectral elements with monochromator B. Figure 3 shows that an equivalent spectrum of 576 spectral elements would be recorded by an optimized ICCD spectrograph (G) approximately 200 times faster than with

monochromator B. The AIS (spectrograph F) will record the same spectrum of 500 elements 32 times faster but in addition will record a much wider spectral range, including 4600 spectral elements at once. This is a spectacular improvement in capability. The rating of the CCD spectrograph, H, with respect to optimized ICCD spectrograph G is noteworthy. ICCD spectrograph G seems to be 316 times faster than spectrograph H on the basis of this comparison. It can be argued that we have not treated the CCD spectrograph fairly. In particular, we assumed equal quantum efficiencies for the CCD and the ICCD, whereas the detective quantum efficiency of the CCD was higher for certain wavelengths. However, even factors of 3-5 do not bring the CCD spectrograph into contention. It was demonstrated that the improvements discussed above are attainable in practice, but this is not discussed in detail here.

B. Size of ICCD Spectrographs

In the discussion of the optical designs and the ICCD spectrograph it was mentioned that the design is constrained by the size of the ICCD format. This conclusion follows directly from relation (5). The proper length and width for the slit image are determined by the CCD format and are therefore constant, leaving only the dimensionless f -ratio as an adjustable parameter. The comparative study in Subsection III.A addressed the performance of several instruments whose focal lengths ranged over an order of magnitude from 100 to 10 cm. The monochromator performance scales by focal length, whereas the performance of the spectrographs scales by array size. Note also that the performance was improved by orders of magnitude in the short focal length instruments that can record broad wavelength regions.

A difference of a factor of 10 in focal length implies a difference of a factor of 1000 in instrument volume. For example, a standard commercial 35-mm camera lens, such as the Nikon 135-mm $f/2$ with a 50-mm square grating and a modest collimator and slit, forms a small spectrograph. The smaller f -ratio would improve its performance by a factor of 2 over ICCD spectrograph G in Table II. Although it would be limited in spectral range by the lens coating, the comparison in size and performance is remarkable.

The application of new technology has completely reversed the emphasis on instrumentation. The monochromator is a precision, high-cost optical tool with a readout system as simple as a photomultiplier tube and a strip chart. The array detector permits the use of simple optical configurations, but the data retrieval and the manipulation require major resources. However, once the data analysis system has been established, the spectral coverage required in future programs can be achieved by a replication of small spectrographs covering the spectral range and having a common data format. At the University of Arizona, this technique is used to provide small space flight spectrographs in a group of five to cover the wavelength range from 115 to 1100 nm simultaneously

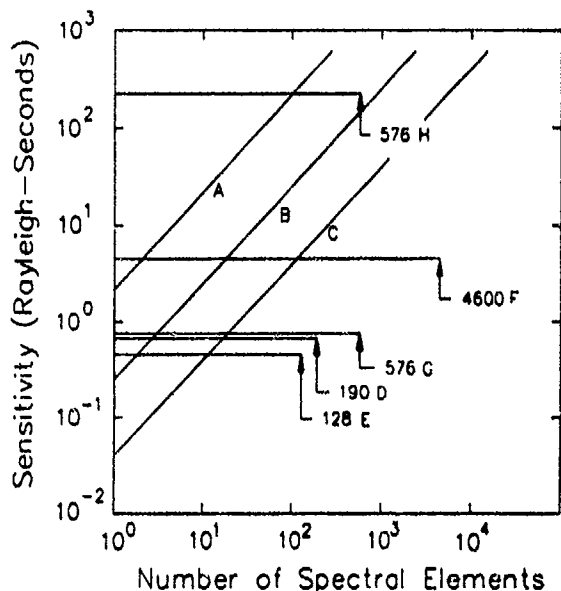


Fig 3. Sensitivities for the instruments listed in Table II. The letters that label the lines correspond to those in the table. The numbers show the number of spectral elements in each spectrum. The sensitivities of the monochromators depend on the number of spectral elements because of the necessity for time sharing.

with 4600 spectral elements. The spectral resolution varies from 3 to 10 Å over the spectral range. The spectrograph set has outside dimensions of 41 cm × 41 cm × 21 cm. This instrument is described in a companion paper.¹⁶ The spectrographs are included in Table II and Fig. 3 as spectrograph F.

C. Data Quality Comparisons

Not only does the ICCD spectrograph have a photometric advantage over monochromators, the quality of the data shows a remarkable improvement as well. The data set accumulated by the Voyager UV spectrograph¹⁹ can illustrate this point. Because the detector integrates signals continuously over the whole spectral range, it records temporal variations in the relative brightness of features within the passband properly. Also, the effects of internal scattering and other characteristic contaminations are recorded simultaneously with the primary emissions.

The monochromator lacks this advantage because only one wavelength position is sampled at one time. The recorded signal includes not only the selected wavelength but also a scattered contribution from other bright regions of the spectrum. The scattered component cannot be determined with confidence because the emission causing it is not recorded simultaneously.

The Voyager UV spectrograph presents a unique opportunity to evaluate a photoevent counting spectrograph. It has no moving parts. It records the spectrum from 500 to 1700 Å in 128 segments with an intensified Reticon linear anode array. Although this spectral range may be unfamiliar to many researchers, the data are characteristic of the photoevent counting spectrographic capability at any wavelength.

Figure 4 shows a Voyager UV spectrograph spectrum²⁰ of emissions from the interstellar medium acquired in the direction of the galactic pole, a region free of stars. The integration time was 1.5×10^6 s, or approximately 415 h. The emissions arise from resonance scattering of solar lines by interplanetary hydrogen and helium. The He (584-Å), H (1216-Å), and H (1025-Å) lines are well defined. Note that the ordinate scale changes through the analysis. The H (1216-Å) line intensity results in a peak photoevent rate of approximately $1 \text{ s}^{-1} \text{ pixel}^{-1}$. Laboratory calibration of the instrument measured the scattering from lines at many wavelengths throughout the wavelength range. After the detector dark count is subtracted, a matrix multiplication removes the effects of scattering of the four emission lines He (584 Å), H Ly- α , H Ly- β , and H Ly- γ . The resulting spectrum is shown in Fig. 4b. In Fig. 4c, this reduced spectrum is compared with a model computed by a spectral synthesis program that applies the instrument's transmission function to the four discrete lines. Using these techniques, we have found that the modeling process gives a sensitive measure of wavelength. Although each spectral element is approximately 9 Å wide, the model line must be placed within 2 Å of the

true wavelength position for a match to be convincing. Figure 4d shows the difference between the model and the reduced spectrum in Fig. 4c. This represents the noise in the observation after the emission is removed. Differences are large where the signals are larger even though the percentage error is decreasing. In Fig. 4a, the count at approximately 750 Å is approximately 4.5×10^4 counts channel^{-1} in 1.5×10^6 s. Poisson statistics imply a corresponding standard deviation of 212 events or ± 0.14 events in 1000 s. That envelope, illustrated in Fig. 4d, is close to the envelope of the noise left after the analysis. This demonstrates that it is possible to understand the origin of all events in the spectrum, to the statistical limit of the observation. Finally, the event rate for the peak in the H Ly- α line was 1 s, whereas the rate for the H Ly- γ line peak was 1 in 330 s; the usable dynamic range for these spectra was therefore at least 330. Similar research can be done with photoevent counting systems having higher sensitivities and higher counting rates limited only by the statistical accuracy of the weakest emission as noted above.

IV. Application of Array Detectors to Imaging

The astronomy community took the lead in the application of the CCD to research imaging. Again, this was an expensive undertaking requiring the development of new electronics techniques, the evaluation of sensors, and the development of image processing systems. In this application, the CCD competed with the photographic plate, which it easily bested. Even the early CCD devices and systems exhibited important advantages in detector capability. Although this technology was an important advancement holding great promise in astronomy, long integration times and broad spectral bands were acceptable. In contrast, the airglow and auroral community requires higher time resolution and narrow-band photometry, and the bare CCD has proven less useful. The interference filter and the photomultiplier had replaced photography as a scientific tool in the early 1960's. Monochromatic imaging was pursued by using flying spot photometers. Intensified photography has seen modest use in the last few years, followed by some use of intensified solid-state detectors.

The requirements of the astronomical application and the airglow and auroral application differ. For the purpose of this discussion it is appropriate to compare on the basis of angular resolution. When an $f/3$ telescope with an aperture of 4 m and a focal length of 12 m illuminates a single CCD pixel, 0.022-mm square, the pixel has an angular field of view of 0.4 arcsec. If the field of view is filled by a radiating nebular gas as well as the airglow in the foreground, the signals will be proportional to the surface brightnesses. The surface brightness of the nebular gas may change from pixel to pixel with changes in gas density or excitation. The airglow brightness would contribute to each pixel uniformly because the field of view is

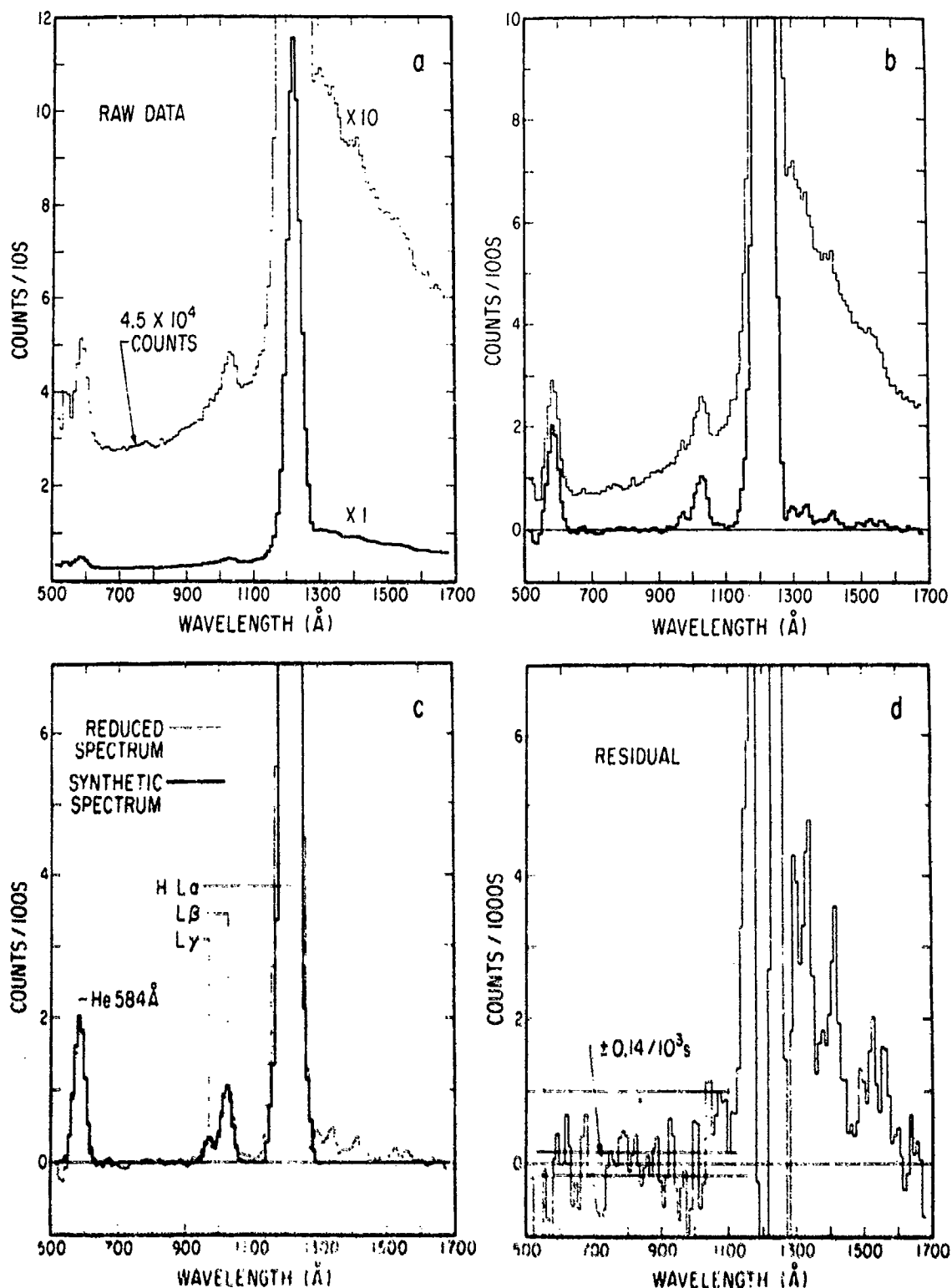


Fig. 4 Illustration of the steps leading to a final spectrum from a spectrograph. ^a a. Raw spectra including signal and detector background. The detector background is due to intrinsic noise and to gamma rays from the radioisotope thermoelectric generators that power the spacecraft. ^b b. Result of subtracting the detector background (top curve) and removing the instrumental scattering (bottom curve). ^c c. Comparison of the lower curve in ^b with a synthetic spectrum composed of He 584 Å and H Lyman series lines. ^d d. Residual after subtracting the data and the synthetic spectra in ^c.

small compared with the scale of variations in airglow emissions. When the optical system is scaled down by a factor of 10^3 to an aperture of 4 mm and a focal length of 12 mm, the same pixel has an angular field of 0.1° . The nebular source would be contained in a small fraction of the field of view with the detected radiation reduced proportionally. However, the airglow still fills the field of view of the pixel, and the signal level will be the same as for the larger system because the photometric expression [relation (5)] is the same for both optical systems. The brightness of the airglow might vary from pixel to pixel depending on the source of the emission.

We make these comparisons for two reasons. The first is to emphasize that the significant feature of an image is the variation of intensity over the field. It is important to select the angular field to match the scale of the intensity variation to be measured. The second is to emphasize that the photometry is independent of the size of the optical system.

The discussion of the threshold of detection of the ICCD and the CCD can be placed on an absolute scale for this imaging review. If an optical system has the following parameters, f -ratio, 1; pixel area ($2.2 \times 10^{-3} \text{ cm}^2$); transmission (τ), 0.9; quantum efficiency (ϵ), 0.2, then for the unit emission rate, $1 \text{ R} = 10^6/4\pi \text{ photons s}^{-1} \text{ cm}^{-2} \text{ sr}^{-1}$, in Eq. (2) the photoevent rate is $5.4 \times 10^{-2} \text{ events pixel}^{-1} \text{ s}^{-1}$. The abscissa of Fig. 1 can be converted to the sensitivity scale at the top of the figure by using this factor. For instance, an emission rate of 18.5 kR would generate 10^3 photoevents $\text{pixel}^{-1} \text{ s}^{-1}$. The threshold arguments made previously can now be considered on an absolute scale. The sensitivity of the CCD imager would be $\sim 1 \text{ kR s}$. A surface brightness of 1 kR would produce $50 \text{ e}^- \text{ pixel}^{-1}$ in a 1-s exposure, the previously defined threshold of detection. For the ICCD the corresponding number would be 18 R s.

A. Broad Spectral Band Imagers

Many of the dominant auroral emissions can be monitored with interference filters of reasonably wide bandpass (e.g., 50 Å) that could be incorporated into the fast $f/1$ optical system used as a baseline in the discussion above. Even with the 1-kR s threshold of the bare CCD, typical auroral emissions, which are usually tens of kilo-Rayleighs, would give detectable signals in a 1-s exposure. The 0.1° angular resolution of a single pixel corresponds to a scale of 200–400 m at typical auroral heights and ranges. An array of 100×100 pixels corresponds to a field of view 10° square, a size useful for comparative studies of auroral morphology. This type of imager would also be useful for support imaging during spectrographic observations. Clusters of four or six miniature imagers are quite feasible with fiber-optic technology and CCD arrays. For weaker aurora where requirements for both time and spatial resolution can be relaxed, both longer exposures and on-chip summation of four or nine pixels would produce images of good S/N ratio. Intensified systems would be required for better time

resolution, but these can also be implemented in a clustered set.

The imagers associated with the spectrographs in the companion paper¹⁶ were prepared following the outline above. Twelve miniature images are recorded by two CCD's with fiber-optic coupling; 10 of these are intensified.

B. Monochromatic Imagers

For narrow-band monochromatic imaging, the need for near-normal incidence on the interference filter constrains the f -ratio of the optical system. In this case, maximized throughput is important because these imagers are often used to separate weak emissions from a complicated spectral region. The optical technique is to use the largest interference filter available. An image of the sky is formed on the filter through telecentric optics. This image is then re-imaged on the intensifier. To maintain the passband of an interference filter with a 5-Å bandwidth, the incidence angle θ must not exceed approximately 4° from the normal. The required f -ratio of the fore optics is given by $f = (2 \tan \theta)^{-1}$, which implies an $f/7$ system for the example given here. If the optics are properly designed, the f -ratio of the fore optics can be converted to an $f/1$ system feeding the CCD. This will result in a system with the sensitivity defined by the ICCD curve in Fig. 1 if the f -ratio transition is made without vignetting. (Some corrections are required for optical transmission and quantum efficiency). A sensitivity near 40 R s would be typical. Again, by sacrifice of spatial resolution through on- or off-chip summation of 2×2 or 3×3 pixels, the signal could be increased by factors of 4 and 9, respectively; this is effectively increasing the area of the pixel.

Still higher sensitivities can be achieved by a further increase in the effective area of the detector. This can be achieved with the ICCD by use of larger proximity focused intensifiers, say 40-mm diameter, with the output image reduced by a fiber-optic taper to 15-mm diameter to fit the CCD array.

C. Application to the Fabry-Perot Interferometer

The Fabry-Perot (F-P) interferometer falls in the same category as the monochromatic imager, but its field of view is still narrower, and large plates are used to increase the collection area. The optical coupling problem is the same as that for the monochromatic imager; a high-speed telescope would be used with an aperture the size of the F-P plates. The focal length of the telescope would determine the number of rings falling on the CCD. Each spectral order in the F-P fringe pattern contains the same energy. The improvement over the classical scanning F-P system can be evaluated by counting the number of rings and the number of elements required across the ring. An operational advantage lies in the ability to find the center of the ring pattern with software rather than by adjusting the plates and the ring position.

We commented above on imaging the aurora through passband filters with a CCD. In this section we discuss the threshold of detection and the ICCD in

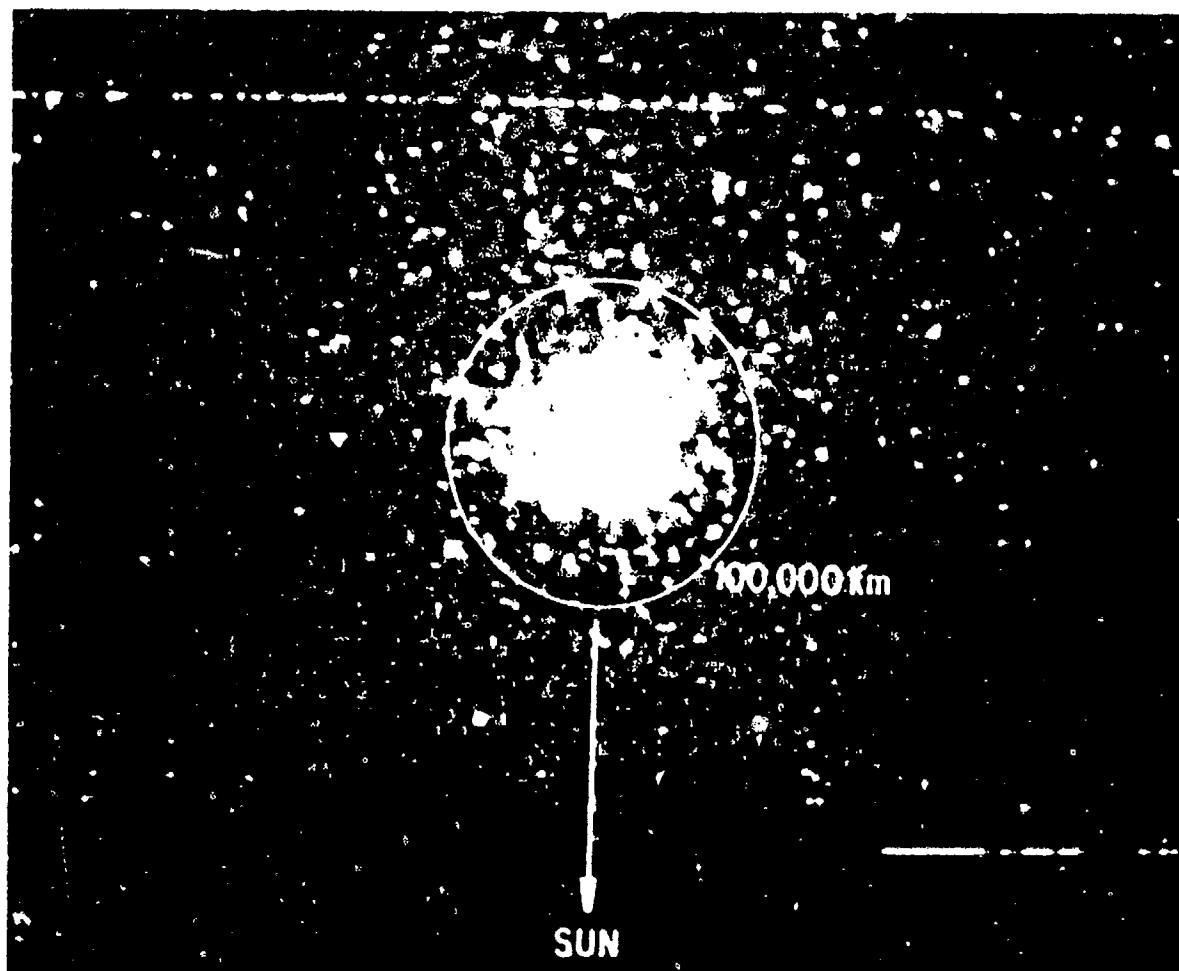


Fig 5. Image of Halley's Comet in the light of OI (6300 Å) emission made by using a F-P interferometer and an intensified CCD. The system sensitivity is approximately 36 R-s.

connection with data from a specialized application. The image of Halley's Comet in Fig. 5 was obtained with a telescope and a F-P interferometer matched to an ICCD by appropriate optics.²¹ The interferometer isolated the cometary OI (6300 Å) emission, which was Doppler shifted from the Earth's airglow line. The intensity gradient from the background to the nucleus of the comet is clear. Unexpectedly, the cloud is not spherically symmetric.

The information contained in the image is the subject of interest here, rather than the physics of the emission, which has been discussed elsewhere.²¹ The image was acquired with a 60-s exposure. The format of the array was 576×384 (0.022-mm) pixels, which have been summed 2×2 . The background level (dark noise) amounts to 1 photoevent in 10 pixels. Near the nucleus of the comet the signal is approximately 1 event/pixel. In spite of the low signal, the image shows an obvious change in surface brightness through 1 order of magnitude. The intensity near the nucleus was 6.3 R. The threshold is therefore approximately 0.6 R. Since this threshold was reached in 60 s, the sensitivity of the system was 36 R s. This is consistent with the $f/1$ example stated above where we note that the ICCD was fed through a Nikon $f/2$ lens of focal length 135 mm. Through the 2×2 summa-

tion, the effective pixel area was increased by a factor of 4 but at $f/2$ the solid angle decreased by a factor of 4. A transmission of 50% would bring the observation into line with the example.

There are other points that can be made from this demonstration. First, we invite the reader to consider the various techniques that could be used in the data analysis and data collection to address this type of imaging. We do not discuss the data further. The question of the comparison of the ICCD image with the CCD image is important for completeness. In the discussion of the CCD, it was estimated that $50 e^-$ would be required per pixel to give a S/N of unity. With the optical system used for the comet observation, the threshold intensity would have been 500 times higher. Even if the CCD noise level were $10 e^-$, the threshold is still out of range by 100. Other optimization of the CCD is possible, but we must also begin to consider such complicating features as working with limited charge and cosmic ray events, etc. We conclude that the strength of the ICCD lies in its application to astronomical problems in which photons are limited.

This research was supported under contract SFRC F19628-85-K-0040 from the U.S. Air Force, National

References

1. Rose, Weimer, and Law, "The image orthicon—a sensitive television pickup tube," *Proc. IRE* **34**, 424–432 (1946).
2. R. W. Engstrom, "Multiplier photo-tube characteristic: application to low light levels," *J. Opt. Soc. Am.* **37**, 420–431 (1947).
3. J. G. Timothy, "Optical detectors for spectroscopy," *Publ. Astron. Soc. Pac.* **95**, 810–834 (1983).
4. R. Bredthauer, C. Chandler, J. Janesick, T. McDurnin, and G. Simms, "Recent CCD technology developments," in *Instrumentation for Ground-Based Optical Astronomy—Present and Future*, L. Robinson, ed. (Springer-Verlag, Berlin, 1988) pp. 486–492.
5. O. H. Siegmund and R. F. Malina, *ACS Symp. Ser.* **2**, 253 (1983).
6. M. L. Lampton, "Recent advances in detectors for the EUV," in *Extreme Ultraviolet Astronomy*, R. F. Malina and S. Bowyer, eds. (Pergamon, New York, to be published).
7. A. L. Broadfoot and B. R. Sandel, "Self-scanned anode array with a microchannel plate electron multiplier: the SSANACON," *Appl. Opt.* **16**, 1533–1537 (1977).
8. G. R. Riegler and K. A. More, "A high resolution position sensitive detector for ultraviolet and x-ray photons," *IEEE Trans. Nucl. Sci.* **NS-20**, 102–106 (1973).
9. B. R. Sandel and A. L. Broadfoot, "Photoelectron counting with an image intensifier tube and a self-scanned photodiode array," *Appl. Opt.* **15**, 3111–3114 (1976).
10. D. G. Torr, R. W. Basedow, and G. H. Mount, "An imaging spectrometric observatory for Spacelab," *Astrophys. Space Sci.* **92**, 237–291 (1983).
11. C. D. Anger, S. K. Babey, A. L. Broadfoot, R. G. Brown, L. L. Cogger, T. Gattinger, J. W. Haslett, R. A. King, D. J. McEwen, J. S. Murphree, E. H. Richardson, B. R. Sandel, K. Smith, and A. V. Jones, "An ultraviolet auroral imager for the Viking spacecraft," *Geophys. Res. Lett.* **14**, 387–390 (1987).
12. R. A. King, A. L. Broadfoot, B. R. Sandel, and A. V. Jones, "Correcting image distortion with fiber-optic tapers," *Appl. Opt.* **27**, 2048–2054 (1988).
13. J. R. Janesick, T. Elliot, S. Collins, H. Marsh, M. M. Blouke, and J. Freeman, "The future scientific CCD," in *State-of-the-Art Imaging Arrays and Their Applications*, K. N. Prettyjohns, ed., *Proc. Soc. Photo-Opt. Instrum. Eng.* **501**, 2–31 (1985).
14. W. G. Fastie, "A small plane grating monochromator," *J. Opt. Soc. Am.* **42**, 641–647 (1952).
15. H. Ebert, *Wied. Ann.* **38**, 489 (1889).
16. A. L. Broadfoot, B. R. Sandel, D. Knecht, R. Viereck, and E. Murad, "A panchromatic spectrograph with supporting monochromatic imagers," *Appl. Opt.* (to be published).
17. A. Vallance-Jones, *Aurora* (Reidel, Dordrecht, the Netherlands, 1974).
18. A. L. Broadfoot and K. R. Kendall, "The airglow spectrum, 3100–10,000 Å," *J. Geophys. Res.* **73**, 426–428 (1968).
19. A. L. Broadfoot, B. R. Sandel, D. E. Shemansky, S. K. Atreya, T. M. Donahue, H. W. Moos, J. L. Bertaux, J. E. Blamont, J. M. Ajello, D. F. Strobel, J. C. McConnell, A. Dalgarno, R. Goody, M. B. McElroy, and Y. L. Yung, "Ultraviolet spectrometer experiment for the Voyager mission," *Space Sci. Rev.* **21**, 183–205 (1977).
20. J. B. Holberg, "Far ultraviolet background observations at high galactic latitude. II. Diffuse emission," *Astrophys. J.* **311**, 969–978 (1986).
21. K. Magee-Sauer, F. L. Roesler, F. Scherb, J. Harlander, and R. J. Oliverson, "Spatial distribution of O (I'D) from Comet Halley," *Icarus* **76**, 89–99 (1988).

APPENDIX D
Final Report, SFRC F19628-88-K-0028

Reprint from *Applied Optics*:

Panchromatic spectrograph with supporting monochromatic imagers

Panchromatic spectrograph with supporting monochromatic imagers

A. L. Broadfoot, B. R. Sandel, D. Knecht, R. Viereck, and E. Murad

The Arizona Imager/Spectrograph is a set of imaging spectrographs and two-dimensional imagers for space flight. Nine nearly identical spectrographs record wavelengths from 114 to 1090 nm with a resolution of 0.5–1.3 nm. The spatial resolution along the slit is electronically selectable and can reach 192 elements. Twelve passband imagers cover wavelengths in the 160–900-nm range and have fields of view from 2° to 21°. The spectrographs and imagers rely on intensified CCD detectors to achieve substantial capability in an instrument of minimum mass and size. By use of innovative coupling techniques only two CCD's are required to record images from 12 imagers, and single CCD's record spectra from pairs of spectrographs. The fields of view of the spectrographs and imagers are coaligned, and all spectra and images can be exposed simultaneously. A scan platform can rotate the sensor head about two orthogonal axes. The Arizona imager/spectrograph is designed for investigations of the interaction between the Space Shuttle and its environment. It is scheduled for flight on a Shuttle subsatellite.

Introduction

The relationship between airglow observations and airglow models has always been a rather subjective one. Modeling now includes a remarkably extensive range of parameters, and present measurements do not effectively constrain all of them. Measurements of many parameters are required to evaluate and constrain the models. Unfortunately the observations that are available for this purpose differ in important ways that complicate their intercomparison. They differ in time, air mass, altitude, solar flux, magnetic conditions, and excitation and quenching mechanisms. The assumptions in relating the data sets to each other are undoubtedly the main source of error so that the data set as a whole does not test a given model at its full potential. Applications of modern technology in optics, detector systems, electronic control, and computing will make a revolutionary change in our ability to collect extensive data sets having fixed interrelationships. The instrument described here, the Arizona Imager/Spectro-

graph (AIS), is a starting point in attacking this problem.

The spectrograph has been recognized as an important diagnostic tool because it records simultaneously a large spectral passband and also retains spatial resolution along its slit. A detector having two-dimensional spatial resolution is required in the image plane; until recently that detector has been photographic film. Replacing the film by the intensified charge coupled device (ICCD) has improved our spectrographic capability in two important ways. First, the ICCD spectrograph has photon-counting sensitivity. Second, the size of the spectrograph is constrained by the detector size, which is quite small. The AIS exploits both of these advantages while retaining spatial resolution along the slit. The application of ICCD's to airglow instruments is discussed in a companion paper.¹

An important guiding principle in the design, construction, and operation of the AIS has been to provide the capability for acquiring spectral and spatial information simultaneously. Toward that end the spectrograph slit, which is imaged on the ICCD detector, is 2 pixels wide \times 192 pixels long. The 192 pixels along the length may be summed into groups of a selectable number of pixels. Summing 8 pixels into each group (as in the example in Fig. 1) divides the length of the slit into 24 segments, and separate spectra are recorded for each segment. Spatial inhomogeneities in the source will be represented

A. L. Broadfoot and B. R. Sandel are with the Lunar and Planetary Laboratory, University of Arizona, Tucson, Arizona 85721. D. Knecht, R. Viereck, and E. Murad are with the Air Force Geophysics Laboratory, Hanscom Air Force Base, Bedford, Massachusetts 01731.

Received 8 April 1991.

0003-6935/92/163083-14\$05.00/0.

© 1992 Optical Society of America.

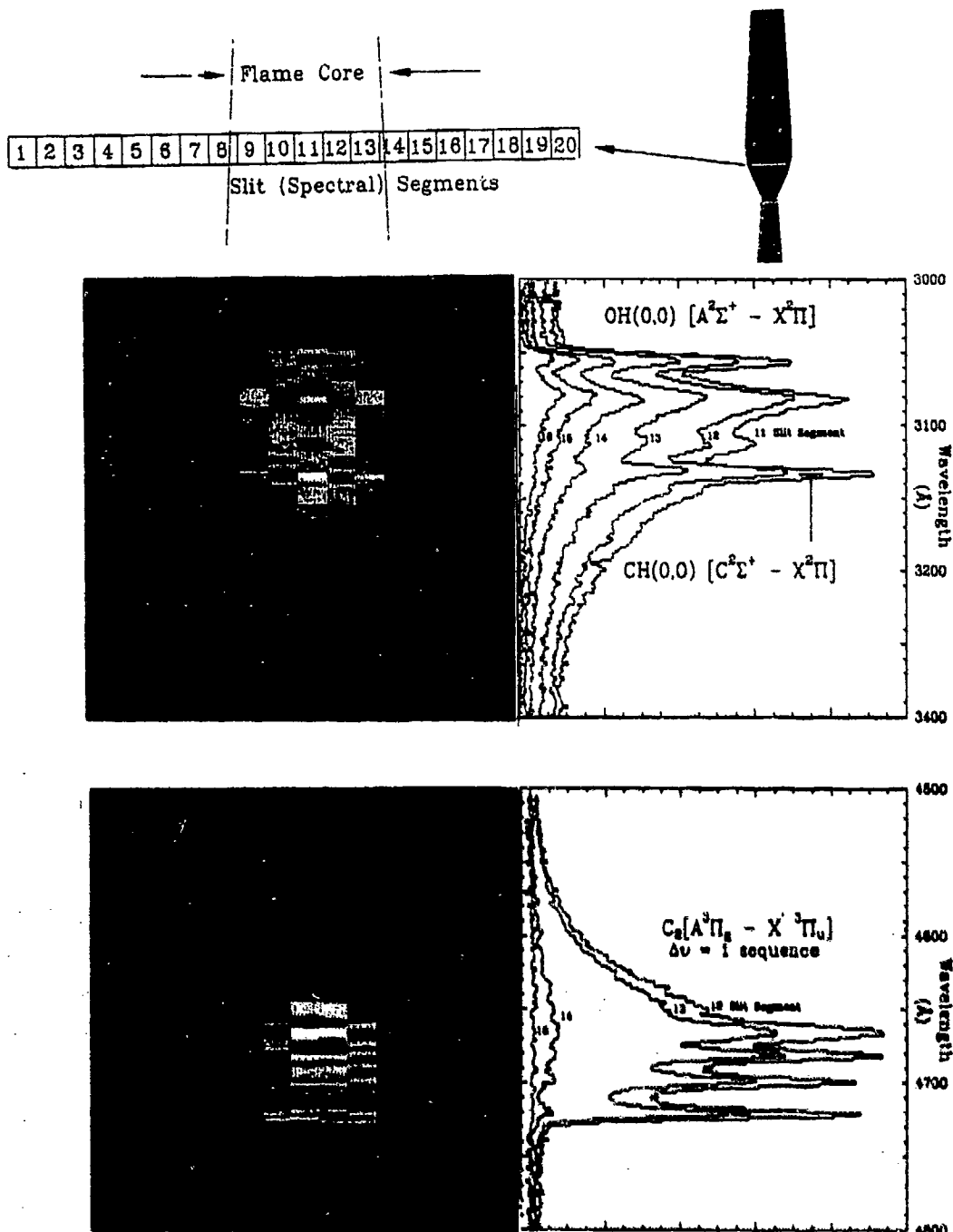


Fig. 1. Spectral-spatial signature of an oxy-fuel flame that illustrates the advantage of an imaging spectrograph, which records spatial variations in the spectrum of the source along the length of its slit. The schematic diagram at the upper right shows the location of the spectrograph slit projected on the flame. The POV along the slit is divided into segments that correspond to different positions within the flame, as shown in the enlarged diagram to the left. Spectra recorded from the individual segments are shown in the color plots below the slit. The line plots are spectra from the selected segments indicated by the numbers near each line. This spatially resolved spectroscopy reveals, for example, a difference in the spatial distributions of OH and CH emissions that would be difficult to measure by other means.

in the set of spectra, which are recorded simultaneously. In this case statistical accuracy in the spectrum is sacrificed to gain spatial information. Statistical accuracy in the spectrum can be recovered in data analysis by summing the adjacent segments, thereby sacrificing spatial detail to improve the signal-to-noise ratio of weak spectral features.

Figure 1 illustrates the advantages of this spectrographic technique. The flame of an acetylene torch was used as the target. In the schematic diagram in the upper right-hand corner, the white line shows the projection of the spectrograph slit across the core of the flame. To the left is an enlarged view of the slit that shows that 20 of the 24 segments were illuminated by the flame. Aligned under the slit are the recorded spectra, one spectrum for each segment. Although the spectral range from 3000 to 9000 Å was recorded at the same resolution, we have selected two spectral regions that include two prominent bands for discussion. The color plot shows that the most intense emission originates in the center of the core of the flame. The UV OH emission extends across 14 segments of the slit, while the longer wavelength C_2 (Swan) bands appear to be confined to the central core. It is noteworthy that the CH(0,0) band is more confined than the OH bands.

The spectrum of the best signal-to-noise ratio will be obtained by summing the central four or five segments. Summing all the segments would increase the noise content unless the emission of interest filled the slit. An improved spatial signature for the band emissions can be obtained by summing the appropriate wavelength bins in the spectral direction.

A companion imager with a passband near 3100 Å would show the extent of the OH emission in two dimensions, but only the spectrograph can separate the blended intensity profile of the CH emission from the nearby OH emission.

All these techniques were available to us with the spectrograph and photographic plate. The improvement available now is in detector and electronic technology. We enjoy all the attributes of the classical spectrograph that is combined with the photon-counting sensitivity of the photomultiplier for every pixel in the detector array.

This approach has a tremendous advantage in studying time-dependent phenomena, such as the active experiments, which have been performed to study ionospheric electron holes²⁻⁴ and atmosphere-plume interactions.⁷ For example, Mendillo *et al.*⁴ observed 630-nm radiation when the Space Shuttle's orbital maneuvering system engines were fired. The observation was made with a narrowband filter. It is reasonable to attribute the radiation to $O(^1D) \rightarrow O(^3P)$. Since the radiative lifetime τ of $O(^1D)$ is ~ 120 s, spectral information as a function of distance along the line of release can be extremely valuable in determining the morphology of this species.

An important factor leading to the consistency of a spectrographic data set is recording the entire spec-

trum at the same time from the same gas column with diagnostic resolution. The AIS comes close to achieving this goal. It records the spectrum from 114 to 1090 nm simultaneously. The spectrum is sampled at 5000 contiguous spectral intervals. The AIS is a true spectrograph by maintaining spatial information along its entrance slit.

The AIS addresses another problem that is common to airglow and auroral spectroscopy, namely, that of relating the location of the observed gas column to the region of the scene being analyzed. The AIS has a complement of 12 coaligned imagers, 10 of which are intensified. By the use of passband filters, the AIS records the spatial extent and surface brightness of emissions. All images are shuttered at the same time as the spectra are.

The instrument described in this paper was designed to meet the needs of a space flight program that is directed at the analysis of the shuttle glow.^{1,2} The Earth's airglow is the background against which the shuttle glow is observed. Useful airglow and auroral observations are made during the same flight opportunity. The AIS is one of a group of instruments that form the payload of the Infrared Background Signature Survey flight program. The experiments are to be flown on the German-built carrier Shuttle Pallet Satellite II, which is manifested for flight on STS-39 in Apr. 1991.

We have prepared a second nearly identical instrument for ground-based airglow and auroral measurements. The spectrograph section covers only the wavelength region from 300 to 1100 nm. The imager passbands and field of view (FOV) are adaptable to the classical auroral and airglow emissions. A third instrument is in preparation for Hitchhiker Shuttle flight opportunities, with the first flight expected in 1992. The primary targets are shuttle glow, contamination and flow fields, as well as airglow and auroral emissions from the atmosphere. The data formats of all these instruments are identical, thus simplifying the intercomparison of data sets. The data are recorded in a widely used format, the Flexible Image Transport System. The Image Reduction and Analysis Facility processing software developed by the Kitt Peak National Observatory is used for data analysis.

Arizona Imager/Spectrograph Overview

The AIS spectrographs and imagers are mounted on an azimuth-elevation scan platform that is driven by stepping motors (Fig. 2). The central box of the spectrograph-imager assembly includes five spectrograph housings of identical mechanical design. The spectrographs cover the wavelength range from 114 to 1090 nm in nine overlapping wavelength bands. Pairs of double gratings in four of the spectrograph housings image eight spectral bands onto four intensified CCD arrays. The fifth spectrograph housing contains a single grating and records the wavelength range from 900 to 1090 nm on a bare (unintensified)

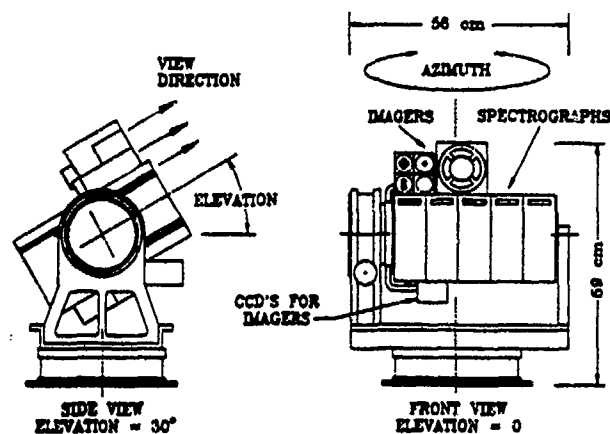


Fig. 2. Two views of the AIS spectrographs and imagers mounted on their scan platform. The nine spectrographs are separated into five housings. Above the spectrograph housings are the 12 passband imagers. The axes of rotation pass through the center of gravity of the rotating section. The FOV's of all the spectrographs and imagers are colligned.

CCD. The FOV of the spectrographs is typically $0.2^\circ \times 2^\circ$. There are no moving parts in the spectrographs. Exposure is controlled electronically by a cathode gate potential or by using the high-speed CCD readout capability, which is 50 ms/frame. The characteristics of each spectrograph are given in Table I.

Figure 2 also shows the cluster of 12 imagers. The imager baffles and intensifiers are mounted on top of the spectrographs. Flexible fiber-optic image conduits carry the images to two CCD's that are mounted beneath the spectrographs. Ten of the images are intensified, and two (the IR images) are not. The IR images are conducted directly to the CCD's by the fiber optics. These two IR imagers can accommodate bright signals and are used for accurate pointing (2° FOV) and field monitoring (18° FOV) to warn of bright emissions coming into the imaging space. Eight UV images are recorded with various passbands and FOV's to support the primary spectrographic experiment. The remaining two imagers have FOV's of 5° and are intensified and filtered for the visible wavelengths of the shuttle glow. The

flexible fiber-optic conduits have separate bundles to acquire the images from the image planes or from the fiber-optic output of the intensifiers. At the CCD end the fiber bundles are gathered in a 2×3 matrix, which matches the image section of the CCD. The CCD is used in the frame transfer mode; the images are moved quickly from the image half to the storage half of the CCD, which effectively shutters the image. All functions are under microprocessor control.

Imaging Spectrographs for ICCD Detectors

Spectrograph Optics

Figures 3 and 4 show the primary features of the optics. After reviewing several optical designs for usefulness with the ICCD detector, we chose one employing aberration-corrected holographic concave gratings. The simplicity of the mechanical design, which could be used at all wavelengths, 20–1100 nm, was the strongest argument. This design requires only one optical element and one surface, compared to five optical elements and nine surfaces that are required by an alternative classical design. The gratings were designed by American Holographics, Inc. Although the first set was expensive, successive sets were quite economical. Tables II and III summarize grating characteristics and spectrograph design parameters.

The number of spectrographs and gratings required to cover the wavelength range from 114 to 1090 nm was determined primarily by the spectral dispersion that is required for a diagnostic spectrum. At short wavelengths the airglow spectrum is fine structured and requires an ~ 0.3 – 0.5 -nm spectral half-width to separate blends and determine rotational structure in molecular bands when accurate spectral modeling is used. At the longer wavelength end of the spectrum band systems are broader, which reduces the dispersion requirement somewhat. The length of the CCD array and the pixel size determine the plate dispersion. For a spectrograph the ideal transmission function is rectangular and 2 pixels in width; therefore the 576-pixel array can record 288 spectral elements along its length or ~ 100 nm for a 0.3-nm width. Secondary constraints included the

Table I. Spectrograph Characteristics

Spectrograph Designation	Wavelength Range (nm)	Resolution (nm)	Photosensitive Material	Dispersion (nm/pixel)	Quantum Efficiency	F Ratio	Sensitivity (DN/s) per Rayleigh
1	1090-900	1.3	Si*	0.32	0.1	2.9	0.003
2	930-764	0.9	GaAs	0.29	0.18	4.1	1.4
3	774-608	0.9		0.29	0.18	4.1	0.8
4	617-532	0.45	S-20	0.15	0.12	4.1	0.7
5	548-482	0.45		0.15	0.12	4.1	1.25
6	488-382	0.45	S-20	0.15	0.25	4.1	0.3
7	386-300	0.45		0.15	0.25	4.1	0.7
8	302-200	0.54	Ca ₂ Te	0.18	0.06	4.1	0.3
9	220-114	0.54		0.18	0.06	4.1	0.3

*Unintensified.

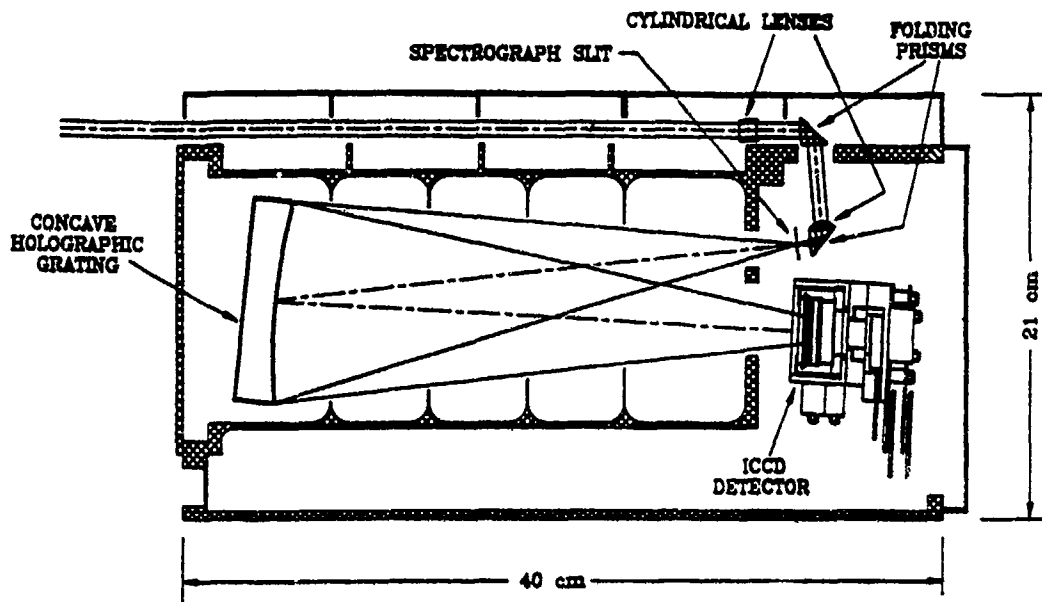


Fig. 3. Cross section in the plane of dispersion of one of the spectrographs. All the spectrographs are based on concave holographic aberration-corrected gratings and hence have a common design. Cylindrical lenses improve baffling and minimize the size of the foreoptics.

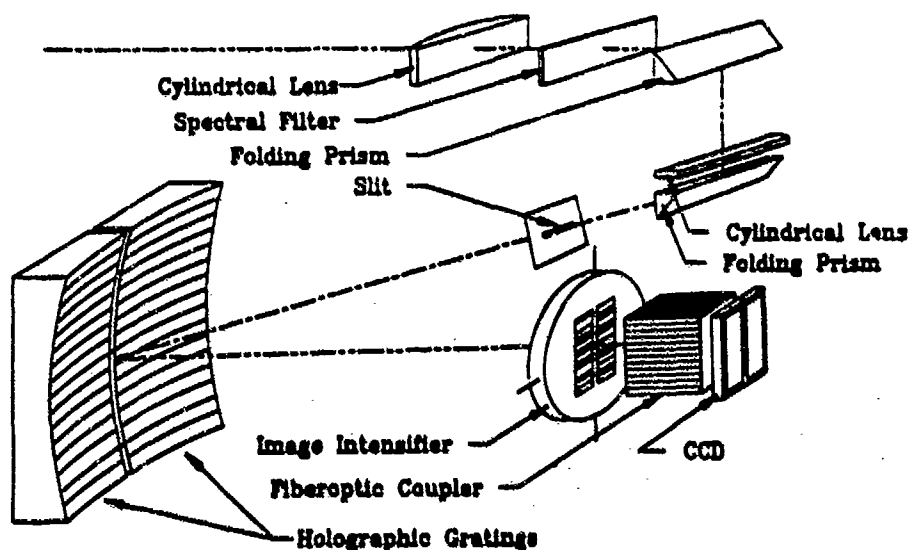


Fig. 4. Schematic diagram of a dual-grating spectrograph. Each grating images its dispersed spectrum on one half of the rectangular detector. A single slit feeds both gratings.

Table II. Grating Characteristics

Grating Number	Wavelength Range (nm)	Slit-Grating Distance (mm)	Grating-Detector* Distance (mm)	Angle of Incidence (deg)	Angle of Diffraction	Angle, Slit-Detector Center
1	1000-900	259.5	277.7	11.5	2.5	9.0
2	830-784	271.2	276.5	10.9	2.7	8.3
3	774-608	271.0	276.3	9.7	1.4	8.3
4	617-532	263.3	279.7	13.4	4.4	9.0
5	548-482	268.0	279.4	12.1	3.1	9.0
6	488-382	271.2	277.0	10.2	2.7	7.5
7	388-300	271.0	276.8	9.0	1.5	7.5
8	303-200	276.9	274.7	1.2	-7.8	9.0
9	230-114	276.2	274.0	2.5	-6.5	9.0

*The spectral plane is perpendicular to the line between the grating center and the detector center.

Table III. Spectrograph Design Parameters

Instrument Parameters	Dual Grating	Single Grating
Full pixel array (per spectrum)	180 × 576	360 × 576
Element size (monochromatic slit image, mm)	180 × 2	360 × 2
Grating radius of curvature (mm)	275	275
Slit dimensions (mm)	0.04 × 4.0	0.04 × 8.0
Grating dimensions (mm)	35 × 100	70 × 100
Effective <i>f</i> number	4.1	2.9

separation caused by the photocathode response and the goal of a reasonably small size. With these constraints the spectrum from 114 to 1090 nm was divided into nine overlapping bands (Table I). Although it is possible to build nine identical spectrographs to cover the spectral range, such a unit would be too large for a practical flight instrument. By using two gratings in each spectrograph we achieved a tractable instrument size. Reducing the grating area results in a loss in throughput by a factor of 2. By reducing the slit length to allow the two spectra to be recorded side by side on a single CCD, the detector area is also reduced by a factor of 2 (Fig. 5). The accumulated reduction in throughput is therefore a factor of 4.

Spectrograph 1 is an exception. The photoelectric sensitivity in the 900–1090-nm range is compara-

tively low for either of the possible detectors, bare silicon of the CCD or the S1 photocathode. The bare CCD was selected because the S1 photocathode requires special cooling, which might not be available, and the sensitivities are not much different. For this spectrograph we chose a lower dispersion to allow a single grating to be used for optimum throughput.

The position of the ICCD detector was unique for each spectrograph. The optical design required that the grating–slit distance be common for all spectrographs and that the detector be perpendicular to the line from the grating center to the detector center. This condition places all the variability in the five spectrographs in the detector position. A special coupler was designed for each spectrograph to satisfy these optical design requirements.

Foreoptics

The FOV of the spectrographs was specified to be 2.3° to encompass the scale of emissions at the expected range to the target. Since the spectrograph slit was 4 mm long, a 100-mm focal length was required. A single lens could be used, but the diameter would have been 50 mm and a sizable off-axis system would be required. Instead cylindrical optics were used to simplify the baffling and minimize the volume of the optical enclosure.

The folded refractive optical system is shown in Figs. 3 and 4 and in the more detailed Fig. 6. Inter-

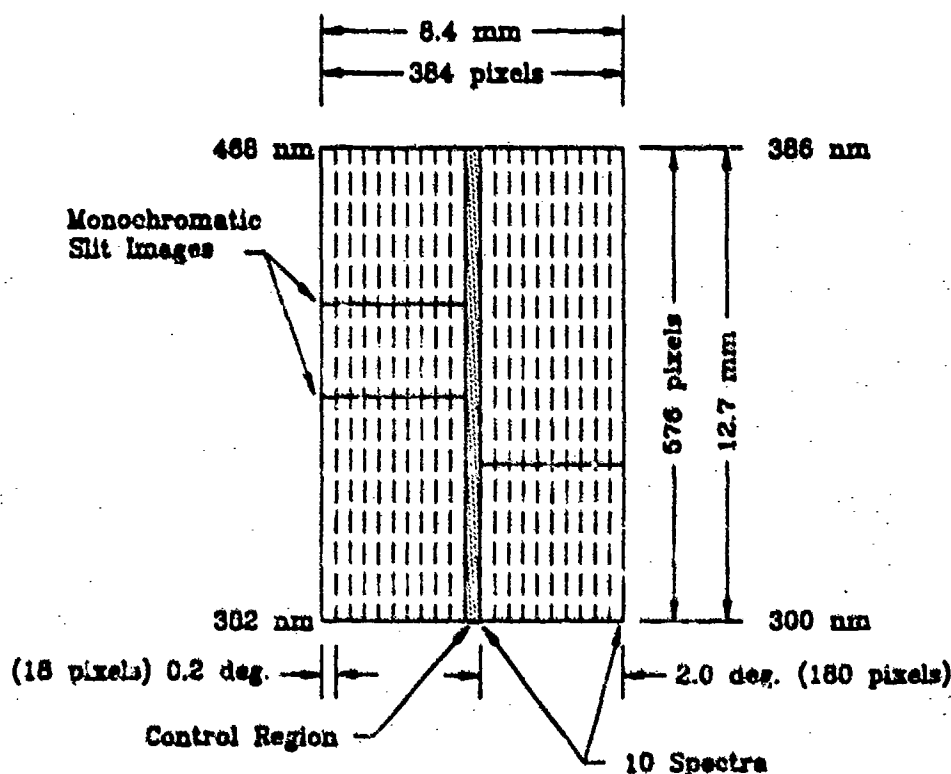


Fig. 5. Organization of the two spectra dispersed onto one ICCD. Readout proceeds by shifting the charges in the top row of pixels horizontally and digitizing them one by one. The charge on all pixels is then shifted vertically by one row. This sequence is repeated until the charge that is collected on all pixels has been sampled serially. The charge from more than one pixel can be shifted into the output capacitor resulting in an on-chip charge summation. Typically several pixels are summed horizontally (the direction parallel to the slit). The readout pattern is computer controlled.

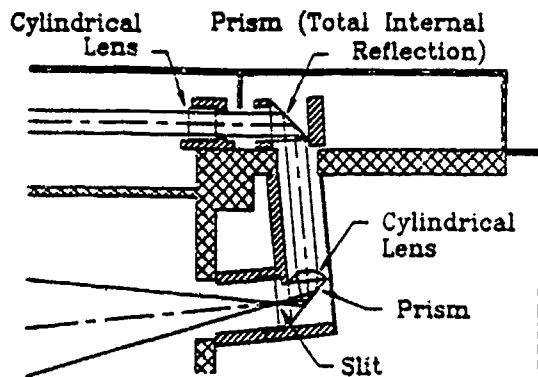


Fig. 6. Cross section of the refractive foreoptics that are used for all but the UV spectrograph. The FOV's across and along the slit are controlled separately with crossed cylindrical optics.

nal reflection in a prism serves as the folding element to minimize reflective losses. A ray trace showed that some of the rays that strike the slit prism would not be internally reflected, so the back surfaces of these prisms were silvered. Crossed cylindrical lenses image the target on the slit. A cylindrical lens of 19-mm focal length is located 19 mm from the slit. The slit width of 0.045 mm restricted the angular width of the FOV to 0.14° outward from the lens. The width of the grating acceptance angle through the slit at the lens was 7 mm. The second cylindrical lens, of 100-mm focal length, is located 100 mm from the slit where the cross-sectional area of the projected grating acceptance angle is $\sim 7.2 \text{ mm} \times 30 \text{ mm}$. The cross-sectional area at entry to the baffle is $7.4 \text{ mm} \times 32.2 \text{ mm}$.

Two spectrographs require special attention. Spectrograph 1 has an entrance slit 8 mm long and therefore requires a focal length of 200 mm to match the FOV of the other spectrographs. The addition of a concave 25-mm focal-length cylindrical lens and adjustment of the position of the 100-mm lens resulted in an effective focal length of 200 mm. Reflective cylindrical foreoptics were needed for spectrograph 5, which covers the wavelength range from 115 to 320 nm (Fig. 7). Although the problem of chromatic aberration in refractive optics was eliminated, considerable spherical aberration was introduced by the short focal-length cylindrical surface. Three reflections were required to match the FOV requirements. The reflective surfaces were coated to enhance UV reflection to 1150 Å.

Thermal Compensation

For most satisfactory performance the CCD's and intensifiers should be at a temperature below -10°C . At these temperatures both the CCD leakage current and intensifier shot noise are small during an exposure time of 10 s. To achieve this temperature the whole spectrograph is radiatively cooled. Alignment is done at room temperature, and the Shuttle Pallet Satellite flight thermal model predicts temperatures as low as -70°C . This is a temperature range of 100°C , which implies a change of $\sim 0.07 \text{ cm}$ in length

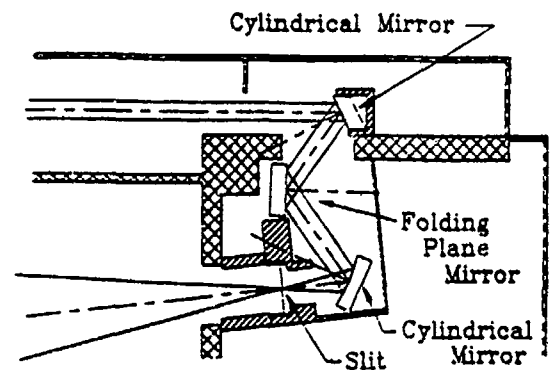


Fig. 7. Cross section through the reflective foreoptics of the UV (115-320 nm) spectrograph. The refractive optics of Fig. 5 are replaced with the equivalent cylindrical reflective components. Considerable spherical aberration in the FOV is introduced but does not reduce the data quality.

of the spectrograph body over the focal length of 27.5 cm caused by thermal contraction. A change in focus of only 0.012 cm would degrade the spectral resolution. Therefore the grating-detector separation is thermally compensated by the mechanical design and material selection. The gratings in the spectrograph are deposited on Zerodur blanks, which have a coefficient of thermal expansion near zero. To maintain focus through the temperature extreme the position of the grating relative to the slit and detector is established by Invar rods that are 29.2 cm long between clamps, which limits the change in focus to $1 \times 10^{-3} \text{ cm}$ for $\Delta T = 100^\circ\text{C}$. A stainless-steel diaphragm is sandwiched in the grating holder and attached to the spectrograph frame. This diaphragm provides lateral support of the grating but deforms to allow longitudinal motion. Invar rods extend from the four corners of the grating holder to fixed points near the image plane as noted above.

Passband Imagers

Airglow Imaging

The main purpose of imaging in this investigation is to provide information about the spatial distributions of a variety of species. It is also designed to allow pointing of the spectrographs accurately and provide a photometric map of extended gas clouds that are being analyzed by the spectrographs; therefore high spatial resolution is not necessary. Imaging must be done simultaneously to properly associate the band-pass images to changing conditions and to be contemporaneous with the one-dimensional image of the spectrograph.¹ For this reason we use multiple imagers instead of a filter wheel. The CCD image frame of 384×288 pixels was subdivided into six arrays of 128×144 pixels (Fig. 8). With two CCD's we expose 12 images simultaneously. Flexible fiber-optic image conduits collect the images directly or from intensifiers and transfer them to the CCD's.

Because of the small image format ($2.8 \text{ mm} \times 3.2 \text{ mm}$), miniature optics can be used, and up to six images can be formed on a single standard 15-min

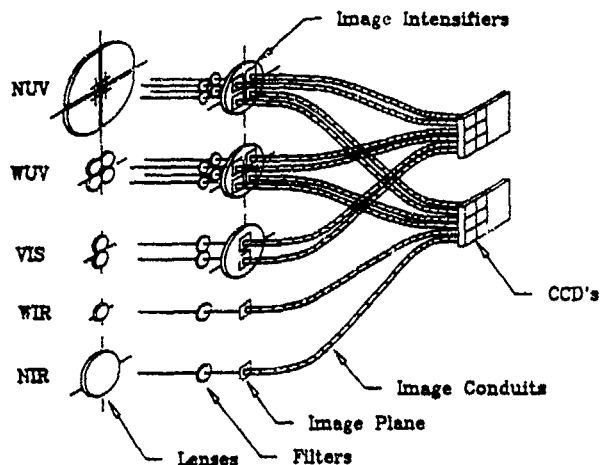


Fig. 8. Schematic diagram of the imager components. Coherent fiber-optic bundles transfer the passband images to one of two CCD's.

image intensifier. Broadfoot and Sandel¹ point out that the photometric efficiency E of an imager is independent of the size of the imager since the throughput is proportional to the detector area A and the solid angle of illumination Ω , where the solid angle Ω is in turn proportional to the reciprocal f ratio squared; that is, $E \propto A/f^2$. The area of the detector is the pixel, which is a constant of the system. The f ratio is independent of the size of the optics. The design parameter remaining is to satisfy the FOV by selection of the focal length, then to optimize the aperture to minimize the f ratio.

Imager Set

Figure 8 summarizes the imager sets. The sets are classified as narrow angle (N) or wide angle (W) and are referred to by the wavelength regions of UV, VIS, and IR. Images formed by the lenses are conducted by flexible fiber-optic bundles to two CCD's. The two IR imagers are not intensified. Proximity focused image intensifiers are used to intensify the remaining 10 images. The light from the phosphor is conducted by the fiber-optic faceplate to a flexible fiber-optic image conduit. The light is conducted to a third fiber-optic window, which is in contact with the surface of the CCD. The images were arranged in groups of six as illustrated in Fig. 9 on the image half of the CCD. The UV images were split to minimize the effect of a failure in a single CCD. In retrospect this arrangement was more complicated than needed; future instruments would not use such an arrangement.

The imager complement that is needed to satisfy the scientific requirements is listed in Table IV. Eight imagers record UV emission in four different passbands in the 150–270-nm wavelength range. Four of these have a FOV of $\sim 2^\circ$ to match the spectrographs. The remaining four imagers have similar passbands but 25° FOV's to examine the larger context of the spectrographs and narrow-angle imagers.

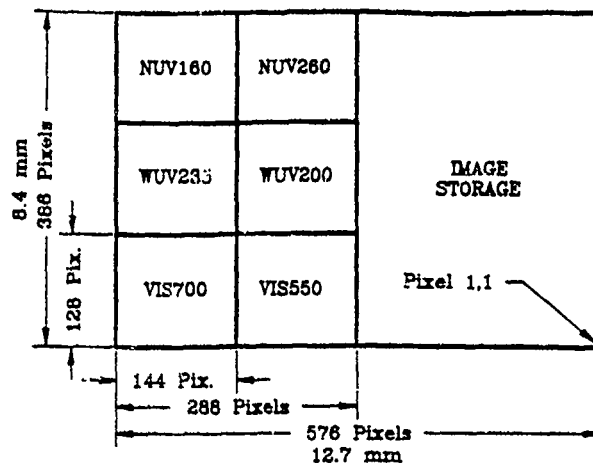


Fig. 9. Locations of images on one of the two CCD's that are used for imaging. The frame transfer capability of the CCD is used to move the image to the storage area. Exposure continues while the storage area is being digitized. The second imaging CCD records the remaining six images in a similar way.

Wide and narrow-angle unintensified imagers assist in several ways. Their wavelength band is restricted to the IR region around 900 nm, which is probably an important region for shuttle glow. The NIR (2° FOV) will define the pointing of the spectrographs. The WIR (18° FOV) surveys the field and detects bright sources that should be avoided by the intensified channels. The shuttle glow is also the target of interest for the other two medium-field (5° FOV) imagers that cover two visible bands.

Infrared Imagers

The IR imagers are the most straightforward since the image is formed directly on the end of the flexible fiber-optic bundle. The lens for the wide-angle imager is a commercial lens of 9-mm focal length and 5-mm-diameter lens. A filter between the lens and the fiber bundle limits the wavelength to > 700 nm. The lens and filter are located in the center of a plate that is spaced from the image plane to focus. Figure 10 illustrates the mechanical layout. A standard frame size that is 50 mm square was used for most of the imagers' sections. The insides of the baffle tubes were machined to a common diameter so that baffles and spacers for most imagers have a common outside diameter. Inside diameters of the baffles were machined in a jig, which allowed all baffle sets to be machined as a group and provide tapered knife-edges. The baffles and spacers were stacked in the baffle tube and held in by a jam nut. The walls of the baffle tubes were machined to leave a wall thickness of 1.3 mm between square endplates.

Figure 11 is a section through the narrow-angle IR imager. A lens with a 75-mm focal length and 40-mm diameter was selected for this application. In both IR imagers the end of the fiber-optic bundle can be moved to adjust the focus.

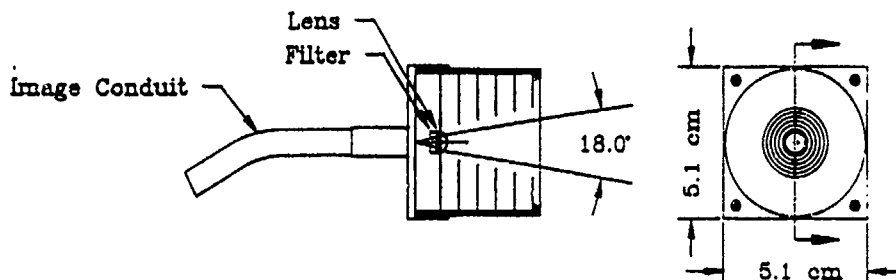


Fig. 10. Wide-angle IR imager. No image intensifier is used for this passband.

Visible Wavelength Imagers

Figure 12 is a cross section through the two visible imagers. Two identical lenses (focal length, 35 mm; diameter, 9 mm) form separate images on the photocathode of a single proximity focused image intensifier. The fiber-optic output of the intensifier is coupled to the flexible fiber-optic bundle to transfer the image to the CCD.

Wide-Angle UV Imagers

The WUV's presented some special problems. Given the chosen image size, the desired field of 25° implies a focal length of 6.8 mm. Using such a short focal-length lens was complicated by the fact that the intensifier window was 5 mm thick. Reimaging designs using refractive spherical optics were considered, but they presented many problems and did not provide better imaging than the single lens that was used. The wide-angle lens consists of a MgF_2 hemisphere and a MgF_2 spacer that form an image on the photocathode. An aperture stop at the base of the hemisphere limits image aberrations. Ray tracing showed significant changes in the imaging properties from the center to edge of the image plane caused by the change in focal distance. The two adjustable parameters were the size of the aperture stop and the focal plane distance. It was demonstrated that a fairly uniform image quality over the image plane could be achieved with an $f/2$ aperture stop and with the image plane at the median distance between the best focus for on-axis and edge rays. Most (80%) of the rays fall inside a circle of 2-pixels diameter. This is an acceptable resolution for an imager that is intended to detect changes in the surface brightness of extended gas clouds.

Figure 13 is a cross section through two of the imagers. The proximity-focused image intensifier has a MgF_2 window and a Cs_2Te photocathode with a

sensitive area that is 17 mm in diameter. The center of the images lies on a circle that is 12.75 mm in diameter, which is common to all the multiple imagers.

Narrow-Angle UV Imagers

The design goals for the NUV (2°) set were to achieve a minimum mass by using only one image intensifier while maximizing the throughput and minimizing cost. A trade-off study of both refractive and reflective optics was carried out in parallel with a search for commercially available lens systems. Refractive designs could be used but require changes for each wavelength. The reflective design seemed more general. A high-speed reflective optics lens manufactured by the Nye Optical Company appeared to have the best characteristics. It employs a spherical primary surface and an aspherical secondary in a Cassegrain configuration. The effective focal length is 90 mm, and the effective focal ratio is 1.1.

Mechanical modifications of the selected lens were needed to have four optical axes and thereby four images. A cross section of this imager is shown in Fig. 14. The lens was sawed into four pie-shaped sections, which were then separated by the appropriate distance, i.e., 12.75 mm as mentioned above. The secondary was reassembled and bonded to a backplate of appropriate material. Provision was made to adjust the primary sections individually. Preliminary adjustments were made at visible wavelengths before the bandpass filters and the Cs_2Te intensifier were installed.

Intensified CCD Detectors

Application of the intensified CCD detector has been discussed in detail in a companion paper.¹ The principles outlined there have been used to define the AIS. Figure 15 shows an ICCD assembly.

Proximity-focused image intensifiers were pro-

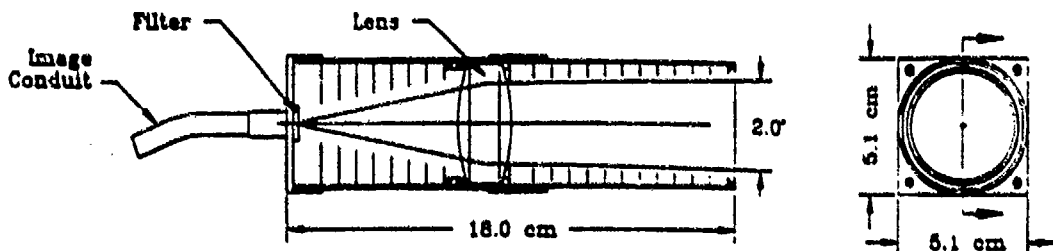


Fig. 11. Narrow-angle IR imager.

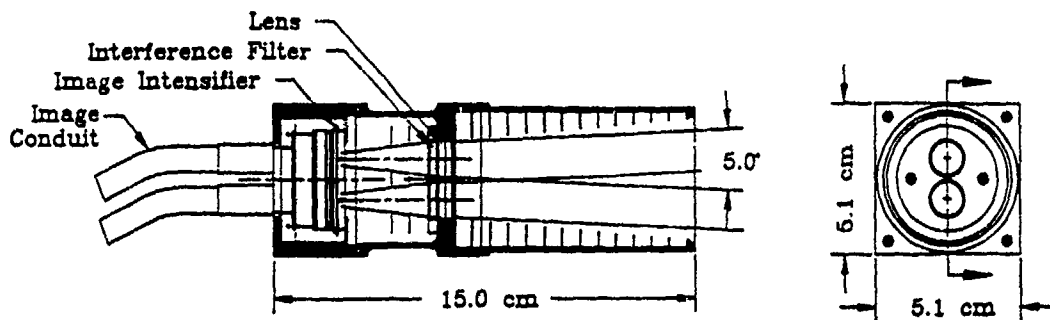


Fig. 12. Two visible intensified imagers (VIS 700, 500).

cured from several manufacturers. Four cathode materials were used to cover the spectrum (Tables I and IV). Two special specifications were placed on the intensifiers: (1) flying leads and (2) a transparent conductive coating on the fiber-optic output window. Although all the intensifiers could have been obtained with wraparound power supplies in essentially the same mechanical envelope, we prefer to control the intensifier gain with digitally controlled high-voltage power supplies. The conductive coating isolates the CCD from any charge leakage caused by the high voltage (6000 V) on the intensifier anode.

Intensifiers from different manufacturers tend to have different dimensions; thus a special external shell was needed to establish a common interface between the instrument and the CCD assembly. The housing is close fitting with potting cavities. A 50-mm \times 50-mm format about the detector axis is maintained on three sides. Special attention was given to ensuring that the fiber-optic window was plane with the back surface of the housing when the intensifier is potted into place. The flying leads were led through cavities to Reynolds 167-3770 connectors. The cavities were potted for insulation purposes.

Figure 15 illustrates the ICCD configuration. The fiber-optic window is oil coupled to the face of the CCD. A ceramic frame is used to attach the window to the CCD package. This CCD assembly is then positioned in the larger housing with the window plane with the surface of the housing, since this is the interface to the intensifier. A small copper evaporator with a copper inlet and outlet tubes is coupled to the rear of the CCD package for cooling. The contacts to the CCD pins are provided by a constantan

wire leading out the back. The cavity around the CCD pins is covered and the cavity is potted. The CCD housing and covers are made of Delrin, which was chosen for its electrical and thermal insulating properties. Two printed circuit boards are stacked on the back of the housing, one for CCD biasing and clocking and one for the preamplifier. A recirculating Freon refrigeration system cools the CCD to its operating temperature, which is -20°C or lower. Although the AIS/Shuttle Pallet Satellite instrument is radiatively cooled in space, cooling is required for laboratory operation and most ground-based applications.

We have tried thermoelectric cooling of the CCD without much success. The heat load through the fiber-optic window is large, which requires high currents and therefore efficient heat sinking. This is not consistent with the small size that is desired.

The CCD readout circuitry is enclosed in the electronics compartment below the spectrographs. Both the clocking and the analog signal line are shared among the CCD's. The electronics can control eight CCD's and intensifiers, as discussed below.

Photometric Sensitivity

The sensitivity of both spectrographs and imagers is discussed in the companion paper.¹ This section deals with the technique of calibrating the instruments and results. Finally the results are reconciled with the calculations to relate the design expectations to the instrument performance. The tools that were used to perform the instrument calibration include continuum light sources (quartz iodide lamps, hydrogen lamps), a set of calibrated passband filters, a detector that has been calibrated against a National

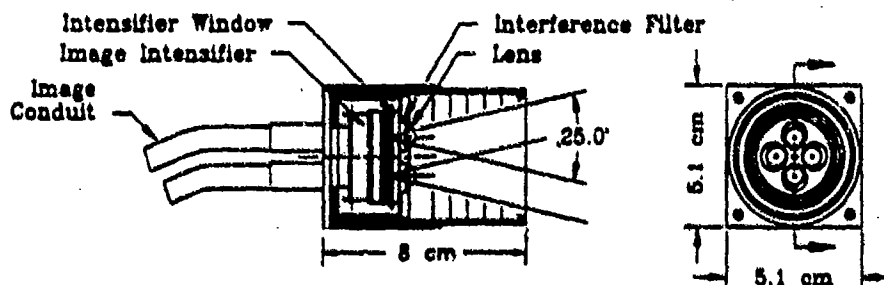


Fig. 13. Set of four wide-angle ultraviolet imagers (160, 200, 235, 260). Because of their short focal lengths, the four lenses are bonded to the window of the image intensifier.

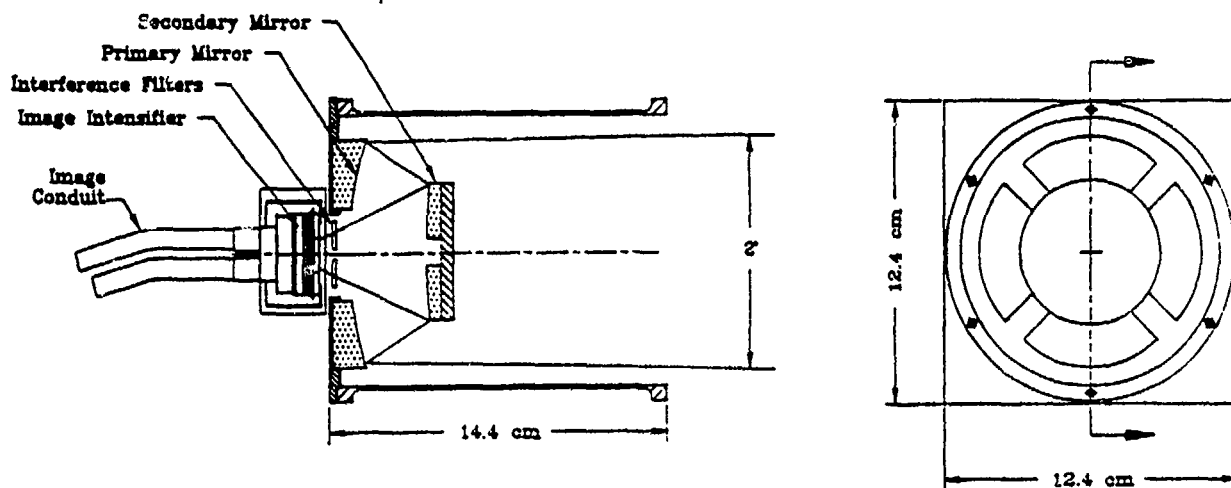


Fig. 14. Set of four narrow-angle ultraviolet imagers (160, 200, 235, 260). The Cassegrain design uses a four-segment optical system to form separate images in each of four passbands.

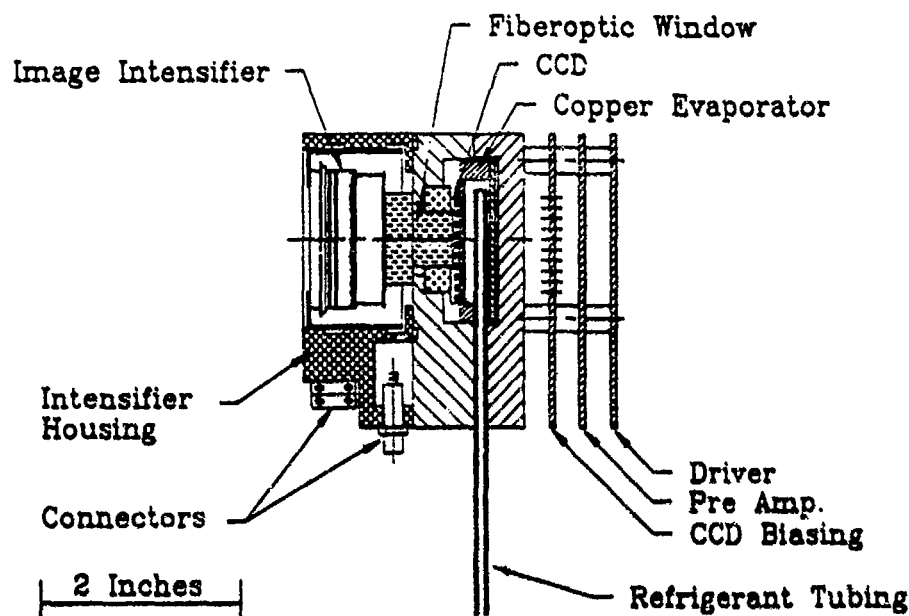


Fig. 15. Intensifier-CCD assembly. The refrigeration evaporator is used only for laboratory testing. The AIS is passively cooled in flight.

Table IV. AIS Imager Characteristics

Imager Number	Imager Type	Imager Designation	Wavelength Peak (hw) (nm)	Angular FOV		Photo-sensitive Material	Angular Resolution (deg/pixel)	Quantum Efficiency (% trans.)	F Ratio	Sensitivity (dn/s) per Rayleigh per Pixel
				$\Delta\lambda$ (deg)	EI (deg)					
1	NUV	NUV 160	160 (25)	1.8	1.6	Ca_2Te	0.013	0.06	2.2	0.076
2	NUV	NUV 200	200 (25)	1.8	1.6		0.013	0.06	2.2	0.070
3	NUV	NUV 235	235 (25)	1.8	1.6		0.013	0.06	2.2	0.13
4	NUV	NUV 260	260 (25)	1.8	1.6		0.013	0.06	2.2	0.39
5	WUV	WUV 160	160 (25)	25	21	Ca_2Te	0.17	0.06	2.2	0.58
6	WUV	WUV 200	200 (25)	25	21		0.17	0.06	2.2	0.55
7	WUV	WUV 235	235 (25)	25	21		0.17	0.06	2.2	0.65
8	WUV	WUV 260	260 (25)	25	21		0.17	0.06	2.2	1.6
9	Medium VIS	VIS 500	500 (200)	6.0	5.3	S-20	0.042	0.11	2.6	4.0
10	Medium VIS	VIS 700	700 (200)	6.0	5.3		0.042	0.09	2.6	2.3
11	WIR	WIR 900	900 (400)	21	19	Si^*	0.15	0.1	2.3	0.098
12	NIR	NIR 900	900 (400)	2.3	2.0	Si^*	0.016	0.1	2.3	0.062

*Unintensified CCD.

Table V. Mass and Dimensions of AIS Components

AIS Component	Mass (kg)	Dimensions:
		Height × Length × Width (cm)
Scan platform	75	60 × 40 × 36
Instrument control unit	10	23 × 36 × 33
Low-voltage power supply	8	10.5 × 35 × 26
High-voltage power supply	8	10 × 30 × 23
Data recording unit	15	20 × 50 × 25
Motor driver box	1	5.2 × 18 × 9.4
Cables	7	

Bureau of Standards standard detector, and a diffusing screen that filled the FOV of the spectrograph or imager being calibrated.

Two techniques were used to calibrate the spectrographs. The first approach was to illuminate the diffusing screen with the light source and bandpass filter. Filters were available for at least two wavelength regions within the spectral range of each spectrograph. The spectrum was recorded for each of the bandpass filters, and the screen brightness was measured with the standard detector. The spectrograph record verified the transmission function of the filter. The integral of the recorded spectrum, compared with the brightness that is measured by the standard detector, determined the instrument sensitivity at each filter wavelength. Second, the diffusing screen was illuminated by a stabilized continuum source. The continuum was recorded by all spectrographs simultaneously. The diffusing screen was observed by the standard detector through the bandpass filters to establish its brightness in specific wavelength bands. The spectrographic record established the run of intensity in the continuum. The comparison of the brightness that was measured through the bandpass filter with the recorded continuum spectrum established the sensitivity. The results of several calibrations are given in Table I along with other parameters that are useful in comparing spectrographs. The sensitivity is reasonably con-

stant through the spectral range of each spectrograph.

The second calibration method described above is the most useful for field work and for reconciling possible differences between spectrographs in their regions of overlap. The continuum intensity can be reproduced by using regulated power supplies and confirmed by monitoring with a standard detector and single bandpass filter at a preferred wavelength.

Calibration of the imagers was straightforward. The continuum source was used to illuminate the screen, and the continuum brightness was determined by the filters and standardized detector as describe above. The sensitivity determined for each imager is given in Table IV, along with other characteristics of the imagers.

In the companion paper¹ the expected sensitivity was calculated in terms of the rayleigh-second (R-s), which is the emission rate in rayleighs that is required to provide a signal-to-noise ratio of unity in 1 s. The calculation assumes that the ICCD detection system has photon-counting efficiency, and therefore the result is the count rate, in photoevents per second, that results from an emission rate of 1 rayleigh. The difference in the calculation and the measurement is in the gain of the system; the average signal level per photoevent can be calculated by combining the two measurements. If, for example, a 1-rayleigh emission rate produces 2.9 DN/s, and the sensitivity is 4 R-s, a single photoevent gives an average signal level of 11.6 DN, where DN is a data number equal to one unit in the analog-to-digital conversion.

Arizona Imager/Spectrograph Subsystems

The AIS subsystems include the sensor head with the spectrographs and imagers, the scan platform, the instrument control unit, the low-voltage power supplies, the high-voltage power supplies, the data recording unit, the motor drive box, and interconnecting cabling. Table V lists the mass and dimensions of these subsystems. Figure 16 shows a block diagram of the subsystems and their interconnections.

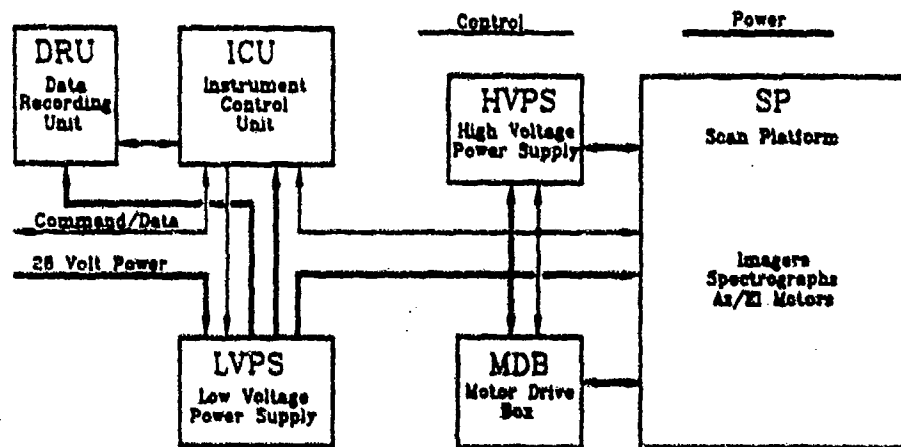


Fig. 16. Block diagram of the AIS electronics subsystems.

Table VI. Micro Computer Memory

Memory Type	Kbytes
Boot ROM (fused link)	8
Capacitor backed-up RAM	4000
EPROM	384
RAM	256
Data RAM (double ported)	3000

Scan Platform

A scan platform can direct the coaligned FOV's of the AIS to specified targets. The platform has two axes of rotation, which we refer to as azimuth and elevation. The sensor head is suspended between two bearings on the elevation axis. This assembly is mounted on a turntable that provides the azimuth rotation. Both motions are driven by stepping motors through worm gears. For strength and reliability, the worm gears were doubly tapered cone gears manufactured by Cone Drive Textron, which engage 19 teeth. The step size is 0.0082° in elevation and 0.014° in azimuth. The rotation range in elevation is -60° to 135° from the horizontal and in azimuth -175° to $+175^\circ$. The scan rates are $105^\circ/\text{min}$ in azimuth and $52^\circ/\text{min}$ in elevation. The position is measured in terms of the number of steps from a fiducial microswitch for each axis.

Instrument Control Unit

All AIS functions are initiated in the computer that are housed in the instrument control unit. This circuitry can be divided into three sections: the microcomputer, the CCD controller, and the interface circuitry. A VME bus backplane was used, and all circuitry was fabricated on double Eurocard printed circuit boards.

A complementary metal-oxide semiconductor single-board computer controls the AIS. Important changes

to provide reliability and flexibility were made in the memory addressable by the 80C86 microprocessor. The memory sections are listed in Table VI. A custom boot program was written for the BIOS read-only memory (ROM). All the essential startup and communications subroutines were included in the BIOS, which was written into the Fused Link ROM. The bit patterns in this memory cannot be altered permanently by high-energy particle penetration. The operational programs for the AIS were written into the EPROM, but reliability was insured by providing three copies of the program and a load routine that corrects errors to the bit level.

Variable parameters are stored in capacitor-backed RAM so that the instrument can be powered down without loss of information on the current instrument configuration. The AIS program is loaded from the EPROM to the RAM to run. A 3-Mbyte double-ported memory serves for data accumulation and buffering.

Figure 17 is a diagram of program flow. When power is applied to the instrument control unit the microcomputer performs the CPU health check, establishes the engineering telemetry link, and completes the instrument functional tests. In flight selected science data and engineering data are queued for a real-time low-rate data link. Most of the data are collected at high speed in the data memory, then transferred to an optical disk when the observation has been completed. Most of the observing programs are stored in the EPROM because the command uplink capability in flight is quite limited.

The CCD controller, referred to as the micro control unit, contains a simple processor and memory. The readout format of the spectrographs (Fig. 5) is selected by on-chip or off-chip summation to form effective pixels that are long and narrow by summing in the direction parallel to the slit. The effective pixel appears to be $1 \times N$ real pixels, the length N

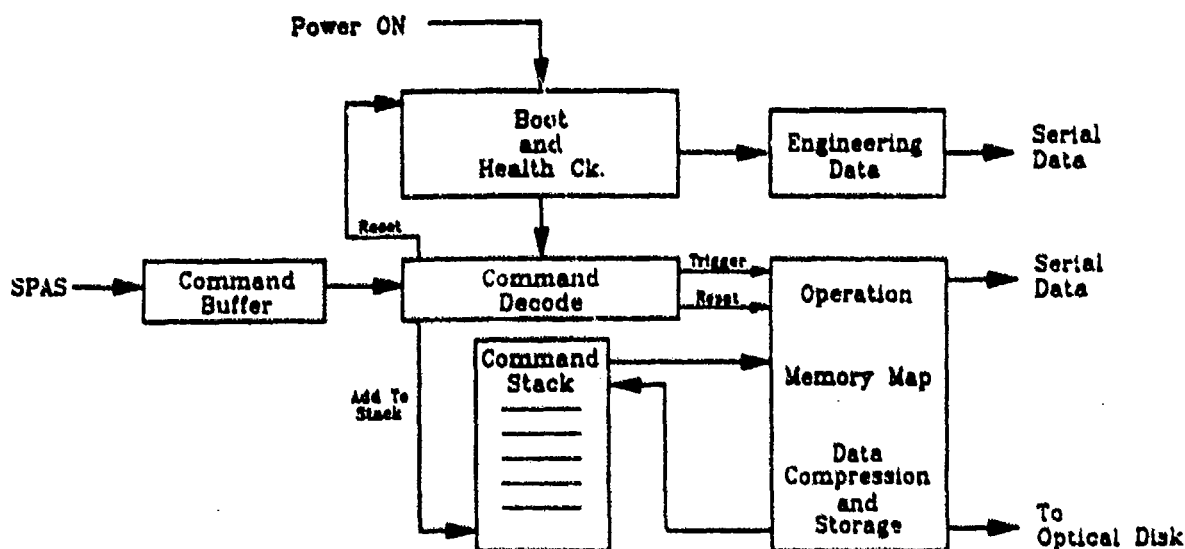


Fig. 17. Logical blocks of the AIS control software.

depending on the spatial resolution that is required. The imagers can be read out with on-chip or off-chip summation to form larger square pixels of 2×2 , 3×3 , etc. Pixel windows are addressable. High-speed clocking is also available; the pixel shift rate can be increased from the 1-MHz rate that is used with digitization to a 4-MHz rate when the charge is shifted but not digitized. Several readout formats can be stored in the micro control unit program memory. Once a particular program is activated the micro control unit free runs.

Power Supplies and Data Recorder

The low-voltage power supply subsystem contains nine miniature power supplies and matching EMI filters that are manufactured by Integrated Circuit Inc. Turning on power to the AIS activates only the power supplies that power the instrument control unit microprocessor. When the microprocessor has performed its self-check, it can power other parts of the system as required. To save power and reduce heating, power supplies are turned on only when they are needed.

Each intensifier has its own high-voltage power supply. The seven units were manufactured by K&M Electronics, Inc. (Model M2225). Digital inputs to each supply control the microchannel plate voltage and photocathode gating potential.

Most of the data that are collected by the AIS will be stored on a 200-Mbyte WORM optical disk recorder manufactured by OptoTech and ruggedized to military specifications by Mountain Optech. The optical disk and its power converter are housed in a sealed vessel that maintains 1 atm of pressure.

This research was supported under contract SFRC-F19628-86-K-0040 from the U.S. Air Force. Addi-

tional funding in support of this effort has been received from the National Aeronautics and Space Administration under contract NASW-4245 and NASA grant NAG5-637 through Goddard Space Flight Center, Wallops Flight Facility.

References

1. A. L. Broadfoot and B. R. Sandel, "Application of the ICCD to airglow and auroral measurements," *Appl. Opt.* 31, 000-000 (1992).
2. A. W. Yau, B. A. Whalen, F. R. Harris, R. L. Gattinger, M. B. Pongratz, and P. A. Bernhardt, "Simulations and observations of plasma depletion, ion composition, and airglow emissions in two auroral ionosphere experiments," *J. Geophys. Res.* 90, 8387-8406 (1985).
3. P. A. Bernhardt, "A critical comparison of ionospheric depletion chemicals," *J. Geophys. Res.* 92, 4617-4628 (1987).
4. M. Mendillo, J. Baumgartner, P. D. Allen, J. Foster, J. Holt, G. R. A. Ellis, A. Klekociuk, and G. Reber, "Spacelab-2 plasma depletion experiments for ionospheric and radio astronomical studies," *Science* 238, 1260-1264 (1987).
5. P. A. Bernhardt, B. A. Kashiwa, C. A. Tepley, and S. T. Noble, "Spacelab-2 upper atmospheric modification experiment over Arecibo. 1. neutral gas dynamics," *Astron. Lett. Commun.* 27, 169-182 (1988).
6. P. A. Bernhardt, W. E. Swartz, M. C. Kelley, M. P. Sulzer, and S. T. Noble, "Spacelab-2 upper atmospheric modification experiment over Arecibo. 2. plasma dynamics," *Astron. Lett. Commun.* 27, 183-194 (1988).
7. E. Murad, D. J. Knecht, R. A. Viereck, C. P. Pike, D. C. Cooke, I. L. Kofsky, C. A. Trowbridge, D. L. A. Rall, G. Ashley, L. Twist, J. B. Elgin, A. Setayesh, A. T. Stair, Jr., and J. E. Blaha, "Visible light emission excited by interaction of Space Shuttle exhaust with the atmosphere," *Geophys. Res. Lett.* 17, 2205-2206 (1990).
8. P. M. Banks, P. R. Williamson, and W. J. Raitt, "Space Shuttle glow observations," *Geophys. Res. Lett.* 10, 118-121 (1983).
9. S. B. Mende, O. K. Garriott, and P. M. Banks, "Observations of optical emissions on STS-4," *Geophys. Res. Lett.* 10, 122-125 (1983).